Transport Models and In Vitro Study for the Permeability of the Blood-brain Barrier to Water and Solutes

by

Guanglei Li

A dissertation submitted to the Graduate Faculty in Biomedical Engineering in partial fulfillment of the requirements for the degree of Doctor of Philosophy

The City University of New York

2010

This manuscript has been read and accepted for the Graduate Faculty in Engineering in satisfaction of the dissertation requirement for the degree of Doctor of Philosophy.

Professor Bingmei Fu

Date — Chair of Examining Committee

Professor Mumtaz Kassir

Date — Executive Officer

Professor John M. Tarbell

Professor Luis Cardoso

Professor David S. Rumschitzki

Professor Peter Ganatos

Professor Barclay Morrison

Supervisory Committee

THE CITY UNIVERSITY OF NEW YORK

ABSTRACT

TRANSPORT MODELS AND IN VITRO STUDY FOR THE PERMABILITY OF THE BLOOD-BRAIN BARRIER TO WATER AND SOLUTES

by

Guanglei Li

Adviser: Dr. Bingmei M. Fu

The blood-brain barrier (BBB) is a dynamic barrier between blood circulation and central nervous system (CNS). Its unique structure provides a protective role for the CNS as well as a barrier to drug delivery to the brain. Although numerous studies have been conducted to understand the transport mechanism of the BBB, they are rather qualitative. Therefore, one objective of this thesis is to quantitatively investigate the structural mechanism by which the BBB controls the transport of water and solutes. Another objective is to build and characterize in vitro BBB models for drug delivery study.

For water and small hydrophilic solutes, the major route across the BBB is a paracellular pathway. In the first part of this study, a mathematical model for water and neutral solute transport through the paracellular pathway was developed to predict the permeability of the BBB to water and neutral solutes. The endothelial surface glycocalyx (SGL) and the basement membrane (BM) of the

BBB carry negative charge due to their glycosaminoglycan compositions. In the second part of this study, an electro-diffusion model for the transport of charged molecules across the BBB was developed. In this model, constant charge densities were assumed in the SGL and in the BM. Both electrostatic and steric interaction and exclusion to charged molecules were considered within the SGL and the BM, and at their interfaces with non-charged regions of the BBB. The model predicted that the charge density in both SGL and BM would be ~30 mEq/L based on the permeability data for positively and negatively charged solutes measured in intact rat mesenteric and pial microvessels.

In vitro BBB models have been widely used due to their advantages over *in vivo* models. In the third part of this study, several *in vitro* BBB models were developed: endothelial monoculture (immortal mouse brain microvascular endothelial cell line, bEnd3), coculture of bEnd3 and primary rat astrocytes, coculture with basement membrane substitutes. The hydraulic conductivity, transendothelial electrical resistance and diffusive solute permeability of these in vitro models to various-sized solutes were quantified. The expression of the BBB tight junction proteins in these models was also assessed using RT-PCR and immunofluorescence. The results suggest that the endothelial monoculture and the coculture models are fairly good models for studying the transport of relatively large solutes across the BBB.

ACKNOWLEDGMENTS

It is a great pleasure to thank many people who made this thesis possible. First I want to give my deepest gratitude to my advisor, Dr. Bingmei Fu for all her valuable guidance, endless support, and encouragement. Thank her for leading me into this challenging research field, and for helping me build the foundation of my future career.

I also want to give my deep thanks to the members of my thesis committee: Dr. John Tarbell, Dr. David S. Rumschitzki, Dr. Luis Cardoso, and Dr. Peter Ganatos, and Dr. Barclay Morrison. Thank Dr. John Tarbell for letting me using his Laboratory. I learnt many valuable skills in cell and molecular biology there. Thank Dr. Barclay Morrison for providing cellular supplies and support to my research and study.

I would like to give my special thanks to other members of my Lab, Dr. Min Zeng, Dr. Wei Yuan, Dr. Qin Liu, Jie Fan, Bin Cai, Lingyan Shi, and Lin Zhang. I also want to thank my colleagues, Zhongdong Shi, Limary Cancel, Veronica Lopes, Henry Quaz, Melissa Simon, Jing Chen. They gave me tremendous help in my research and life. Thanks for all of them being a great source of support and friendship.

Finally, I would like to thank my parents back in China and my husband Mingyuan Huang for their unconditional love and support through all these years. Without them, I have not been here.

Contents

LIST OF FIGURES

LIST OF TABLES

CHAPTER 1 INTRODUCTION

1.1 The Blood-Brain Barrier

Central nervous system (CNS) is the most critical and sensitive system in human body. Normal function of the CNS necessitates a highly regulated extracellular environment to ensure appropriate activities of neurons. The concentrations of ions such as Na^+, K^+ and Ca^{2+} within CNS must be maintained within very narrow ranges. Some substances contained in our diet, although readily metabolized and excreted in peripheral systems, could be quite neurotoxic so they need to be excluded from the CNS. Furthermore, metabolic demand of neuron tissues is pretty high, with the CNS consuming approximately 20% of oxygen and energy produced by glucose oxidation in human body (Rolfe and Brown, 1997). Therefore, it is essential that the interfaces between the CNS and the peripheral circulatory system serve as a dynamic regulator of ion balance, a barrier to potentially harmful molecules, and a facilitator of nutrient transport. Actually, there are two major interfaces, blood-brain barrier (BBB) and blood-cerebrospinal fluid barrier, in different locations between the CNS and the peripheral circulation. However, the surface area of the BBB is 5000 times that of the blood-cerebrospinal fluid barrier (Hawkins and Davis, 2005), so the BBB is the major mechanism for regulating the substance exchange between the CNS and peripheral tissue.

The BBB is known as a “neurovascular unit” consisting of the cerebral microvascular endothelium, astrocytes, pericytes, neurons, and the extracellular matrix (Hawkins and Davis, 2005) .The first experimental evidence for the existence of the BBB is discovered by Ehrlich (1885). After injecting a water-soluble dye trypan blue into the circulatory system, he found that it stained all human organs except the brain and spinal

cord (Ehrlich, 1885). Later, Goldmann injected trypan blue directly into the cerebrospinal fluid (CSF) and found that it stained all cell types in the brain but failed to penetrate into the periphery tissue (Goldmann, 1913). This result indicates that there is a barrier to the dye between the CNS and the peripheral circulation. Lewandowsky is the first one to use the term *bluthirnschranke* (blood-brain barrier) while studying the limited permeation of potassium ferrocyanate into the brain (Lewandowsky, 1900)

Figure 1.1 shows a schematic of the three-dimensional BBB structure. The capillary lumen is enclosed by endothelial cells and the abluminal surface of the microvessel is ensheathed by astrocyte foot processes. The cross-section of the BBB was shown in **Fig. 1.2:** A**,** an electron microscopic image; B, graphic reconstruction of the vessel (Farkas and Luiten, 2001). On the luminal surface of endothelium, there is a surface glycocalyx layer (SGL) consisting of heparan sulfate proteoglycan, chondroitin sulfate proteoglycan, and hyaluronic acid (Henry and Duling, 1999; Tarbell and Pahakis, 2006). The brain microvessel wall consists of endothelial cells, whose apposing membranes form tight junctions (TJ), which limit the paracellular passage to water and solutes (Romero et al., 2003). Pericytes attach to the abluminal membrane of the endothelium at irregular intervals. Both endothelial cells and pericytes are surrounded by a uniform and narrow matrix-like basement membrane (BM) which has collagen type IV, heparin sulfate proteoglycans, laminin, fibronectin, and other extracellular matrix (ECM) proteins (Leblond and Inoue, 1989; Miosge, 2001). On the tissue side, the BM is ensheathed by astrocyte foot processes which cover more than 98% of the brain microvasculature surface (Cohen et al., 1995; Pardridge, 1999).

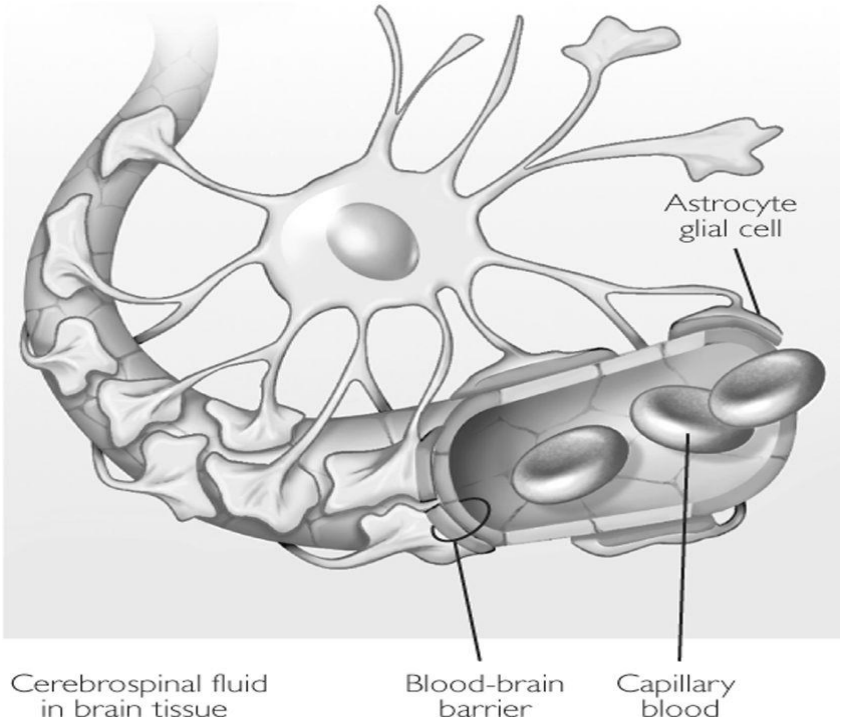

Figure 1.1 The three-dimensional anatomical structure of the BBB. The capillary lumen is enclosed by endothelial cells. The whole microvessel is ensheathed by astrocyte foot processes (http://medical-dictionary.thefreedictionary.com/_/viewer.aspx?path=mosbyCAM&name=500057-fx20.jpg).

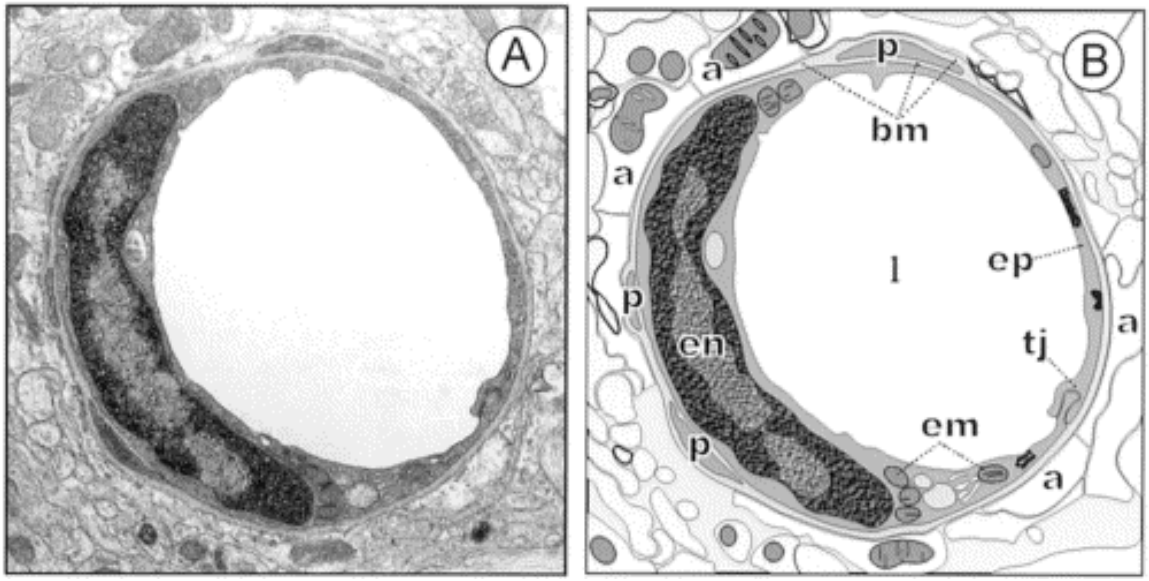

Figure 1.2 The cross-sectional view of a typical rat cortex capillary. A: an electron microscopic image; B: graphic reconstruction of the vessel (Farkas and Luiten, 2001). Abbreviations: a, astrocytic end feet; bm, basement membrane; em, endothelial mitochondria; en, endothelial nucleus; ep, endothelial cytoplasm; l, capillary lumen; p, pericytes; tj, tight junction.

The brain microvessels are different from those in the rest of the body in several different aspects. First, the brain endothelium is ensheathed by pericytes and astrocytes foot processes that almost cover the entire abluminal surface of capillaries. The close apposition of astrocytes to endothelial cells is thought to be necessary for the development and maintenance of the BBB junction proteins (Hurwitz et al., 1993; Haseloff et al., 2005). The uniform and thin matrix-like BM sandwiched between the astrocytes and the endothelium acts as a permeability barrier, retarding the movement of molecules into brain tissue, and participates in the maintenance of the BBB integrity (Hawkins and Davis, 2005). Second, between adjacent endothelial membranes, there are junctional complexes which include adherens junction (AJ), tight junction (TJ), and possibly gap junctions (Simard et al., 2003). The structure of the junction complexes between endothelial cells is shown in **Figure 1.3** (Kim et al., 2006). Both AJ and TJ act

to restrict para-cellular transport across the endothelium while gap junctions mediate intercellular communication. AJs are ubiquitous in the vasculature and their primary component is vascular endothelial (VE)-cadherin. They basically mediate the adhesion of endothelial cells to each other and contact inhibition during vascular growth and remodeling. Although disruption of AJ at the BBB can lead to increased permeability, TJ is the major junction that confers the low para-cellular permeability and high electrical resistance (Romero et al., 2003). The tight junction complex includes two classes of trans-membrane molecules: occludins and claudins. These trans-membrane proteins from adjacent endothelia cells interact with each other and form seals in the spaces between adjacent endothelial cells. The cytoplasmic tails of the trans-membrane proteins are linked to the actin cytoskeleton via a number of accessory proteins such as members of the zonula occludens family, ZO-1, ZO-2 and ZO-3. Third, the cytoplasm of the brain endothelial cell is uniformly thick with very few pinocytotic vesicles and no fenestrations. Besides, an enzymatic barrier, capable of metabolizing exotic agents and drugs, exists in the cerebral endothelial cell.

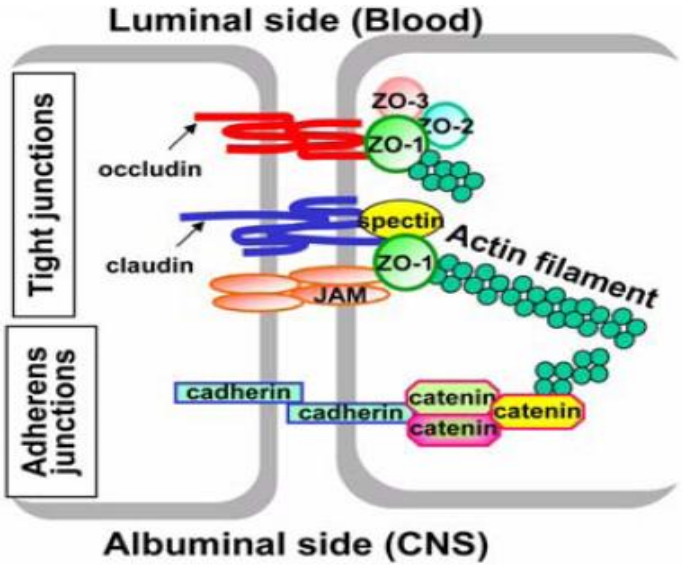

Figure 1.3 Schematic representations of the junction complexes between endothelial cells(Kim et al., 2006). There are two major classes of junction complexes: tight and adherens junctions. The transmembrane molecules (occludins and claudins) from adjacent endothelial cells interact with each other and form seals in the paracelullar spaces. The cytoplasmic tails of the transmembrane proteins are linked to the cytoskeleton via a number of accessory proteins, including members of the zonula occludens family (ZO-1, ZO-2, and ZO-3) and catenin.

1.2 Transport across the BBB

To satisfy the special need of brain, transport across the BBB occurs through six different mechanisms: simple diffusion, facilitated diffusion, carrier-mediated transport, receptor-mediated endocytosis, absorptive-mediated transport and carrier-mediated efflux. **Figure 1.4** shows all the mechanisms and routes for the transport across the BBB (Neuwelt, 2004a). The transport of substances from the capillary blood into the brain tissue depends on the molecular size, lipid solubility, binding to specific transporters, and electrical charge (Moody, 2006). Small hydrophilic molecules like sodium fluorescein (NaFl) can pass the BBB by diffusion when they circulate in the blood. Small lipid-philic molecules can cross the BBB by transcellular facilitated diffusion because they can easily diffuse through cell membranes. The BBB provides selective carrier systems for essential

nutrients such as glucose, amino acids, and vitamins. Receptor-mediated endocytosis (RME) is the major method for supplying the brain with peptides and proteins, such as low-density lipoproteins, transferrin, insulin, leptin and growth factors. Efflux transport pumps metabolites and xenobiotics from the brain to the blood circulation. P-glycoprotein (P-gp), a member of the adenosine triphosphate-binding cassette family of exporters, was found to be a potent energy-dependent efflux pump in brain capillaries.

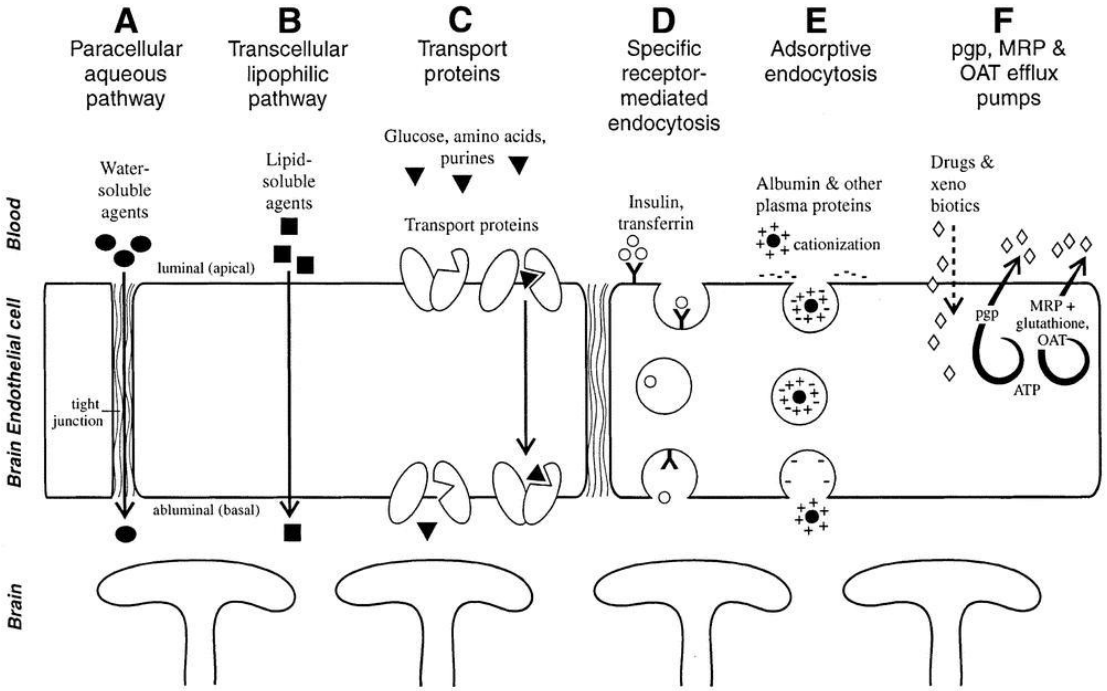

Figure 1.4 Transport pathways across the BBB. For normal homeostasis, carrier-mediated transport systems exist for hexoses (glucose, mannose, and galactose), monocarboxylic acids (acetic, lactic, and pyruvic acids), large neutral amino acids (tyrosine, phenylalanine, and isoleucine), acidic amino acids (glutamate and aspartate), basic amino acids (arginine and lysine), nucleic acid precursors (adenine, adenosine, and guanine), choline, and thyroid hormones (via transthyretin). The large neutral amino acid transporters, like the glucose transporter, are present on both the luminal and abluminal membranes of endothelial cells and are bidirectional, although they are most important for influx to the brain, whereas other transporters are unidirectional efflux systems. The carrier for small neutral amino acids is primarily located on the abluminal membrane and allows only efflux. Potassium efflux is archieved with an energy-dependent process that exchanges sodium for potassium at the abluminal membrane, with adenosine triphosphate (ATP) as the energy source (Na+/K+-adenosine triphosphatase). P-gp, which is localized

to the luminal membrane of endothelial, pumps amphipathic organic cations or neutral compounds out of the CNS into the blood, while multidrug resistance-associated protein (MRP) and organic anion transporter (OAT) pump anions out of the CNS as efflux proteins (Neuwelt, 2004b).

1.3 Significance of the Study

Pathology of CNS Diseases

The loss of BBB structural integrity and normal function is involved in many CNS diseases. Using a variety of tracers, disruption was found to be associated with various neurological disorders such as migraine, postconcussion syndrome (Korn *et al*., 2005), multiple sclerosis (Minagar and Alexander, 2003), and epilepsy (Roch *et al*., 2002). Increase in the BBB permeability is either a precipitating event in diseases like multiple sclerosis (MS), or a consequence of the pathology in cases such as ischemic stroke and traumatic brain injury. In many cases, the BBB is disrupted transiently and allows the influx of molecules and cells which are normally excluded from the brain under homeostatic conditions (Calabria and Shusta, 2006).

After the BBB disruption, vasogenic edema and brain swelling will occur. As a result, the intracranial pressure will increase and blood flow to the brain will reduce, and ischemia will follow. This edema response induced by the BBB disruption has a very bad effect on the brain. It can cause the progression of multiple sclerosis and encephalitis (Floris et al., 2004), induce the autoimmune destruction of myelin and neurons(Petty and Lo, 2002) , and induce the progression of AIDs. Under some circumstances, it could even develop into a life threatening complication of stroke (Rosenberg, 1999).

Although many biochemical factors induced by these brain diseases have been found to affect the endothelial tight junction proteins and modulate the neurovascular

matrix, how they ultimately disrupt the structural components of the BBB to increase the BBB permeability, and how to restore the BBB structures by therapeutic agents, are still not well understood. Current clinical treatment of vasogenic edema relies on systemically administered osmotic agents to suck the fluid from the brain (Qureshi and Suarez, 2000). This method can help releasing the symptoms of edema but can not reverse it and eliminate the cause of edema. Therefore, understanding the mechanism responsible for BBB breakdown is very critical for the treatment of the BBB disruption and other CNS diseases.

Drug Delivery to the CNS

A large number of people in the world are now suffering from CNS diseases. The total number of patients with CNS diseases is reported to be larger than that with cardiovascular diseases (Pardridge, 2006). While the BBB serves as a natural defense that safeguards the brain against the invasion of various circulating toxins and infected cells, it also provides a significant impediment toward the delivery of diagnostic and therapeutic agents to the brain via the systemic route. Essentially almost 100% of large-molecule drugs, including peptides, recombinant proteins, monoclonal antibodies, RNA interference (RNAi)-based drugs and gene therapies, and more than 98% of small-molecule with molecular weight more than 500 daltons can not penetrate the brain microvessel wall (Pardridge, 2006).

Various methods such as intracerebral implantation, microdialysis, convection-enhanced distribution, osmotic shock, and chemical modification of the BBB have been developed for delivering drugs into the brain. However, the applications of these methods are limited and they can only partially keep with the demands of modern therapies. For

instance, the efficiency of intracerebral implantation, microdialysis and convection-enhanced distribution methods are low since their major transport mechanisms are diffusion and convection of interstitial fluid. The penetration distances of drugs delivered by the above three methods are reported to be less than 1mm (Mak et al., 1995). For effective treatment of the CNS diseases, therapeutic agents have to reach the specific regions of the brain at an adequate amount. So it is of great importance to investigate the molecular composition, structure, and transport mechanisms of the BBB to improve the drug delivery efficacy.

1.4 Microvessel Permeability to Water and Solutes

The microvessel wall behaves as a permeable membrane for water and small hydrophilic solute transport. The membrane transport properties are often described by Kedem–Katchalsky equations derived from the theory of irreversible thermodynamics,

$$J_s = PRT\Delta C + \left(1 - \sigma_f\right)CJ_v \tag{1.1}$$

$$J_v = L_p(\Delta p - \sigma_d RT\Delta C) \tag{1.2}$$

Here L_p, the hydraulic conductivity, describes the membrane permeability to water. P, the diffusive permeability, describes the permeability to solutes. J_s and J_v are the solute and volumetric fluxes per unit area; ΔC and Δp are the concentration and pressure difference across the membrane. σ_f is the solvent drag or ultrafiltration coefficient which describes the retardation of solutes due to membrane restriction, and σ_d, the reflection coefficient, describes the selectivity of membrane to solutes. For trans-endothelial transport, σ_f is equal to σ_d (Curry, 1983) and thus we often use σ, the reflection coefficient, to represent both of them. R is the universal gas constant and T is the absolute temperature.

From the above equation, we can see that L_p could be calculated by $J_v/\Delta p$ when $\Delta C = 0$ and P can be obtained from $J_s/\Delta C$ when J_v=0.

1.5 Previous Studies

Mathematical Models

To quantitatively understand the structural mechanisms whereby the microvessel wall modulates the transport of water and solutes, a number of mathematical models have been developed to predict the measured permeability data based on the ultra-structural data obtained from electron microscopy for peripheral microvessels.

Based on the ultra-structure of the inter-endothelial cleft obtained by random section electron microscopy, simple one-dimensional theories like the pore–slit and the fiber matrix theory were first applied to correlate cleft structure with the large amount of experimental data for hydraulic conductivity L_p and the diffusive permeability P before the late 1980s (Wissig, 1979; Michel and Curry, 1999). Later, based on serial section electron microscopic study for the ultra-structure of frog mesenteric microvessels (Adamson et al., 1993), Fu et al. (1994) proposed a three-dimensional junction-pore-matrix model as shown in **Figure 1.5**. In their model for the inter-endothelial cleft, an endothelial surface glycocalyx layer was considered to be a molecular sieve. In the junction strand, large breaks with dimensions 2d×2B exist and the spacing between the breaks is 2D. There is also a small continuous slit of height $2b_s$ along the junction strand. The depth of the whole cleft is L and the thickness of the junction strand is L_{jun}. L_1 and L_3 are depths between junction strand and the luminal and abluminal fronts of the cleft, respectively. At the entrance of the cleft on luminal side, there is a fiber layer of thickness L_f. The radius of these fibers and the gap spacing between fibers are represented by *a*

and Δ. For frog mesenteric capillary, this model provided an excellent fit for L_p and P data with regards to solutes of size ranging from potassium to albumin.

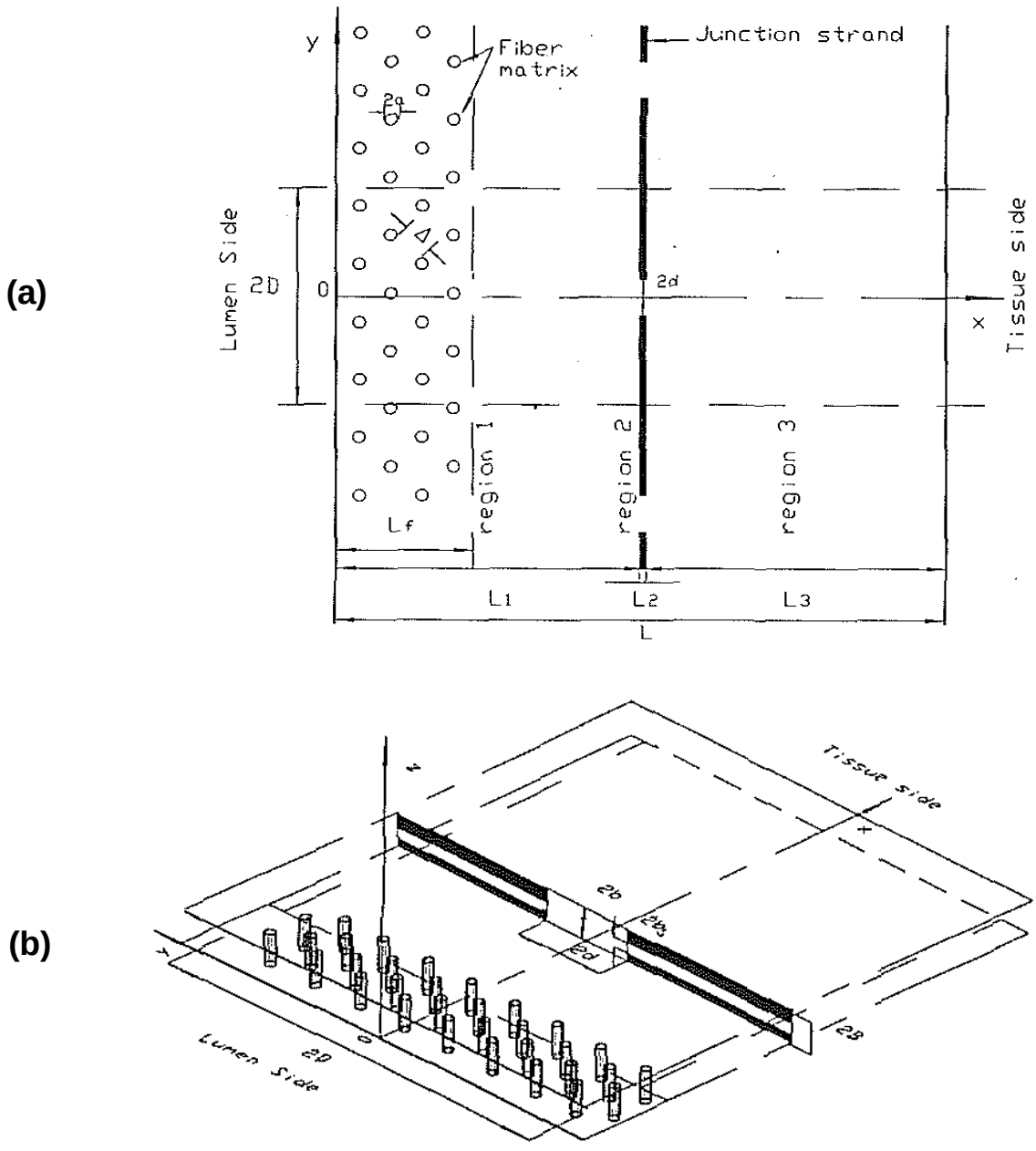

Figure 1.5 Model for the inter-endothelial cleft structure proposed by Fu et al (1994) (a) the plane view of surface glycocalyx layer and the cleft region, (b) the 3-D sketch.

I*n vivo* studies found that increase intracellular cAMP levels would decrease the permeability of microvessel to water and solute. One reason of this phenomenon is that cAMP increases the number or complexity of junction strands in the para-cellular cleft (Adamson et al., 1998). To quantitatively analyze the ultra-structural mechanisms of altered microvessel permeability by cAMP, Fu and Chen (2003) developed a modified 3D junction-pore-matrix model with two junction strands in the interendothelial cleft.

To develop a transport model of the BBB, the previous 3D models (Fu *et al.*, 1994; Fu and Chen, 2003) are extended in this study to include other structural components of the BBB, the basement membrane and astrocyte foot processes. The model prediction is validated by comparing it with the *in vivo* permeability for small solutes across rat pial microvessels measured using a non-invasive technique(Yuan et al., 2009b).

Previous experimental results suggested that the microvessel wall contained negative charges. First, Adamson et al. measured the permeability of two similar size globular proteins, ribonuclease (net charge=+4) and α-lactalbumin (net charge=-10) across frog mesenteric capillary and found that the permeability of positively charged ribonuclease was twice of that for negatively charged α-lactalbumin. Accordingly, several mathematical models have been employed to describe the charge effect on microvessel permeability. A simple Donnan-type model was the first one to be used (Deen et al., 1980; Adamson et al., 1988). It was suggested that the steric and electrostatic exclusions could be described in terms of an effective partition coefficient (Φ_{eff})

$$\phi_{eff} = \phi_{steric} \exp(-Z\Delta EF / RT) = \phi_{steric} \exp(-Z\Delta\psi) \tag{1.3}$$

Here, Φ_{eff} is the steric partition coefficient describing the size selectivity of the membrane, ΔE is the effective Donnan electrical potential difference across the

mmembrane, Z is the charge number of the solute, $\Delta\psi = F\Delta E / RT$ is the dimensionless electrical potential, R is the universal gas constant, F is Faraday's constant, T is temperature, E is the electrical potential.

Recently, an electrochemical model investigating the transport of charged molecules across glycocalyx layer was proposed by Stace and Damiano (Stace and Damiano, 2001; Damiano and Stace, 2002). It investigated the influence of the anionic groups within capillary glycocalyx on the electrochemical transport of charged molecules through the microvessel. Their model assumed that the glycocalyx was a multi-component mixture including a fluid constituent (blood plasma), mobile ions (cations and anions), and a solid proteoglycan/glycoprotein/GAG matrix with fixed negative charges. Later, Fu et al. (2003) considered the transport across the inter-endothelial region and developed a two-dimensional model incorporating the effect of both size and charge. This model provides the first quantitative analysis of various experimental results expected to be associated with negative charges in trans-vascular pathways.

In Vitro Experimental Models

The development of *in vitro* models for the BBB has enabled the study of transport phenomena at the molecular and cellular levels. The aim of such *in vitro* BBB models is to functionally resemble as many as possible the unique characteristics of the BBB. Compared with in vivo animal models, the *in vitro* models are relatively accessible, flexible, reproducible and abundantly available. Previous investigations showed that the permeability of the *in vitro* BBB models to various compounds such as sucrose, retinoic acid, retinol, haloperidol, caffeine, and mannitol was comparable to the permeability data obtained from *in vivo* models (Franke et al., 1999).

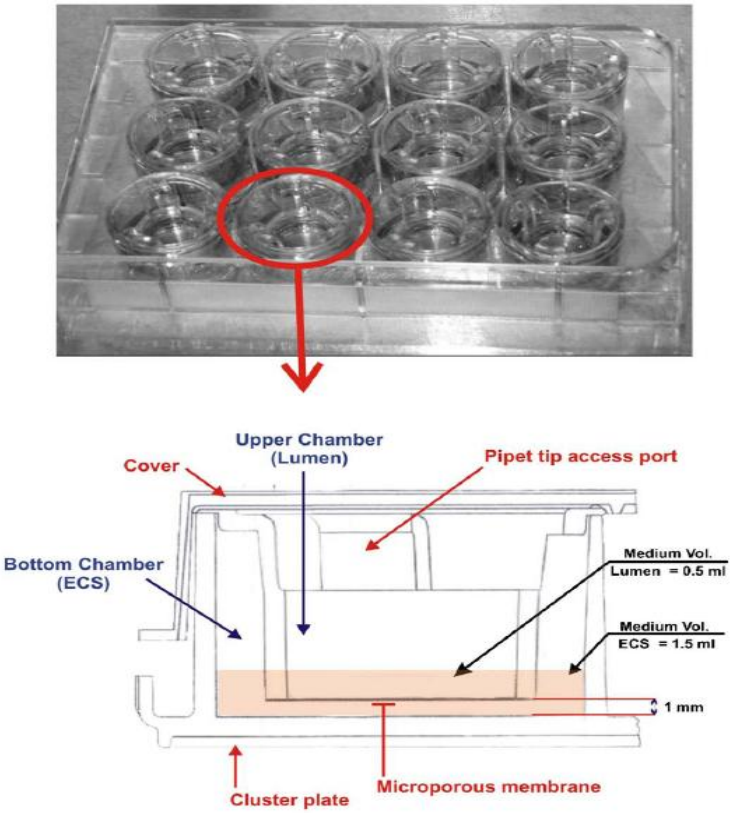

Figure 1.6 Schematic representation of a typical Transwell apparatus. The upper (luminal) chamber and the bottom (abluminal) chamber are separated by a microporous membrane (Santaguida et al., 2006).

To characterize the transport properties of *in vitro* BBB models, the solute permeability coefficient *P* of the *in vitro* BBB was determined by measuring the flux of the selected tracer. The most commonly used cell culture substrate consists of a porous membrane support submerged in the culture medium (Transwell apparatus). The Transwell system is characterized by a horizontal side-by-side or vertical diffusion system (**Fig. 1.6**). During the experiment, the flux of tracers into the abluminal compartment of the Transwell system is recorded as a function of the time and the solute permeability coefficient *P* is calculated from the slope of the flux. The tracers used in the transport experiments are labeled by a fluorescent dye or isotope whose intensity can be

measured quantitatively. Another index, Trans-endothelial Electrical Resistance (TEER), or the ionic conductance of the monolayer, is also a measurement of the "tightness" of the in *vitro* BBB models.

So far, two major types of *in vitro* BBB models have been developed: endothelial cell monolayer and coculture of endothelial cells with glia cells. The cells for these models are basically obtained from primary/sub-passaged or immortalized cell cultures. The origins of the cells are also very diverse: human, primate, bovine, porcine, rodent and murine species.

The brain capillary endothelial cells (BCEC) have been used to establish tissue culture systems ever since the technique of culturing highly purified populations of microvascular cells became available in the early 1980s. The first endothelial monolayers were established using BCEC grown on culture dishes, microcarriers (e.g., dextran beads), and various kinds of filters, including nylon mesh and polycarbonate. These cultured BCEC cells keep their endothelial phenotypes and provides a simple model for study the permeability of the BBB. For instance, they express angiotensin converting enzyme, von Willebrand factor, and internalize accetylated low-density lipoprotein. However, they were reported to lose many BBB-specific features they possessed *in vivo*. For instance, they are lack of specific brain endothelial markers γ-glutamyl transpeptidas (Kondo et al., 1994), marker enzyme alkaline phosphatase(Meyer et al., 1990), and glucose transporter system (Hemmila and Drewes, 1993). Moreover, the permeability of the BCEC monolayer to sucrose was reported to be from 10^{-4} to 10^{-5} cm/s compared with 10^{-6} to 10^{-8} cm/s *in vivo*. The TEER for endothelial monolayer was also found to be pretty low, from 20 to 1,400 $\Omega \cdot$ cm^2, compared with more than 2,000 $\Omega \cdot$ cm^2 *in vivo*. So the BCEC

monolayer alone is not a well-characterized model for the BBB. The major reason for this is the lackness of *in situ* environment and brain-derived signals.

In human body, the BBB are almost completely ensheathed by surrounding tissue, mostly astrocyte foot processes. Experimental result from electron microscopic techniques shows that astrocytes do have significant effects on the formation of the unique BBB phenotype of brain endothelial cells (Abbott, 2002; Haseloff *et al.*, 2005). They induced formation of tight junctions between endothelial cells and increased para-cellular properties of BBB (Arthur *et al.*, 1987).

To better mimic the *in vivo* BBB, a model with coculture of BCEC and astrocyte was devoloped. This coculture model was characterized on the basis of specific cell-type properties and specific BBB properties by electron microscopic evaluation and immohistochemistry methods (Gaillard et al., 2001). The results showed that BCEC displayed (1) characteristic endothelial cell morphology; (2) expression of endothelial cell markers (i.e., CD51, CD62P, CD71 and cadherin 5); (3) tight junction formation between the cells; (4) expression of typical barrier marker γ -glutamyl-transpeptidase (γ -GTP) and P-glycoprotein (Pgp) and transferrin receptor. Astrocytes displayed characteristic astrocyte morphology and expressed glial fibrillary acidic protein (GFAP). Transmission electron microscopy showed evidence of tight junction formation between the endothelial cells and few pinocytic vesicles. A 15-fold increase in γ-glutamyl transpeptidase activity was measured in the endothelial cells cocultured with astrocytes (Demeuse et al., 2002). The permeability of the coculture system to several tracers was reported to be lower than the endothelial monolayer. These results indicate that the coculture system is a better model to study the transport across the BBB.

CHAPTER 2 MATHEMATICAL MODLES FOR THE PERMEABILITY OF THE BBB TO WATER AND NEUTRAL SOLUTES

2.1 Introduction

The BBB strictly regulates mass exchange between peripheral circulation and the CNS due to its unique anatomic structure. **Figure 2.1** shows the three-dimensional (a) and cross-sectional view (b) of the BBB which is drawn based on microscopy studies (Farkas and Luiten. 2001). Transport across the BBB include both paracellular and transcellular pathways (Pardridge, 2005). While large molecules cross the BBB through transcellular pathways, water and small hydrophilic solutes cross the BBB through the paracellular pathway (Hawkins and Davis, 2005). The paracellular pathway of the BBB is formed by the endothelial tight junction openings, the BM filled with extracellular matrix and the openings between adjacent astrocyte foot processes. One objective of this study is to test the hypothesis that in addition to the endothelial tight junctions, the BM and the astrocyte foot processes provide a significant resistance to water and solute transport across the BBB.

The breakdown of the BBB and increased permeability are widely observed in many brain diseases such as stroke, traumatic head injury, brain edema, Alzheimer's disease, AIDS, brain cancer, meningitis, et al. (Dietrich et al., 1994; Fukuda et al., 1995; Baldwin et al., 1996; Barzo et al., 1996; Baskaya et al., 1997; Beaumont et al., 2000; Cernak et al., 2004). Although numerous biochemical factors are found to be responsible for the breakdown of the BBB in disease, the quantitative understanding of how these factors affect the structural components of the BBB to induce BBB leakage is poor. On the other hand, designing therapeutic drugs with better transport properties across the BBB relies greatly on

this understanding. Therefore, another objective of this study is to investigate how the structural components in the paracellular pathway of the BBB affect its permeability to water and solutes through mathematical modeling.

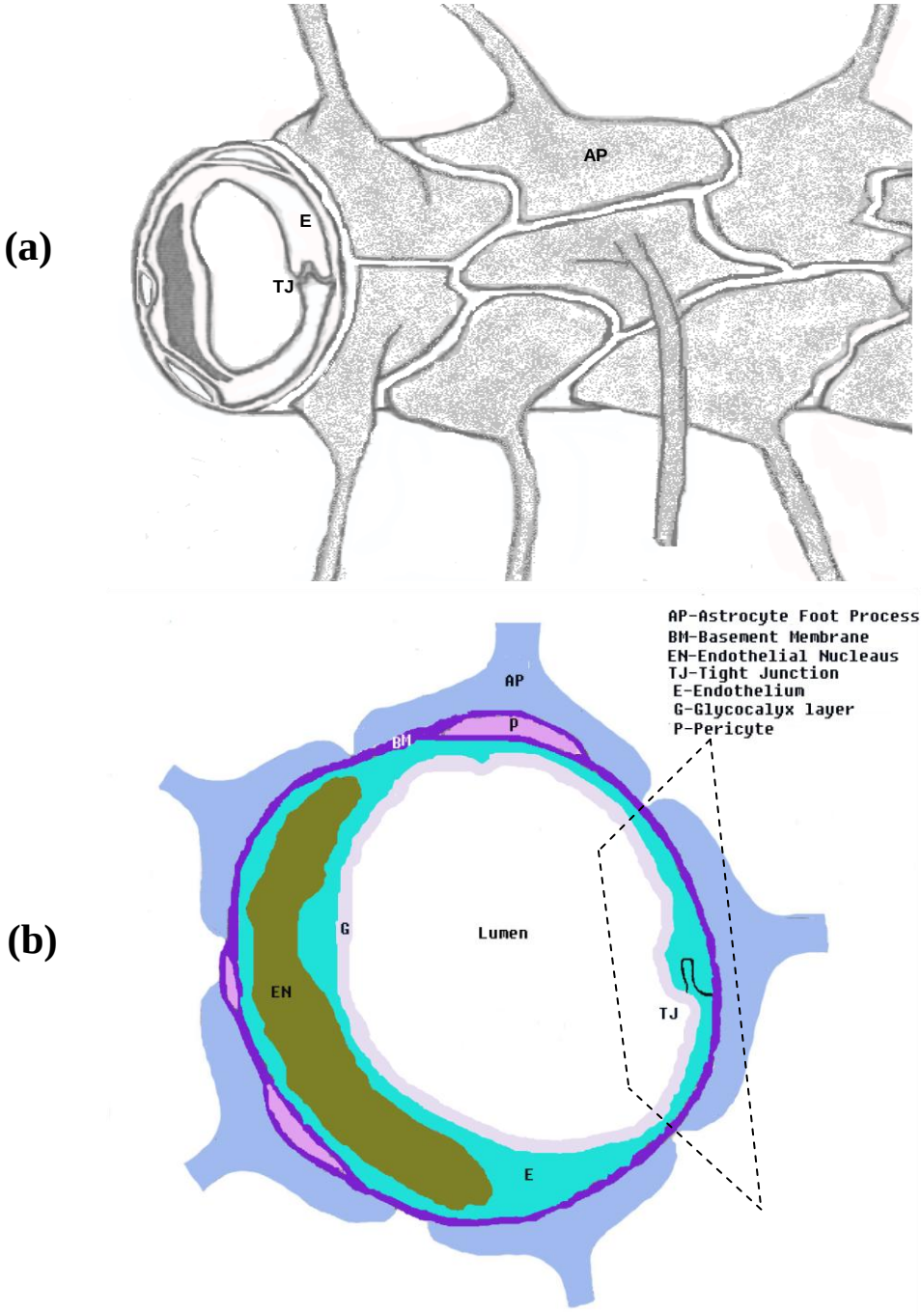

Figure 2.1 The cross-sectional view of the BBB. The dash lined part is the focused region in our model.

Extended from a previous three-dimensional model for studying the transport across the microvessel wall with endothelium only (Fu et al., 1994), our new model for the transport across the BBB included the BM and wrapping astrocyte foot processes. The anatomic parameters for the BBB structural components were obtained from the literature. Before making its predictions, our simplified unidirectional model, which has analytical solutions, was first validated by comparing its results with those from the actual 2-D model (**Appendix A**). In addition, the unknown transport parameters were estimated by comparing the predicted permeability data to various-sized solutes with those of rat pial microvessels measured *in vivo* (Yuan et al., 2009b).

2.2 Model geometry

Figure 2.2 shows our model geometry for the BBB, which is an enlarged view of the dash lined part in **Fig. 2.1(b).** At the luminal side, there is an endothelial SGL with a thickness of L_f. Between adjacent endothelial cells, there is an inter-endothelial cleft with a length of L and a width of 2B. In the inter-endothelial cleft, there is a L_{jun} thick junction strand with a continuous slit-like opening of width $2B_s$. The distance between the junction strand and luminal front of the cleft is L_1. At the tissue side of the cleft, a BM separates the endothelium and the astrocyte foot processes. The thickness of the BM is $2L_b$ and the length of the astrocyte foot processes is $2W_a$. Between adjacent astrocyte foot processes, there is a cleft with a length of L_a and a width of $2B_a$.

Unlike the peripheral microvessel wall, the endothelium of the BBB has negligible large discontinuous breaks in the junction strand of the inter-endothelial cleft and the small slit in the junction strand is assumed continuous (Hawkins and Davis,

2005). As a result, the cross-sectional BBB geometry is the same along the axial direction (y direction in **Fig. 2.2**) and thus the model could be simplified to 2-D (in x, z plane). It could be further simplified to a unidirectional flow in each region due to very narrow clefts and the BM. In addition, the curvatures of the BM and the endothelium can be neglected because their widths are much smaller than the diameter of the microvessel.

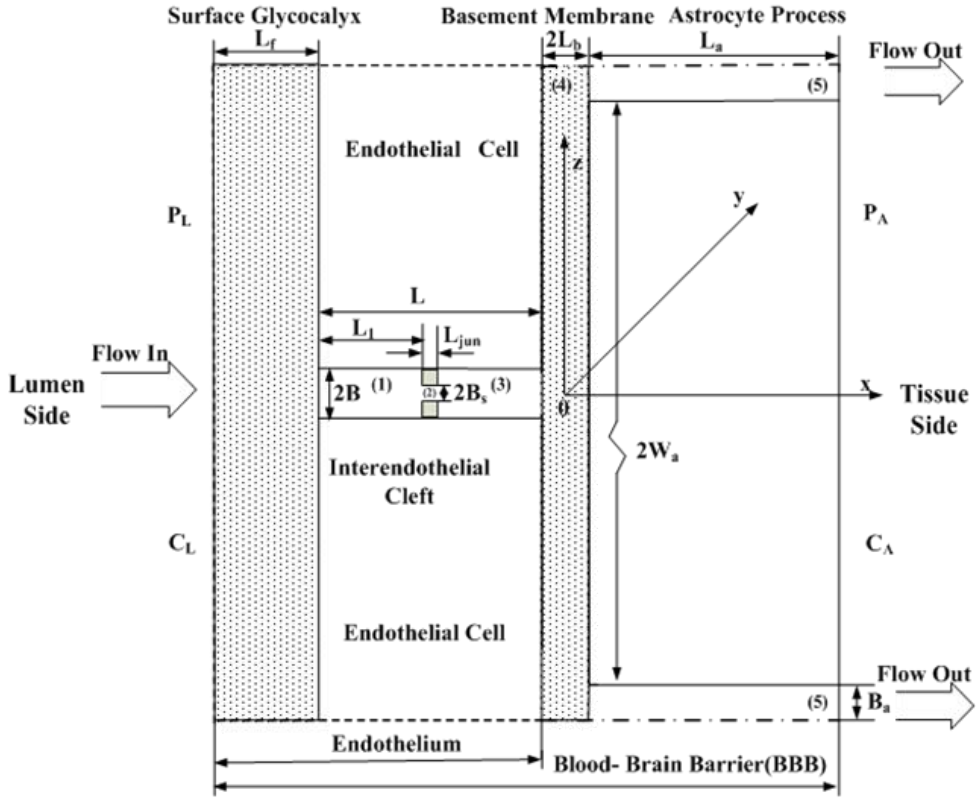

Figure 2.2 Model geometry for the para-cellular pathway of the BBB (not in scale). In our study, the surface glycocalyx layer and the endothelial cells are defined as the Endothelium only while the BBB is defined to include the endothelium, the basement membrane and the astrocytes.

2.3 Hydraulic conductivity L_p

Endothelial Region

In region 1 and 3 of inter-endothelial cleft, the water flow can be approximated by

a Poiseuille channel flow (**Appendix A**) since the width of the inter-endothelial cleft 2B is small compared to both the length of the blood vessel L_v and the depth L of the cleft (see **Table 2.1**). In region 2 of inter-endothelial cleft, the velocity was shown to be very close to Poiseuille profile (within 1.5%) when the Reynolds number is low (less than 0.1) (Dagan *et al.*, 1982). In conclusion, the velocity distribution in all three regions of the inter-endothelial cleft can be considered as Poiseuille flow and expressed as:

$$u^{(i)} = -\frac{B_i^{\,2}}{2\mu} a_i \left(1 - \frac{z^2}{B_i^{\,2}}\right) \qquad \text{i=1, 2, 3} \tag{2.1}$$

Here a_i's are the pressure gradients in different regions of the inter-endothelial cleft and B_i = B when i = 1, 3; $B_i = B_s$ when i = 2.

The pressure in the lumen of microvessel is constant,

$$p = p_L \tag{2.2}$$

A linear 1-D Darcy flow approximation is applied to the SGL (Hu and Weinbaum, 1999). The average velocity along the length of the cleft in the x direction is:

$$\bar{u} = \frac{K_p}{\mu} \frac{p_L - p^{(1)}(-L - L_b)}{L_f} \tag{2.3}$$

Here K_p is the Darcy permeability in the SGL, μ, the viscosity, $p^{(1)}(-L - L_b)$ the pressure at the interface between the SGL and the interendothelial cleft, and L_f is the SGL thickness.

Basement membrane

The flow in the BM is approximated to be unidirectional (**Appendix A**) and the velocity profile can be obtained by solving the Brinkman equation with the non-slip boundary condition at the surface $x = \pm L_b$

$$w^{(4)} = -\frac{K_b}{\mu} a_4 (1 - \frac{\cosh(x/\sqrt{K_b})}{\cosh(L_b/\sqrt{K_b})}) \tag{2.4}$$

Here a_4 is the pressure gradient in the BM, K_b is the Darcy permeability in BM.

Astrocyte Region

Similarly, flow in the cleft between astrocyte foot processes can also be approximated as the Poiseuille flow. The velocity profile is

$$u^{(5)} = -\frac{B_a^{\ 2}}{2\mu} a_5 (1 - \frac{[z - (W_a + B_a)]^2}{B_a^2}) \tag{2.5}$$

Here a_5 is the pressure gradient.

The pressure in the brain tissue p_A is constant,

$$x = L_a + L_b \qquad p^{(5)} = p_A \tag{2.6}$$

Equations 2.1, 2.3, 2.4 and 2.5 were solved simultaneously for the pressure and velocity in each region with the boundary conditions (2.2) and (2.6) and continuity boundary conditions for the pressure and volume flow rate at the interfaces between different regions of the BBB. The hydraulic conductivity L_p was obtained similar to the procedure used by Fu et al. (Fu and Chen, 2003).

$$L_p = \frac{Q_L}{p_L - p_A} \frac{L_{jt}}{L_v} \tag{2.7a}$$

where Q_L is the volume flow rate through the vessel with length L_v which is obtained by integration of $u^{(1)}$ the cross-sectional area of the cleft with width 2B and length L_v (**Appendix A**). L_{jt} is the total length of the cleft per unit surface area of microvessel wall and it equals to $1/\pi D_v$. Finally, L_p was calculated as,

$$L_p = \frac{1}{R_f + R_1 + R_2 + R_3 + R_4 + R_5} \frac{1}{\pi D_v} \tag{2.7b}$$

Here R_f and R_i (i=1,2,3,4,5) are the resistances of SGL and each region of the BBB:

$R_f = \mu L_f / (2K_p B)$, $R_1 = 3\mu L_1 / (2B^3)$, $R_2 = 3\mu L_{jun} / (2B_s^3)$,

$R_3 = 3\mu(L - L_1 - L_{jun}) / (2B^3)$, $R_4 = \mu W_a / [4K_b (L_b - \sqrt{K_b} \tanh(L_b / \sqrt{K_b})]$,

$R_5 = 3\mu L_a / (2B_a^3)$.

2.4 Diffusive permeability P

The governing equation for diffusion of a hydrophilic solute is,

$$\Delta C = 0 \tag{2.8}$$

Since the width of the inter-endothelial cleft is very small compared with its length, diffusion of the solute can be simplified to 1-D in all the clefts. The concentration in the lumen of the microvessel C_L and that in the tissue C_A are constants. Solving **Eq. 2.8** with these boundary conditions and continuity boundary conditions for the concentration and the solute flow rate at the interfaces between different regions of the BBB, we obtained the concentration distribution in each region $C^{(i)}$, i=f,1,2,3,4,5. The diffusive permeability P is defined as,

$$P = \frac{Q_L^s}{C_L - C_A} \frac{L_{jt}}{L_v} \tag{2.9}$$

The solute flow rate Q_L^s was obtained by integrating $D_s^c \frac{\partial C^{(1)}}{\partial x}$ over the cross-sectional area of the cleft with width 2B and length L_v (**Appendix A**). The P of the BBB was calculated as,

$$P = \frac{1}{R'_f + R'_1 + R'_2 + R'_3 + R'_4 + R'_5} \frac{1}{\pi D_v} \tag{2.10}$$

Here R'_f and R'_i (i=1,2,3,4,5) are the resistances of the SGL and each region of the BBB to solute transport: $R'_f = L_f / (2BD_s^f)$, $R'_1 = L_1 / (2BD_s^c)$, $R'_2 = L_{jun} / (2B_s D_s^{sl})$, $R'_3 = (L - L_1 - L_{jun}) / (2BD_s^c)$, $R'_4 = W_a / (4L_b D_s^b)$, $R'_5 = L_a / (2B_a D_s^a)$. $D_s{}^f$, $D_s{}^c$, $D_s{}^{sl}$, $D_s{}^b$, and $D_s{}^a$ are effective solute diffusion coefficients in the SGL, inter-endothelial cleft, small silt in the junction strand, BM, and the cleft between astrocyte foot processes, correspondingly.

2.5 Model parameters

All the anatomical and transport parameters for the BBB are listed in **Table 2.1** and **Table 2.2** respectively. The anatomical parameters were based on the electron microscopy observations of rat brain microvessels or mesenteric microvessel.

In the SGL, the effective diffusion coefficients of *species i* are calculated using the following equations (Ogston *et al.*, 1973; Michel and Curry, 1999; Sugihara-Seki and Fu, 2005)

$$D_s^f = D_s^{free}[1 - V_f{}^{0.5}\left(1 + \frac{2r_s}{\pi^{0.5} r_f}\right)]\phi \tag{2.11}$$

$$\phi = 1 - V_f \left(1 + \frac{r_s}{r_f}\right)^2 \tag{2.12}$$

Here D_s^{free} is the solute diffusion coefficient in a free aqueous solution, r_s is the radius of the solute, r_f is the radius of the fiber and V_f the fiber volume fraction. ϕ is the solute partition coefficient, which describes the steric exclusion of the fiber to the solute. The

other term in Eq. 2.11 describes the diffusion resistance of the fiber to the solute.

In the BM, the effective solute diffusion coefficient includes both the effect from the fiber matrix and the cleft. Compared to the SGL, there is an additional drag on the molecule moving within the cleft relative to movement in free solution, and the steric exclusion at the cleft entrance ϕ_b (Ogston *et al.*, 1973; Weinbaum *et al.*, 1992; Michel and Curry, 1999; Sugihara-Seki and Fu, 2005).

$$D_s^b = D_s^{free}\left[1 - {V_f}^{0.5}\left(1 + \frac{2r_s}{\pi^{0.5} r_f}\right)\right]\phi\left(1 - 1.004\beta_b + 0.418\beta_b^3 + 0.210\beta_b^4 - 0.169\beta_b^5\right)\phi_b \quad (2.13)$$

$$\beta_b = \frac{r_s}{L_b}, \quad \phi_b = 1 - \beta_b \quad (2.14)$$

Here L_b is the half width of the BM.

In the cleft regions 1,2,3,5, the effective diffusion coefficients of *species i* in region *n* is calculated using the following equation(Ogston *et al.*, 1973; Weinbaum *et al.*, 1992; Michel and Curry, 1999; Sugihara-Seki and Fu, 2005),

$$D_s^{(n)} = D_i^{free}(1 - 1.004\beta_n + 0.418\beta_n^3 + 0.210\beta_n^4 - 0.169\beta_n^5)\phi_n \qquad n = 1,2,3,5 \quad (2.15)$$

$$\beta_n = \frac{r_s}{W_n}, \quad \phi_n = 1 - \beta_n \quad (2.16)$$

Here $D_s^{(n)} = D_s^c$ when n=1, 3; $D_s^{(2)} = D_s^{sl}$ when n=2; $D_s^{(5)} = D_s^a$ when n=5. W_n is the half width of cleft which equals to B, B_s and B_a for $n = 1, 3; 2; 5$ respectively. ϕ_n is the solute partition coefficient at the cleft entrance, which describes the steric exclusion of the cleft to the solute. The other term in Eq. 2.15 describes the additional drag on the solute moving within the cleft relative to the movement in a free solution.

Table 2.1 Anatomical parameters of the BBB

Microvessel	Diameter (Farkas and Luiten, 2001)	D_v	10,000nm
Endothelium	Glycocalyx layer thickness (Adamson and Clough, 1992; Vink and Duling, 1996)	L_f	100-400nm
	Gap spacing between fibers of glycocalyx (Squire et al., 2001; Weinbaum et al., 2003)	Δ	8nm
	Glycocalyx fiber radius (Squire et al., 2001; Weinbaum et al., 2003)	r_f	6nm
	Fiber volume fraction of the glycocalyx layer (Squire et al., 2001; Weinbaum et al., 2003)	V_f	0.326
	Total length of the cleft region (Schulze and Firth, 1992)	L	700nm
	Distance between the tight junction strand and the front of the inter-endothelial cleft	L_1	350nm
	Width of inter-endothelial cleft (Adamson et al., 2004)	2B	18nm
	Width of the small slit of the tight junction strand (Allt and Lawrenson, 1997; Cassella 1997)	$2B_s$	1-10nm
	Thickness of tight junction strand (Adamson et al., 2004)	L_{jun}	11nm
Basement membrane	Thickness of the basement membrane (Paulson and Newman, 1987; Farkas and Luiten, 2001)	$2L_b$	20-80nm
Astrocyte	Thickness of astrocyte foot processes (Farkas and Luiten, 2001)	L_a	1000nm
	Width of the cleft between astrocyte foot processes (Farkas and Luiten, 2001)	$2B_a$	5-2000nm
	Length of astrocyte foot processes (Farkas and Luiten, 2001)	$2W_a$	5000nm

Table 2.2 Transport parameters for water and solutes across the BBB

Water Transport	Darcy permeability of surface glycocalyx (Guo et al., 2000; Weinbaum et al., 2003)	K_p	$3.16\ nm^2$	
	Viscosity (Zhang et al., 2006a)	μ	7.0×10^{-4} kg/m/s	
Solute Transport (NaFl)	Free diffusion coefficient in aqueous solution (Fu et al., 1995)	D_s^{free}	5.62×10^{-6} cm^2/s	
	Effective diffusion coefficient in the surface glycocalyx layer (Michel and Curry, 1999; Sugihara-Seki and Fu, 2005)	D_s^{f}	1.33×10^{-6} cm^2/s	
	Effective diffusion coefficient in inter-endothelial cleft (Michel and Curry, 1999; Sugihara-Seki and Fu, 2005)	D_s^{c}	5.05×10^{-6} cm^2/s	
	Effective diffusion coefficient in the small slit of the junction strand (Michel and Curry, 1999; Sugihara-Seki and Fu, 2005)	D_s^{sl}	$2B_s=1.0$	$2.47\times10^{-7}cm^2/s$
			$2B_s=10$	$4.65\times10^{-6}cm^2/s$
	Effective diffusion coefficient in the basement membrane(Michel and Curry, 1999; Sugihara-Seki and Fu, 2005)	D_s^{b}	$2L_b=20nm$	$1.21\times10^{-6}cm^2/s$
			$2L_b=80nm$	$1.30\times10^{-6}cm^2/s$
	Effective diffusion coefficient in the cleft between astrocyte foot processes(Michel and Curry, 1999; Sugihara-Seki and Fu, 2005)	D_s^{a}	$2B_a=5nm$	$3.79\times10^{-6}cm^2/s$
			$2B_a=2000nm$	$5.61\times10^{-6}cm^2/s$

2.6 Results

Comparison of the model predictions with measured permeability data

All the anatomical data can be found from the literature (**Table 2.1**) except the fiber density and structure in the BM. In **Fig. 2.3a**, we plotted the model predictions for the solute permeability P by assuming that the fiber matrix in the BM is the same as that in the SGL, i.e., the solute diffusion coefficient in the BM D_s^b is the same as that in the

SGL D_s^f, $D_s^b=D_s^f$ (solid line); or looser ($D_s^b=2D_s^f$, dashed line); or denser than that in the SGL ($D_s^b=0.5D_s^f$, dotted line). Comparing the model predictions with *in vivo* data from rat pial microvessels (Yuan et al., 2009b), we can see that the best fit is when the fiber matrix in the BM has the same transport property as that in the SGL (solid line). **Figure 2.3b** shows the model predictions for the solute permeability P as a function of solute size for the endothelium only model and for the BBB model. B_s, the half width of the endothelial tight junction opening, varies in cerebral microvessels located at different regions of the brain (Allt & Lawrenson, 1997). We chose B_s = 2, 3, 4 nm, which are for pial microvessels at the brain surface. Other parameters were fixed as in **Table 2.1**. From **Fig. 2.3b**, we can see that all the measured P of rat pial microvessels are very close to the predicted P of the BBB while they have large deviations from the predicted P for the endothelium only.

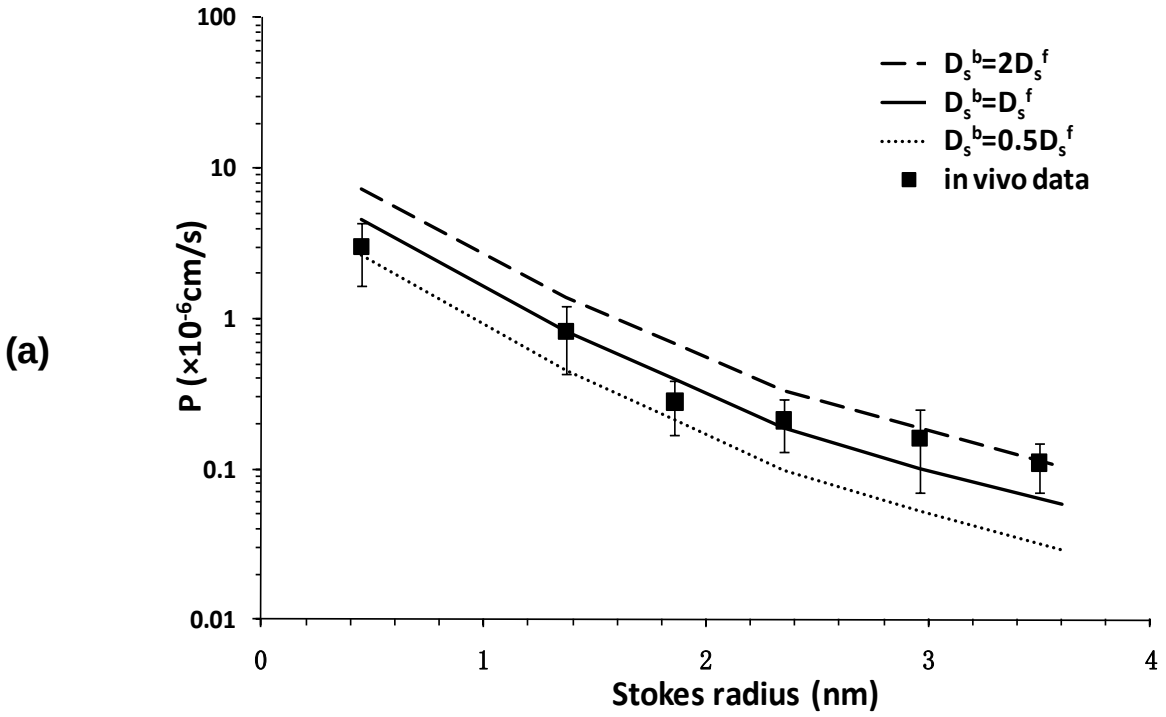

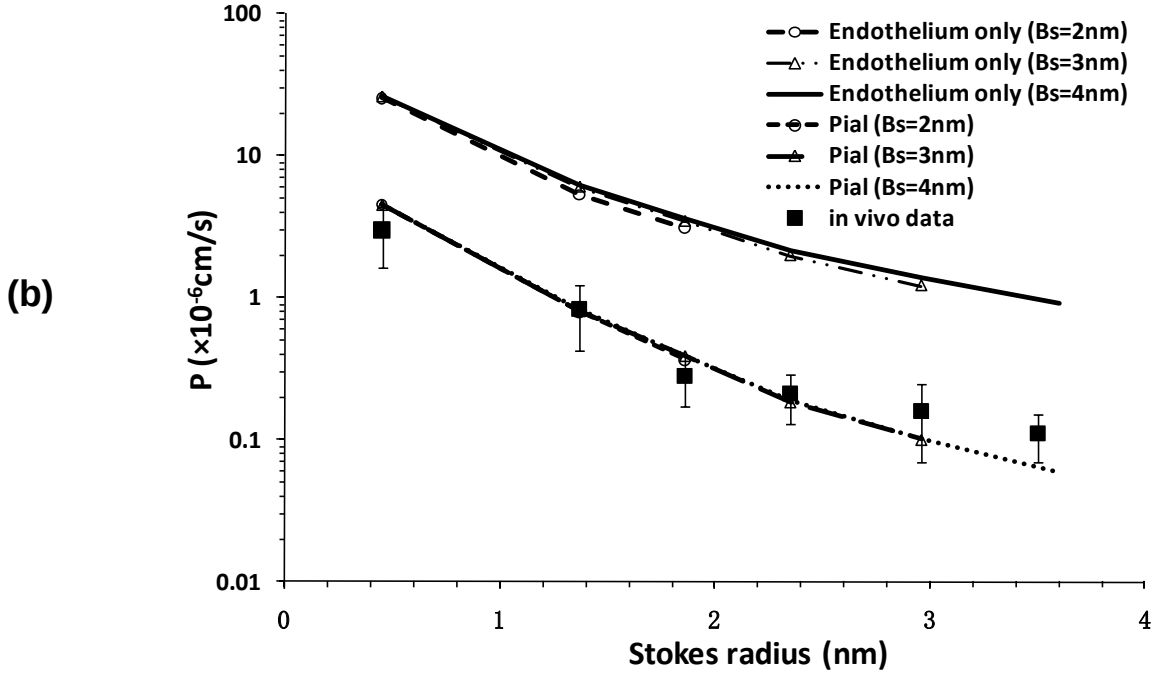

Figure 2.3 (a) Comparison of the model predictions for P of the BBB with the measured data when changing the solute diffusion coefficients in the BM D_s^b : D_s^b =$2D_s^f$ (dashed line, for a looser fiber matrix compared to that in the SGL), D_s^b = D_s^f (solid line, for the same fiber matrix compared to that in the SGL) and D_s^b = $0.5D_s^f$ (dotted line, for a denser fiber matrix compared to that in the SGL). **(b)** Comparison of model predictions with *in*

vivo experimental data for the permeability (P) of rat pial microvessels to all the solutes (Yuan, et al., 2009): sodium fluorescein (NaFl), Dextrans-4K, -10K, -20K, -40K and -70K, when the half width of the small slit in the junction strand, B_s , changes from 2 to 4 nm, the possible values in the rat pial microvesels. The upper 3 lines are the model predictions when considering transport across the endothelium only, while the lower 3 lines are those when considering transport across the entire BBB. For both cases, L_f=100nm, L_b=10nm, B_a=15nm and $D_s^b = D_s^f$. Filled squares are experimental data.

Effects of B_s and the fiber density of the BM on L_p and P^{NaFl}

For peripheral microvessels, the endothelial tight junction opening is dominant in controlling hydraulic conductivity L_p and small solute permeability such as P^{NaFl}. In addition to the tight junction, the BM and astrocytes of the BBB may also contribute to L_p and P^{NaFl}. **Figure 2.4** shows the model predictions for L_p (**Fig. 2.4a**) and P^{NaFl} (**Fig. 2.4b**) as a function of tight junction opening B_s when the BM has different fiber densities. K_b and D_s^b are respective Darcy permeability and NaFl diffusion coefficient in the BM. When the fiber density in the BM is the same as that in the SGL, K_b=3.16cm^2 and D_s^b=1.21×10^{-6}cm^2/s. The dashed lines in **Fig. 2.4** show the case of peripheral microvessels with only endothelium. When B_s increases from 0.5nm to 2nm, L_p will increase by ~20-fold and P^{NaFl} by 4.5-fold. In contrast, when the endothelium is wrapped by the BM and the astrocytes as for the BBB, increase in B_s from 0.5nm to 2nm only induces 5-fold increase in L_p and 1.6-fold increase in P^{NaFl} when the fiber density in the BM is the same as that in the SGL (dash-dot-dash line). If the fiber density in the BM is 10 times of that in the SGL, the increase is only 1.6-fold in L_p and 1.1-fold in P^{NaFl} when the B_s increases from 0.5nm to 2nm (solid line), while if the fiber density in the BM is 1/10 of that in the SGL, the increase is 12-fold in L_p and 2.8-fold in P^{NaFl} respectively (solid line). Even at a large B_s of 5nm, when the BM is filled with the same density fibers as in the SGL, the BBB permeability is only 17% of that of endothelium only. This

percentage can be as low as 2% if the fiber density in the BM is 10 times of that in the SGL.

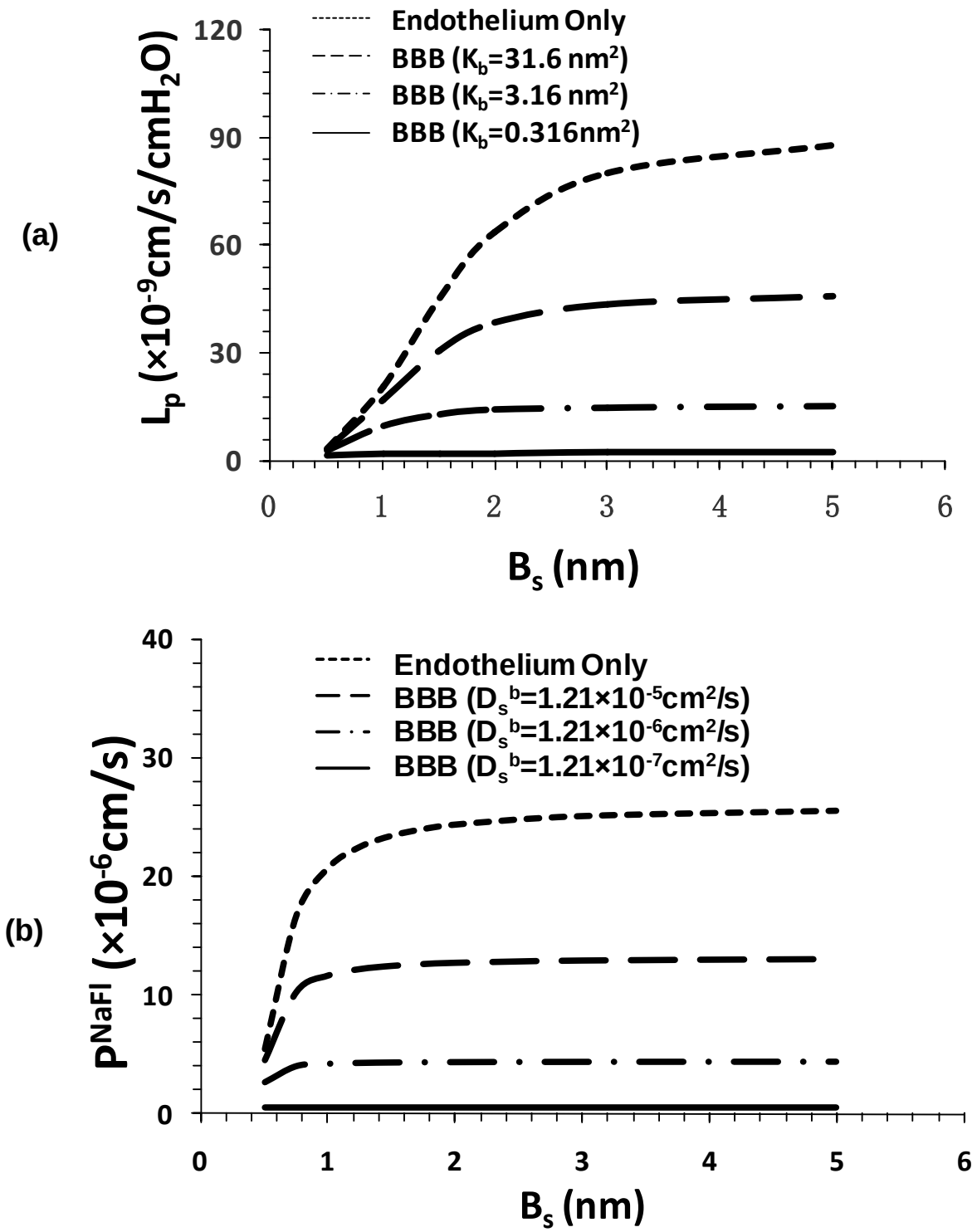

Figure 2.4 Model predictions for **(a)** hydraulic conductivity L_p and **(b)** the permeability to NaFl, P^{NaFl}, as a function of B_s, the half width of the small slit in the junction strand under two cases: when considering transport across the endothelium only (Endothelium only, short dashed lines), and when considering transport across the entire BBB (BBB). In the BBB case, three different fiber densities were considered for the basement

membrane: the same as the fiber density in the surface glycocalyx layer (K_b=3.16cm^2, D_s^b =1.21×10^{-6}cm^2/s, the dash-dot-dash line), ten times lower (K_b=31.6cm^2, D_s^b=12.1×10^{-6}cm^2/s, the dashed line) and higher (K_b=0.316cm^2, D_s^b =0.121×10^{-6}cm^2/s, the solid line). For all the cases, L_f=100nm, L_b=10nm, B_a=15nm.

Effect of L_f on L_p and P^{NaFl}

Figure 2.5 shows the model predictions for L_p (**Fig. 2.5a**) and P^{NaFl} (**Fig. 2.5b**) as a function of the endothelial surface glycocalyx layer thickness L_f. The dashed line is for the case of endothelium only while the solid line for that of the BBB. We can see from **Fig. 2.5**, decrease in L_f from 400 to 0 nm increases L_p and P^{NaFl} by 3-fold in the case of endothelium only, while in the case of the BBB, the increase is only 25% in both L_p and P^{NaFl} with the protection of the BM and the astrocytes.

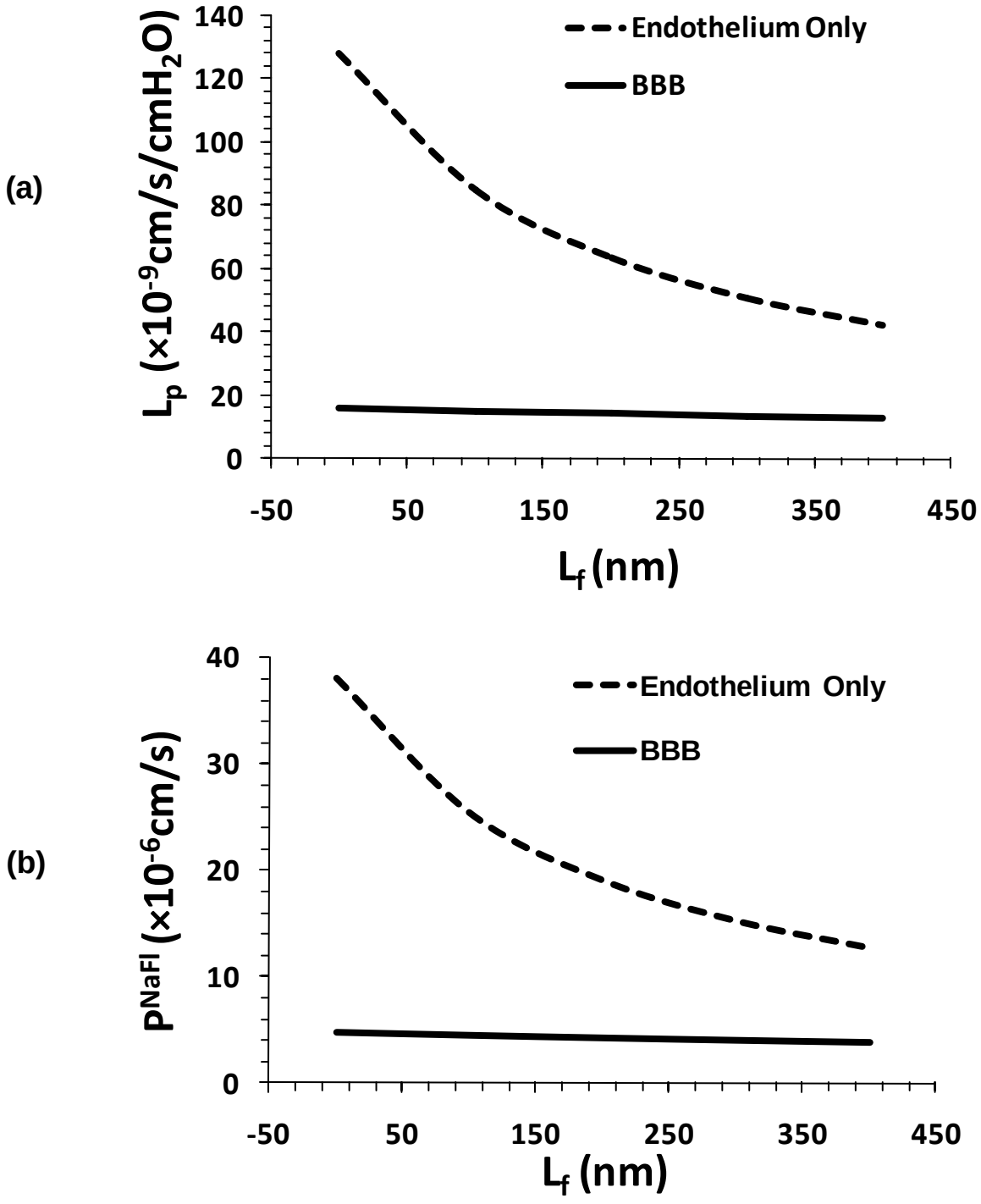

Figure 2.5 Model predictions for **(a)** hydraulic conductivity L_p and **(b)** the permeability to NaFl, P^{NaFl} as a function of the endothelial glycocalyx layer thickness L_f under two cases: when considering transport across the endothelium only (Endothelium only, the dashed line), and when considering transport across the entire BBB (BBB, the solid line). For both cases, B_s=2nm, L_b=10nm, B_a=15nm.

Effect of L_b on L_p and P^{NaFl}

Figure 2.6 shows the model predictions for L_p (**Fig. 2.6a**) and P^{NaFl} (**Fig. 2.6b**) as a function of the basement membrane thickness $2L_b$. The dashed line is for the rat pial microvessel with a larger tight junction opening B_s~2nm while the solid line is for the cerebral microvessel in the brain parenchyma, which may have a B_s as small as ~0.5nm (Allt and Lawrenson, 1997). The BM half thickness L_b is 10-20nm under normal conditions (Farkas and Luiten, 2001). It may become larger in disease. We can see from **Fig. 2.6** that for the cerebral microvessel with the tighter junction, increase in L_b from 10 to 40nm only induces 10% increase in L_p and 50% increase in P^{NaFl}, while it induces L_p increase by 2.7-fold and P^{NaFl} increase by 2.3-fold for the pial microvessel with the looser tight junction.

Effect of B_a on L_p and P^{NaFl}

Figure 2.7 shows the model predictions for L_p (**Fig. 2.7a**) and P^{NaFl} (**Fig. 2.7b**) as a function of the half width B_a of the cleft between astrocyte foot processes. The dashed line is for the rat pial microvessel while the solid line for the cerebral microvessel. We can see from **Fig. 2.7** that for both pial and cerebral microvessels, L_p and P^{NaFl} are not sensitive to the change in B_a when B_a is from 10 to 1000nm. The increase in L_p is only 1% and that in P^{NaFl} is 9% for the cerebral microvessel while it is 5% in L_p and 15% in P^{NaFl} for the pial microvessel. However, when B_a is from 2.5 to 10nm, the increase in L_p can be as large 4-fold and that in P^{NaFl} can be 1.6-fold.

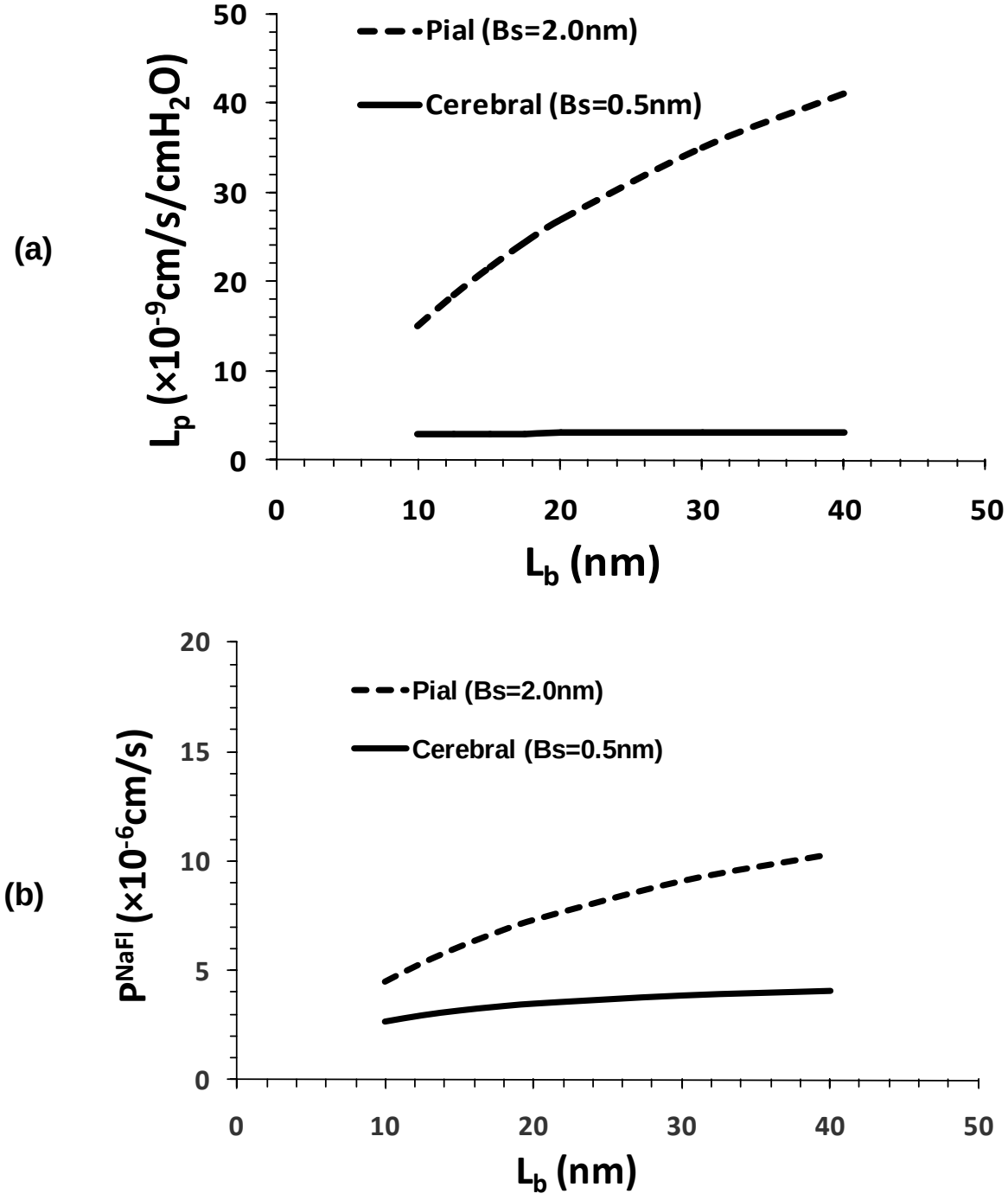

Fig. 2.6 Model predictions for **(a)** hydraulic conductivity L_p and **(b)** the permeability to NaFl, P^{NaFl}, as a function of L_b, the half width of the basement membrane. Two cases are considered: pial microvessels when B_s=2nm (the dashed line) and tighter cerebral microvessels when B_s=0.5nm (the solid line). For both cases, L_f=100nm, B_a=15nm.

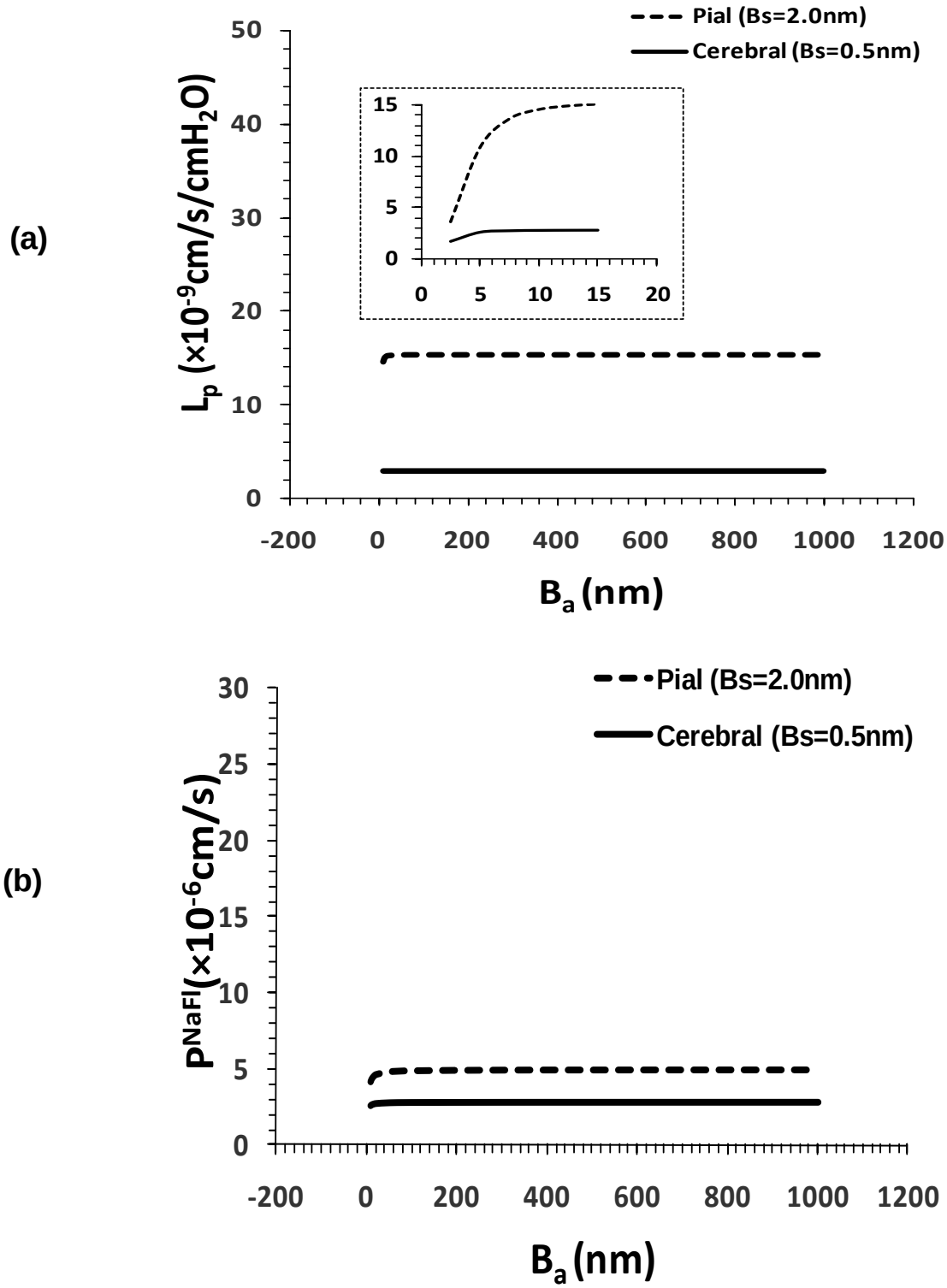

Fig. 2.7 Model predictions for **(a)** hydraulic conductivity L_p and **(b)** the permeability to NaFl, P^{NaFl}, as a function of B_a, the half width of the cleft between astrocyte foot processes. The insets show the results when B_a increases from 2.5 to 15nm. Two cases are considered: pial microvessels when B_s=2nm (the dashed line) and tighter cerebral

microvessels when B_s=0.5nm (the solid line). For both cases, L_f=100nm, L_b=10nm.

Sensitivity analysis

Sensitivity analysis is performed for various anatomical parameters and the results for L_p and P^{NaFl} are shown in Table 2.3 and 2.4 respectively. The value of each parameter is increased and decreased by 10% and the corresponding permeability is normalized compared to the control case (B=9nm, L=700nm, L_1=350nm, L_{jun}=11nm, L_a=1000nm, W_a=2500nm, D_v=10000nm). Two different types of brain microvessel are considered: cerebral and pial microvessels. From Table 2.3 and 2.4, we can see that both L_p and P^{NaFl} are not very sensitive to changes in B, L, L_1 and L_a. For $\mathbf{L_{jun}}$, its value change ~9% and 4% for L_p and $\mathbf{P^{NaFl}}$ respectively in cerebral microvessel while its change is less than 0.7% in pial microvessel. This result is reasonable since cerebral microvesels are much tighter than pial microvessels and thus the tight junctions of cerebral microvessels provide a larger resistance to water and solute transport than that of pial microvessel . For W_a, its value change ~2% and 5% for L_p and $\mathbf{P^{NaFl}}$ respectively in cerebral microvessel while its change is 6-9% in pial microvessel. For D_v, when its values increases by 10% both Lp and $\mathbf{P^{NaFl}}$ decreases by 9% while when its values decreases by 10% both Lp and $\mathbf{P^{NaFl}}$ increases by 11%.

Table **2.3** Sensitivity analysis of anatomical parameters for normalized L_p

Parameters	Control Values (nm)	Normalized L_p			
		Cerebral (B_s=0.5nm)		Pial (B_s=2.0nm)	
		+10%	-10%	+10%	-10%
B	9	100.33%	99.54%	101.79%	97.60%
L	700	99.91%	100.09%	99.52%	100.49%
L_1	350	100.00%	100.00%	100.00%	100.00%
L_{jun}	11	92.44%	109.12%	99.32%	100.69%
L_a	1000	99.97%	100.03%	99.85%	100.15%
W_a	2500	98.51%	101.53%	92.50%	108.83%
D_v	10000	90.91%	111.11%	90.91%	111.11%

Table **2.4** Sensitivity analysis of anatomical parameters for normalized P^{NaFl}

Parameters	Control Values (nm)	Normalized P^{NaFl}			
		Cerebral (B_s=0.5nm)		Pial (B_s=2.0nm)	
		-10%	+10%	-10%	+10%
B	9	101.00%	98.79%	101.63%	98.05%
L	700	99.33%	100.68%	98.92%	101.10%
L_1	350	100.00%	100.00%	100.00%	100.00%
L_{jun}	11	96.25%	104.06%	99.90%	100.10%
L_a	1000	99.45%	100.56%	99.11%	100.90%
W_a	2500	95.68%	104.73%	93.18%	107.90%
D_v	10000	90.91%	111.11%	90.91%	111.11%

Resistances from different regions of the BBB

To investigate the contribution of different regions of the BBB to water and solute transport, the ratios between resistance from each region of the BBB and the total resistance to water and NaFl were calculated and listed in **Table 2.5**. Here NaFl is used as the test solute and two cases were considered: cerebral (B_s=0.5nm) and pial (B_s=2nm) microvessel. From Table 2.5 we can see that, in cerebral microvessel, tight junction (region 2 of inter-endothelial cleft) and basement membrane are the major contributors for resitance. For water, the resistance from tight junction is the largest (82.66%) while for NaFl, BM provides the largest resistance (45.12%). We can also see that, in pial microvessel, BM is the major contributor for both water (80.90%) and NaFl (73.22%) transport.

Table **2.5** The ratio of resistance from each region of the BBB (R_n, n=f,1,2,3,4,5) to the total resistance R_T for water and test solute (NaFl)

Resistance Percentage (R_n/R_T)		SGL	Inter-endothelial cleft (region 1)	Inter-endothelial cleft (region 2)	Inter-endothelial cleft (region 3)	BM	Cleft between astrocyte processes
Water	Cerebral (B_s=0.5nm)	1.10%	0.45%	82.66%	0.44%	15.08%	0.28%
	Pial (B_s=2nm)	5.91%	2.42%	6.93%	2.34%	80.90%	1.49%
NaFl	Cerebral (B_s=0.5nm)	3.66%	3.36%	39.08%	3.25%	45.12%	5.52%
	Pial (B_s=2nm)	5.93%	5.45%	1.15%	5.28%	73.22%	8.96%

Comparison of 1-D and 2-D models

We first validated our simplified unidirectional model by comparing its results

with those from the 2-D model in **Appendix A**. **Figure 2.8** shows that the simplified unidirectional model would overestimate the BBB resistance to water by less than 5% and that to the solutes under study by less than 2%.

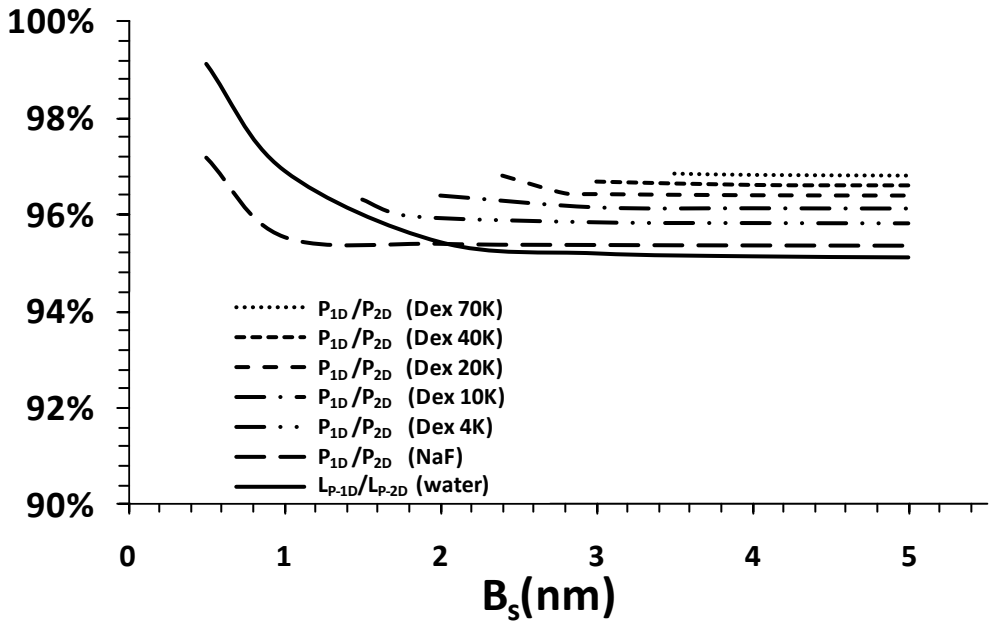

Fig. 2.8 The ratios of the BBB permeability when using the unidirectional model for the BBB ($L_{p\text{-}1D,}$ P_{1D}) to that when using 2-D model ($L_{p\text{-}2D}$, P_{2D}) for water and six solutes: NaFl, Dextrans-4K, -10K, -20K, -40K and -70K.

2.7 Discussion

For simplicity, the transport in the endothelial SGL was considered as a 1-D Darcy flow for the water and as a 1-D diffusion for the solute instead of 2-D in the real case (**Fig. 2.2**). We also approximated a unidirectional flow in the clefts and in the BM by neglecting the 2-D effects in the small entrance/exit regions (**Fig. A2**). To validate this simplicity, we compare the L_p calculated using a 2-D Darcy flow and a more real 2-D Brinkman flow ($L_{p\text{-}2D}$), which satisfies the non-slip boundary condition at the endothelial cell surface, with that calculated using the 1-D flow ($L_{p\text{-}1D}$). We also compare the solute permeability P calculated using the 2-D diffusion ($P_{2\text{-}D}$) with that using the 1-D diffusion

($P_{1\text{-}D}$). Appendix A shows the detailed 2-D model. **Figure 2.8** shows the comparison as a function of the tight junction opening $2B_s$. The solid line is for $L_{p\text{-}1D}$/ $L_{p\text{-}2D}$. We can see that for all the B_s, the underestimation in L_p by using $L_{p\text{-}1D}$ is less than 5% compared to that using the 2-D Darcy or Brinkman equation. The long dashed line is $P_{1\text{-}D}/P_{2\text{-}D}$ for NaFl, the dash-dot-dot-dash line for dextran-4k, the dash-dot-dash line for dextran-10K, the medium dashed line for dextran-20k, the short dashed line for dextran-40k and the dotted line for dextran-70k. We can see that the underestimation in P by using the P_{1D} for the solutes used in our experiments is less than 2% for all the B_s, compared to that using the 2-D diffusion. Therefore, our simplified unidirectional approximation is valid for the reason that the resistance of the SGL to water and solutes is very small compared to the rest part of the BBB, and the clefts and the BM are very narrow with negligible 2-D entrance/exit regions.

Two structural features that distinguish the BBB from the peripheral microvessel are that the endothelium is ensheathed by the astrocyte foot processes and there is a very thin BM layer sandwiched between the endothelium and astrocytes. Our model predicts that they play a crucial role in maintaining the low and stable permeability of the BBB to water and solutes, in addition to the endothelial tight junctions. When the tight junction opening is very small (< 0.5 nm), the BM and astrocytes contribute to 3%-90% of the total resistance to water and small solute transport, depending on the fiber density in the BM. While when the tight junction opening becomes larger for the cerebral microvessels at different locations of the brain, or is increased in disease or by therapeutic agents, the BM and astrocytes contribute to as large as 98% of the total resistance to water and small solute transport when the fiber density of the BM is 10 times of that in the SGL. They

contribute to 83% of the total resistance when the fiber density of the BM is the same as that in the SGL. Even when the fiber density of the BM is only 1/10 of that in the SGL, which occurs in pathological states (Rosenberg et al., 1993; Rascher et al., 2002), the BM and astrocytes would contribute to 49% of the total resistance to water and small solute transport.

In addition to the fiber density of the BM, the thickness of the BM is crucial in determining the BBB permeability especially when the tight junction opening becomes large. Increase in the thickness of the BM from 20 to 80nm would increase the pial microvessel permeability to water and small solutes up to 2.7-fold. On the contrary, the gap spacing between the astrocyte foot processes, which is normally larger than 10nm, has minor influence on the BBB permeability.

The endothelial SGL constantly experiences the chemical and mechanical factors carried by the circulating blood. It may be degraded by these blood-born factors. In the BBB, the BM and the astrocyte foot processes can prevent the permeability increase due to the SGL damage and maintain the stability of the BBB permeability.

In summary, our model indicates that the BM and the astrocyte foot processes ensheathing the endothelium provide a significant resistance to water and solute transport across the BBB in addition to the endothelial tight junction. They play a pivotal role in maintaining the low permeability of the BBB, especially when the endothelial tight junction barrier and surface glycocalyx are compromised. In addition to elucidating how different components of the BBB contribute to maintain the low BBB permeability to water and hydrophilic solutes, our simplified model with the analytical solutions can be easily applied to predict the most likely structural changes when the BBB permeability is modulated in

disease. This will help in finding the targets for the treatment. Furthermore, it can be used to quantify the drug transport under controlled regulation of the BBB permeability.

CHAPTER 3 AN ELECTRO-DIFFUSION MODEL FOR THE BLOOD-BRAIN BARRIER PERMEABILITY TO CHARGED MOLECULES

3.1 Introduction

The major structural components of the BBB include endothelium, basement membrane (BM), and astrocyte foot processes (Nicolazzo *et al.*, 2006a). The three-dimensional structure of the BBB is sketched in **Fig. 3.1a.** At the luminal surface of endothelium, there is a fluffy surface glycocalyx layer (SGL) (Ueno et al., 2004). This mucopolysaccharide structure is highly hydrated in electrolytic solutions and contains a large number of solid-bound negative charges(Lawrenson, 1997) because it is rich in proteoglycan, glycoproteins, and glycosaminoglycan aggregates (Tarbell and Pahakis, 2006). On the abluminal side, pericytes attach to the membrane of the endothelium at irregular intervals. The endothelial cells and pericytes are surrounded by a uniform and narrow matrix-like BM layer, which consists of collagen type IV, heparin sulfate proteoglycans, laminin, fibronectin, and other extracellular matrix proteins, and in turn, carries a great number of negative charges (Leblond and Inoue, 1989; Hamann *et al.*, 1995; Lawrenson, 1997; del Zoppo and Hallenbeck, 2000; Miosge, 2001). Finally, on the tissue side, the BM is ensheathed by astrocyte foot processes (AP), which covers more than 98% of the brain microvasculature surface (Cohen *et al.*, 1995; Pardridge, 1999; Nicolazzo *et al.*, 2006a). For small hydrophilic solutes, the major transport pathway across the BBB is the paracellular pathway consisting of the SGL, endothelial tight junction openings, the BM, and the openings between adjacent astrocyte foot processes (Hawkins and Davis, 2005) (**Fig. 3.2**).

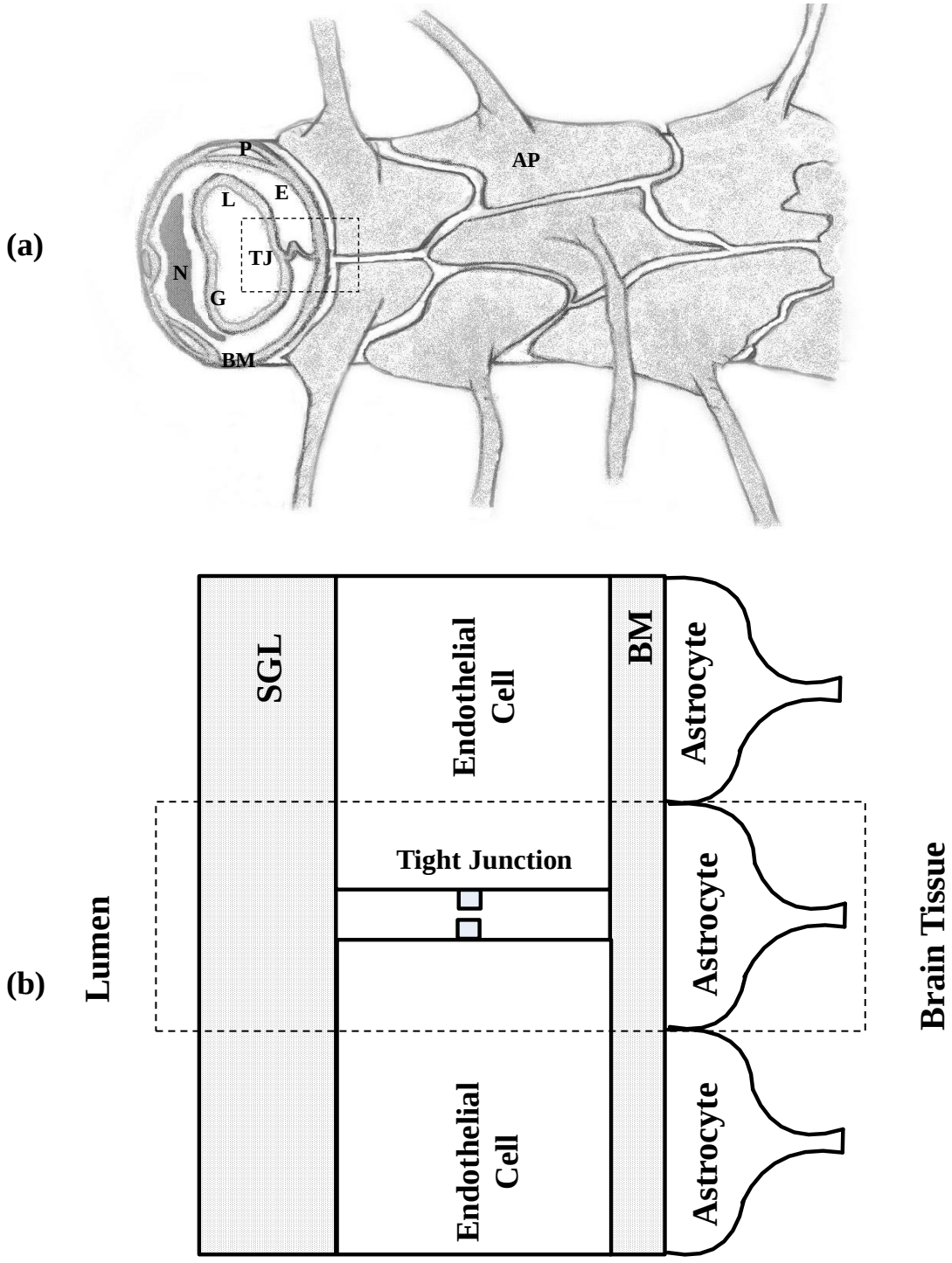

Fig. 3.1 Schematic of the BBB (not in scale). **(a)** Three-dimensional view of the BBB. Abbreviations: AP, astrocyte foot processes; BM, basement membrane; E, endothelium; L, lumen of microvessel; G, Glycocalyx layer; N, nuclease of endothelial cell; P, pericyte; TJ, tight junction. **(b)** 2-D cross-sectional view of the dash-lined region in **Fig. 3.1a**. The curvature of the microvessel wall is neglected since diameter of the microvessel is much larger than the width of the inter-endothelial cleft and the wall thickness. The paracellular

transport pathway from the blood lumen to the brain tissue includes: endothelial surface glycocalyx layer, inter-endothelial cleft, basement membrane, and the cleft between

The charge at the microvessel wall was first quantitatively measured *in vivo* on frog mesenteric microvessels (Adamson et al., 1988). They found that the permeability of mesenteric microvessels to positively charged ribonuclease (+4) was twice that to negatively charged α-lactalbumin (-10) although they have similar size. Based on these measured data, Fu et al. (Fu et al., 2003)developed an electro-diffusion model to explore the charge effect of the SGL of the mesenteric microvessel wall on its permeability. They found that in order to account for the 2-fold difference in the permeability to positively charged ribonuclease and that to negatively charged α-lactalbumin, the charge density of the SGL of frog mesenteric microvessels would be 25-35 mEq/L. Recently, Yuan et al. measured the permeability of intact rat mesenteric and pial microvessels to ribonuclease ($P^{\text{ribonuclease}}$) and α-lactalbumin ($P^{\alpha\text{-lactalbumin}}$) using a quantitative fluorescence imaging microscopy. For mesenteric microvessel, $P^{\text{ribonuclease}}$ was 2.05×10^{-6} cm/s, about 2-fold of $P^{\alpha\text{-lactalbumin}}$ (0.99×10^{-6} cm/s) while for pial microvessel, $P^{\text{ribonuclease}}$ was 5.47×10^{-7} cm/s, about 4-fold of $P^{\alpha\text{-lactalbumin}}$ (1.24×10^{-7} cm/s)(Yuan et al., 2009a). To investigate the effect of the charge carried by the BBB on the charged solute permeability observed by Yuan et al. (Yuan et al., 2009a), we developed an electro-diffusion model in this study.

Previously, several mathematical models have been developed to describe the charge effect on microvessel permeability. A simple Donnan-type model was first used to describe the electrostatic exclusions of the SGL to the charged solute (Deen et al., 1980; Adamson et al., 1988). Another electrochemical model was developed by (Stace and Damiano, 2001; Damiano and Stace, 2002), in which, the SGL was considered as a multi-

component mixture. However, these models only considered transport across the SGL. Later, Fu et al. (Fu et al., 2003)developed a two-dimensional model for charged transport across the inter-endothelial cleft of frog mesenteric microvessel, which incorporated the effect of both size and charge and provided the first quantitative analysis of various experimental results associated with negative charges in para-endothelial pathways.

Although the above model provided a good prediction for the permeability of charged molecules across mesenteric or other peripheral microvessels with endothelium only, it is not applicable to the transport across the BBB since the anatomical structure of the cerebral microvessel is very different from that of peripheral ones. **Figure 3.1b** shows the schematic of the BBB structure. We can see that in addition to endothelium that consists of the SGL, tight junctions in between adjacent endothelial cells, there are wrapping BM and astrocytes surrounding the BBB endothelium. Therefore, in this study, we developed a new transport model for the charge effect of the BBB by extending our previous model in Fu et al. (Fu et al., 2003) for endothelium alone to include the steric and charge effect of the BM and astrocyte foot processes on the BBB permeability to charged solutes.

3.2 Model Description

Figure 3.2 shows our model geometry for the BBB, which is an enlarged and detailed view of the dash-lined region in **Fig. 3.1b**. Description for the anatomical parameters was given in the figure caption for **Fig. 3.2**. The electric charge was assumed to exist both in the SGL and BM. According to Fu et al.(Fu et al., 2003), the overall solute permeability across the endothelium is independent of charge density profile in the SGL as long as they have the same total charge and maximum value. For simplicity, we

assumed that the charge densities C_m in both the SGL and the BM are constants: in SGL, $C_m = C_{m,f}$ ($-L_f - L - L_b < x < -L - L_b$); in BM, $C_m = C_{m,b}$ ($-L_b < x < L_b$). Similar assumptions made by Deen at al.(Deen et al., 1980) and Fu et al. ((Fu et al., 2003)) are used in the SGL and BM: (1) all charged solutes [ribonuclease, α-lactalbumin, and univalent cations and anions (mainly Na+ and Cl^-)] obey a modified Nernst-Planck flux expression; (2) overall electroneutrality is satisfied everywhere; (3) Donnan equilibria exist at the interfaces of the fiber layers (SGL and BM) and other regions of BBB.

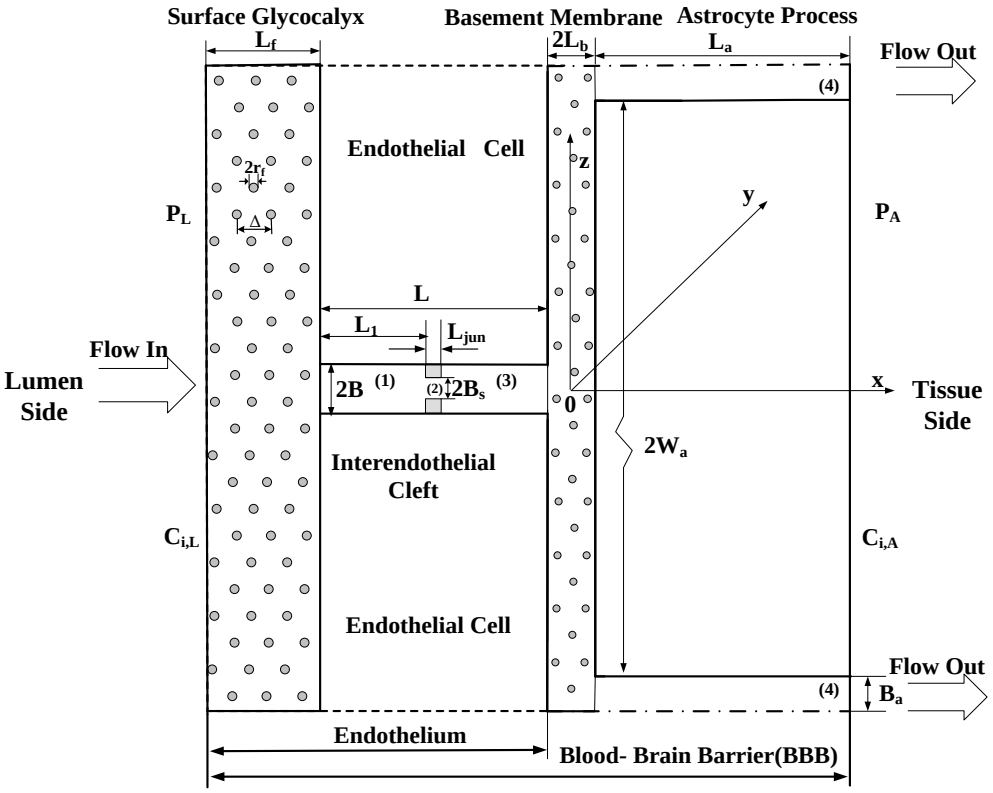

Fig. 3.2 Enlarged view of dash-lined region of **Fig. 3.1b** (not in scale). At the luminal side, there is a SGL represented by a periodic array of cylindrical fibers (Fu et al., 1994; Squire et al., 2001; Fu et al., 2003; Weinbaum et al., 2003; Fu and Shen, 2004). The radius of these fibers is r_f and the gap spacing between the fibers is Δ. The SGL has a thickness of L_f. Between two adjacent endothelial cells, there is an inter-endothelial cleft with a length of L and a width of 2*B*. In the inter-endothelial cleft, there is a L_{jun} thick tight junction strand with a continuous slit-like opening of width $2B_s$. The distance between the junction strand and luminal front of the cleft is L_1. At the tissue side of the cleft, a BM separates the endothelium and the astrocyte foot processes ensheathing the

brain blood vessels. The width of the basement membrane is $2L_b$ and the length of the astrocyte foot processes is $2W_a$. Between adjacent astrocyte foot processes, there is a cleft with length L_a and width $2B_a$. These anatomical structures were drawn based on electron microscopy studies (Schulze and Firth, 1992; Allt and Lawrenson, 1997; Cassella 1997; Farkas and Luiten, 2001). The charge density in the surface glycocalyx layer and basement membrane is $C_{m,f}$ and $C_{m,b}$, respectively.

The governing equations and the boundary conditions for the model are detailed in the **Appendix B**. The concentration profiles of solute i in all regions of the BBB were obtained by solving the governing equations with corresponding boundary conditions. The flow rate of test solute Q_L^S through a period of the cerebral microvessel with a length of L_v, was obtained by integrating $D_{i,1}\frac{\partial C_{i,1}}{\partial x}$ at $x = -L - L_b$ across the cross-sectional area of the cleft. The diffusive permeability P is defined as

$$P = \frac{Q_L^S}{C_{i,L} - C_{i,A}} \frac{L_{jt}}{L_v} \tag{3.1}$$

where L_{jt} is the total length of the cleft per unit surface area of the microvessel wall.

If there is only a continuous slit and no large pores in the tight junction, which is the case for the cerebral microvessel (Allt and Lawrenson, 1997) , because the inter-endothelial and inter-astrocyte clefts, and the BM are narrow compared to their lengths, a 1-D approximation can be made in these regions and **Eq. 3.1** becomes,

$$P = \frac{1}{R_f + R_b + R_1 + R_2 + R_3 + R_4} \frac{L_{jt}}{L_v} \tag{3.2}$$

where R_n (n= f,b,1,2,3,4) are the resistances of the SGL, the BM and each cleft region of the BBB to the charged solute transport: $R_f = L_f e^{Z^i \psi_f}/(2D_{i,f}B)$, $R_b = (W_a + B_a)e^{Z^i \psi_b}/(4D_{i,b}L_b)$, $R_1 = L_1 e^{Z^i \psi_1}/(2D_{i,1}B)$, $R_2 = L_{jun} e^{Z^i \psi_2}/(2D_{i,2}B_s)$, $R_3 = (L - L_1 - L_{jun})e^{Z^i \psi_3}/(2D_{i,3}B)$, $R_4 = L_a e^{Z^i \psi_4}/(2B_a D_{i,4})$. Here ψ_n (n= f,b,1,2,3,4) are the electrical potentials in the corresponding region of the BBB. From the electrical potential profile obtained from

Appendix B, ψ_n (n=1,2,3,4) $<10^{-6}$ and thus $Z^i\psi_n < 10^{-5}$ for both ribonuclease ($Z^i = +4$) and α-lactalbumin ($Z^i = -10$). As a result, $e^{Z^i\psi_n}$ are very close to 1 for n=1,2,3,4 so that the resistances in these four regions could be simplified to $R_1 = L_1/(2D_{i,1}B)$, $R_2 = L_{jun}/(2D_{i,2}B_s)$, $R_3 = (L - L_1 - L_{jun})/(2D_{i,3}B)$, $R_4 = L_a/(2B_aD_{i,4})$.

3.3 Model Parameters

The transport parameters for the BBB under normal conditions are listed in Table 3.1. The mammalian Ringer solution with 10mg/ml bovine serum albumin (BSA) was used in the *in vivo* experiments, in which the concentration of charged BSA, 0.15 mM, is much smaller compared to ion concentrations (Fu et al., 2003). Thus the cation concentration is roughly the same as that of anions in the lumen: C_+=C_-=140 mM. To satisfy the electrical neutrality, C_+ should be identical to C_- in all the cleft regions without charge, whose values are dependent on C_+ and C_- in the lumen as well as the charge density in the SGL and BM. These values are calculated using equations in **Appendix B**.

Because most of the cations are Na^+ and most of the anions are Cl^-, we used the diffusion coefficients of Na^+ and Cl^- as those for cations and anions, respectively, D_+ = 1.593×10^{-5}cm^2/s and D_- = 2.115×10^{-5}cm^2/s at 37^{o}C (Deen et al., 1980).

Table 3.1 Transport parameters for charged solutes

Water Transport	Darcy permeability of surface glycocalyx (Guo *et al.*, 2000; Weinbaum *et al.*, 2003)	K_p	3.16 nm^2
	Viscosity (Zhang *et al.*, 2006a)	μ	7.0×10^{-4} kg/m/s
Ribonuclease and α-lactalbumin (r_s=2.0nm)	Free diffusion coefficient in aqueous solution at 37°C(Fu *et al.*, 2003)	D_i^{free}	1.13×10^{-6} cm^2/s
	Effective diffusion coefficient in the fiber layer(Ogston *et al.*, 1973; Michel and Curry, 1999; Fu *et al.*, 2003; Sugihara-Seki and Fu, 2005)	$D_{i,f}$	1.01×10^{-7} cm^2/s
	Effective diffusion coefficient in the inter-endothelial cleft(Michel and Curry, 1999; Fu *et al.*, 2003; Sugihara-Seki and Fu, 2005)	$D_{i,n}$ (n=1,3) (B=9)	6.86×10^{-7} cm^2/s
	Effective diffusion coefficient in the small slit of the junction strand(Michel and Curry, 1999; Fu *et al.*, 2003; Sugihara-Seki and Fu, 2005)	$D_{i,2}$ (B_s=2.25)	5.29×10^{-8} cm^2/s
	Effective diffusion coefficient in the basement membrane(Michel and Curry, 1999; Fu *et al.*, 2003; Sugihara-Seki and Fu, 2005)	$D_{i,b}$ (L_b=12.5)	7.10×10^{-8} cm^2/s
	Effective diffusion coefficient in the cleft between astrocyte feet(Ogston *et al.*, 1973; Michel and Curry, 1999; Fu *et al.*, 2003; Sugihara-Seki and Fu, 2005)	$D_{i,4}$ (B_a=15)	8.49×10^{-7} cm^2/s

3.4 Results

Electrical Potential Profiles

Figure 3.3 shows the electrical potential profiles E_f and E_b across the SGL (Fig. 3.3a) and across the BM (Fig. 3.3b). The electrical potential is determined by the distribution of cations C_+ and anions C_- and the charge density C_{mf} and C_{mb} in the SGL and BM. Since the mammalian Ringer solution is used as the perfusate and the cation and anion concentrations are constants (C_+=C_-=140mM), so the only factor that affects the

electrical potential is the charge density. For a constant charge density C_{mf} or C_{mb}, E_f or E_b is almost uniform across the SGL or the BM, until a step change at the interface between the charged and non-charged regions due to unequal C_+ or C_- distribution in the charged and non-charged regions (Eqs. B5, B43). As shown in Fig. 3. 3, when C_{mf} or C_{mb} increases, E_f or E_b becomes more negative and the electrical partition at the entrance of the charged (SGL and BM) regions becomes larger, which favors the transport of positively charged solutes. In contrast, this electrical partition at the exit of the charged regions favors the transport of negatively charged solutes.

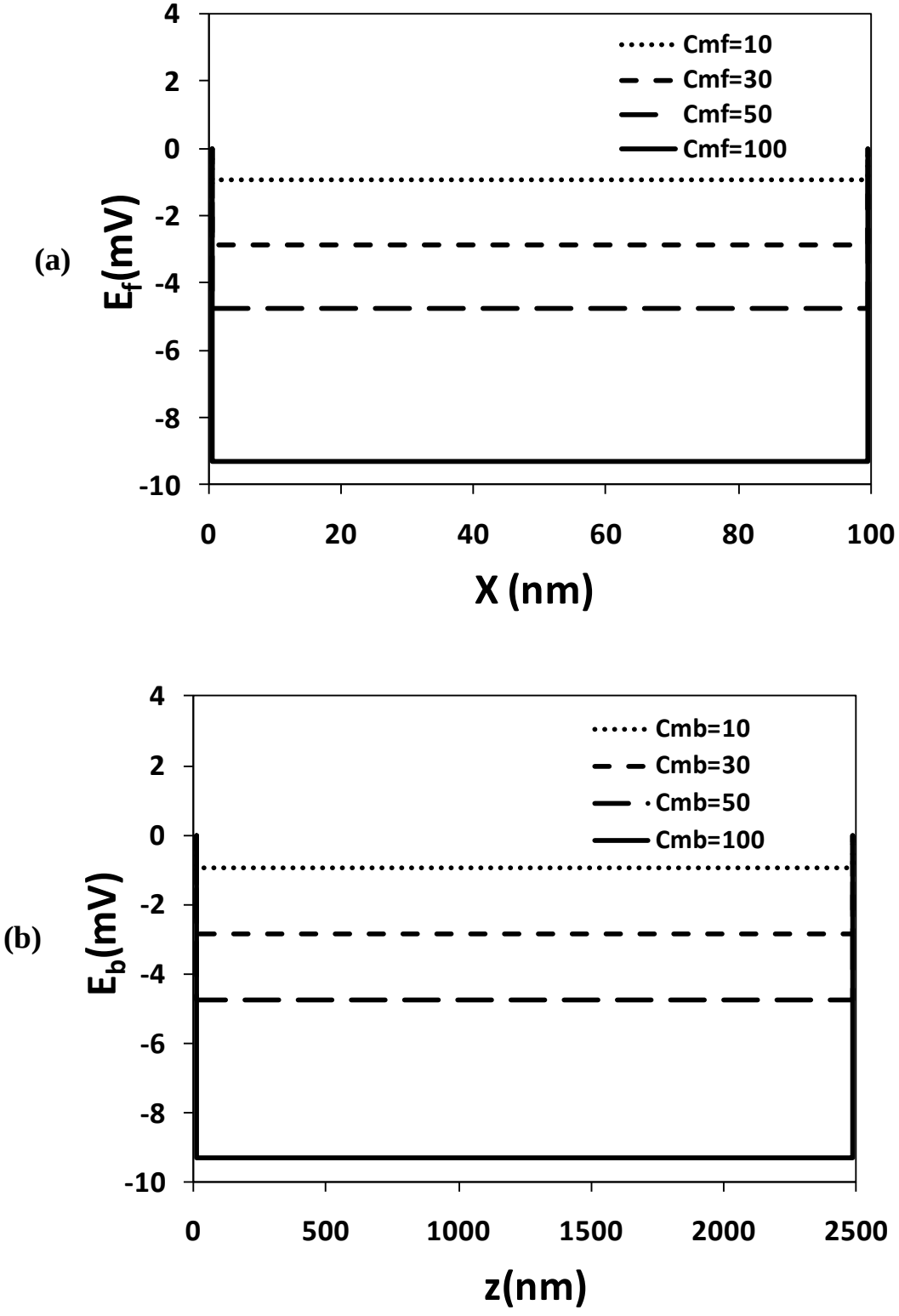

Fig. 3.3 Profiles of electrical potential E_f in the SGL **(a)** and E_b in the BM **(b)** for four different charge densities $C_{m,f}$ or $C_{m,b}$ = 10 (dotted line), 30 (short-dashed line), 50 (long-dashed line), and 100mEq/l (solid line). The reference potential of E_f = 0 is

at x=-L-L_b-L_f, that of E_b = 0 is at z = 0, x= -L_b.

Concentration Distributions of Solutes

Figure 3.4 shows the concentration distributions of positively charged ribonuclease (Z^i =+4), negatively charged α-lactalbumin (Z^i=-10), and a same sized neutral solute (Z^i =0). Due to the electrical partition at the SGL (and BM) entrance as shown in Fig. 3.3, the concentration of positively charged ribonuclease has a step increase at the SGL (or BM) entrance, by about 1.53-fold, while the concentration of negatively charged α-lactalbumin has a step decrease, by about 2.91-fold if both C_{mf} and C_{mb} are 30 mEq/L. For a neutral solute, its concentration is not affected by the charge in the fiber layers. In the SGL, the concentration of a neutral solute decreases from 1 in the lumen to 0.94 at the exit of the SGL, while in the BM it decreases from 0.83 at the entrance to 0.044 at the exit. These decreases are due to the size effect such as the diffusion resistance and steric hindrance of the fibers to the solutes. For the positively charged ribonuclease, its concentration abruptly increases by electrical partition at the entrance of the SGL (and BM), gradually decreases in the fiber layer due to the size effect, and then abruptly decreases further at the exits due to the electrical partition. For negatively charged α-lactalbumin, the electrical partition at the interfaces gives an opposite effect to that for ribonuclease.

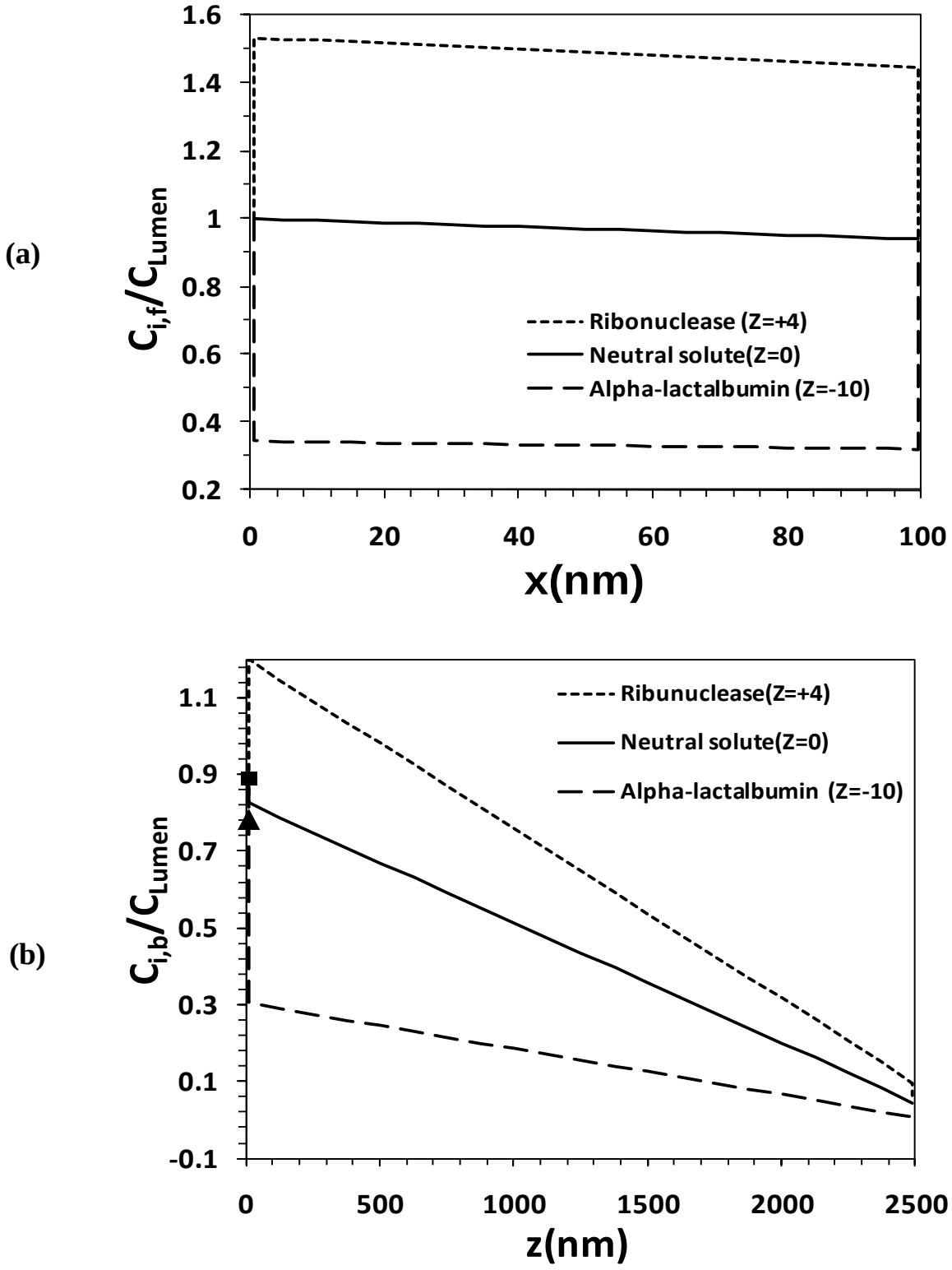

Fig. 3.4 Dimensionless concentration distribution $C_{i,f}/C_{Lumen}$ in the SGL **(a)** and $C_{i,b}/C_{Lumen}$ in the BM **(b)** for a positively charged molecule, ribonuclease (charge number +3, dotted line), a neutral solute (solid line), and a negatively charged molecule, α-

lactalbumin (charge number -11, dashed line). Here $C_{m,f}$=$C_{m,b}$=30mEq/l. Square and triangle in Fig. 3.4b indicate the concentrations of α-lactalbumin and ribonuclease, respectively, at the exit of the inter-endothelial cleft (or the entrance to the BM).

Charge Effect of the SGL and BM on Permeability of Charged Solutes

Figure 3.5 shows the ratio of permeability of positively charged ribonuclease to that of negatively charged α-lactalbumin *(P_{rib}/P_{alpha})* as a function of charge density in the SGL, C_{mf}, for rat mesenteric microvessels consisting of the endothelium only (SGL and endothelial cells) (**Fig. 3.5a**), and P_{rib}/P_{alpha} (**Fig. 3.5b**) as a function of charge density in the BM (C_{mb}) for rat pial microvessels (the BBB at the surface of the rat brain) consisting of the endothelium, the BM and the astrocyte foot processes (the BBB). In rat mesenteric microvessels or other peripheral microvessels, there are no tightly wrapping BM and the astrocyte foot processes. The charge effect on the charged solute transport comes only from the SGL of the endothelium. The filled squares in **Figs. 3.5a, b** are measured data in *in vivo* experiments on rat mesenteric and pial microvessels (Yuan et al., 2009a). The solid line in **Fig. 3.5a** is the model prediction for P_{rib}/P_{alpha} as a function of C_{mf} in the SGL of the mesenteric microvessel. We can see that, when C_{mf} increases, the ratio P_{rib}/P_{alpha} also increases. The best fit for the *in vivo* experimental data is at C_{mf} ~30 mEq/L. In **Fig. 3.5b**, the rat pial microvessel, which not only includes endothelium but also the BM and astrocytes, is considered. In this case, there are two charged regions: the SGL and the BM, which can contribute to the charged solute transport. Since there is no available information about the charge density in the BM, two assumptions are considered for the BM: 1) C_{mf} in the SGL of the BBB is the same as that in the SGL of mesenteric microvessels, i.e., C_{mf} = 30 mEq/L, as predicted from **Fig. 3.5a** (dashed line); and 2) C_{mf} = C_{mb} (solid line). From **Fig. 3.5b**, we can see that when C_{mb} increases, the

ratio P_{rib}/P_{alpha} also increases. To get a best fit for the experimental data for P_{rib}/P_{alpha}(Yuan et al., 2009a), C_{mf} and C_{mb} would be ~30 mEq/l for both cases.

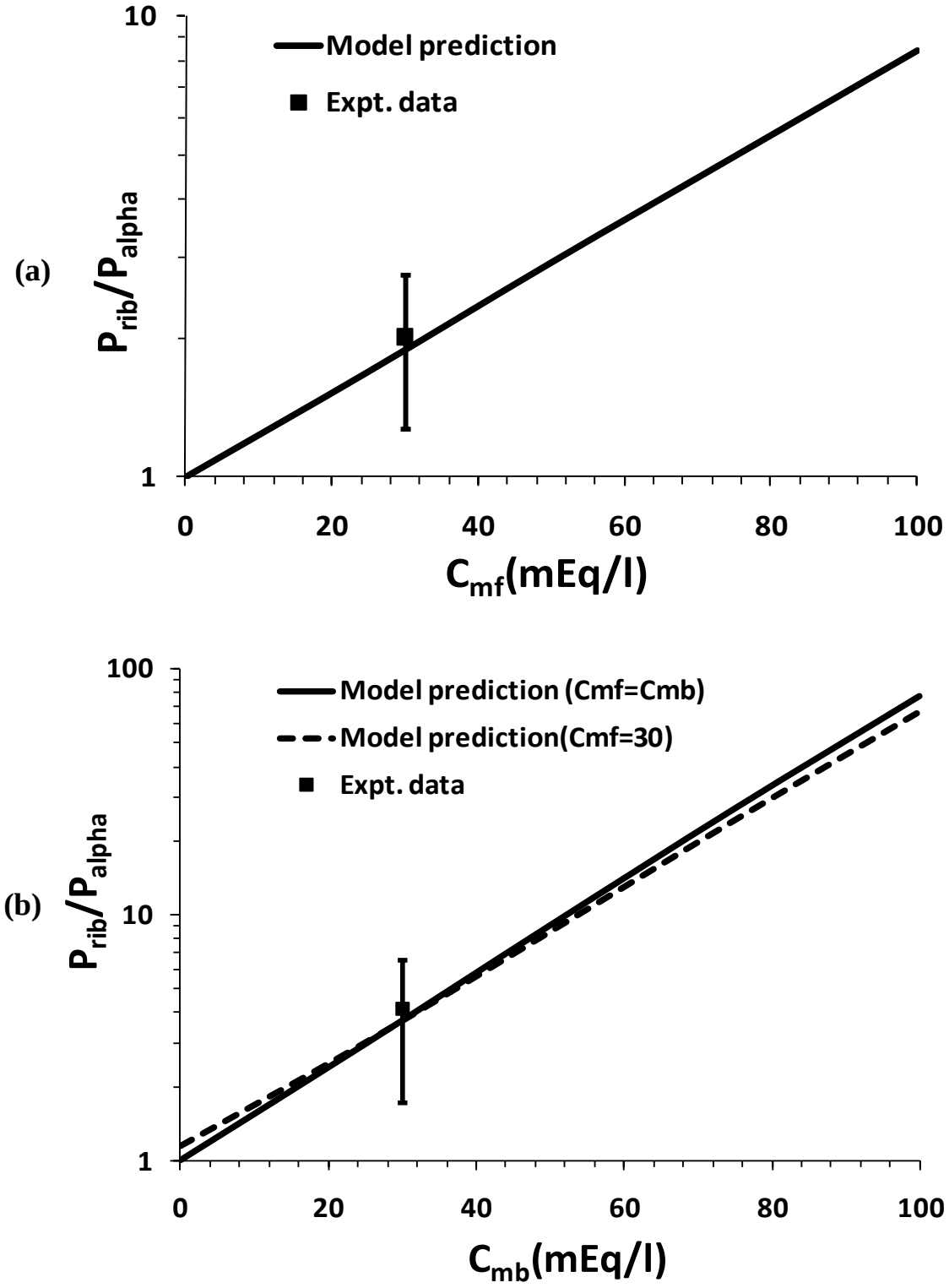

Fig. 3.5 (a) Ratio of permeability of rat mesenteric microvessels to positively charged ribonuclease to that of negatively charged α-lactalbumin *(P_{rib}/P_{alpha})* as a function of charge density in the SGL $C_{m,f.}$. The line is the model prediction while the square symbol

is *in vivo* experimental data(Yuan et al., 2010b). **(b)** Ratio of permeability of rat pial microvessels to positively charged ribonuclease to that of negatively charged α-lactalbumin *(P_{rib}/P_{alpha})* as a function of charge density in the BM $C_{m,b}$, under two cases: (1) $C_{m,f}$ = 30mEq/l (solid line) and (2) $C_{m,f} = C_{m,b}$ (dashed line).Here L_f = 100 nm for all cases.

Combined Effects of Charge Density C_{mf} , C_{mb} and Thickness L_f of the SGL

The ratios of microvessel permeability to ribonuclease and α -lactalbumin to that to the same-sized neutral solute (P/P_{neutral}) as a function of L_f are shown in **Figs. 3.6a,b**, when $C_{mf} = C_{mb} = 0$ (solid line), 25 (dashed line), 50 (short dashed line), and 100 mEq/L (dash-dot-dash line). From **Figs. 3.6a,b**, both $P_{ribonuclease}$ and $P_{\alpha\text{-}lactalbumin}$ decrease with increasing L_f due to size restriction in the SGL. When L_f is increased from 100 to 400nm, the reduction in $P_{ribonuclease}$ is 11-15%, that in $P_{\alpha\text{-}lactalbumin}$ is 16-18% no matter how much C_{mf} and C_{mb} are. However, due to the overall electrical partition at the entrance and exit of the SGL and BM with the fixed negative charge, which favors the transport of positively charged solutes, the increasing C_{mf} and C_{mb} enhances $P_{ribonuclease}$ but reduces $P_{\alpha\text{-}lactalbumin}$. Since the charge on α-lactalbumin (Z^i =-10) is higher than that on ribonuclease (Z^i =+4), the charge in the SGL and BM affects $P_{\alpha\text{-}lactalbumin}$ more significantly. When L_f =100 nm, $C_{mf} = C_{mb}$ from 0 to 50 mEq/L would increase $P_{ribonuclease}$ by 75%, while decrease $P_{\alpha\text{-}lactalbumin}$ by 81%.

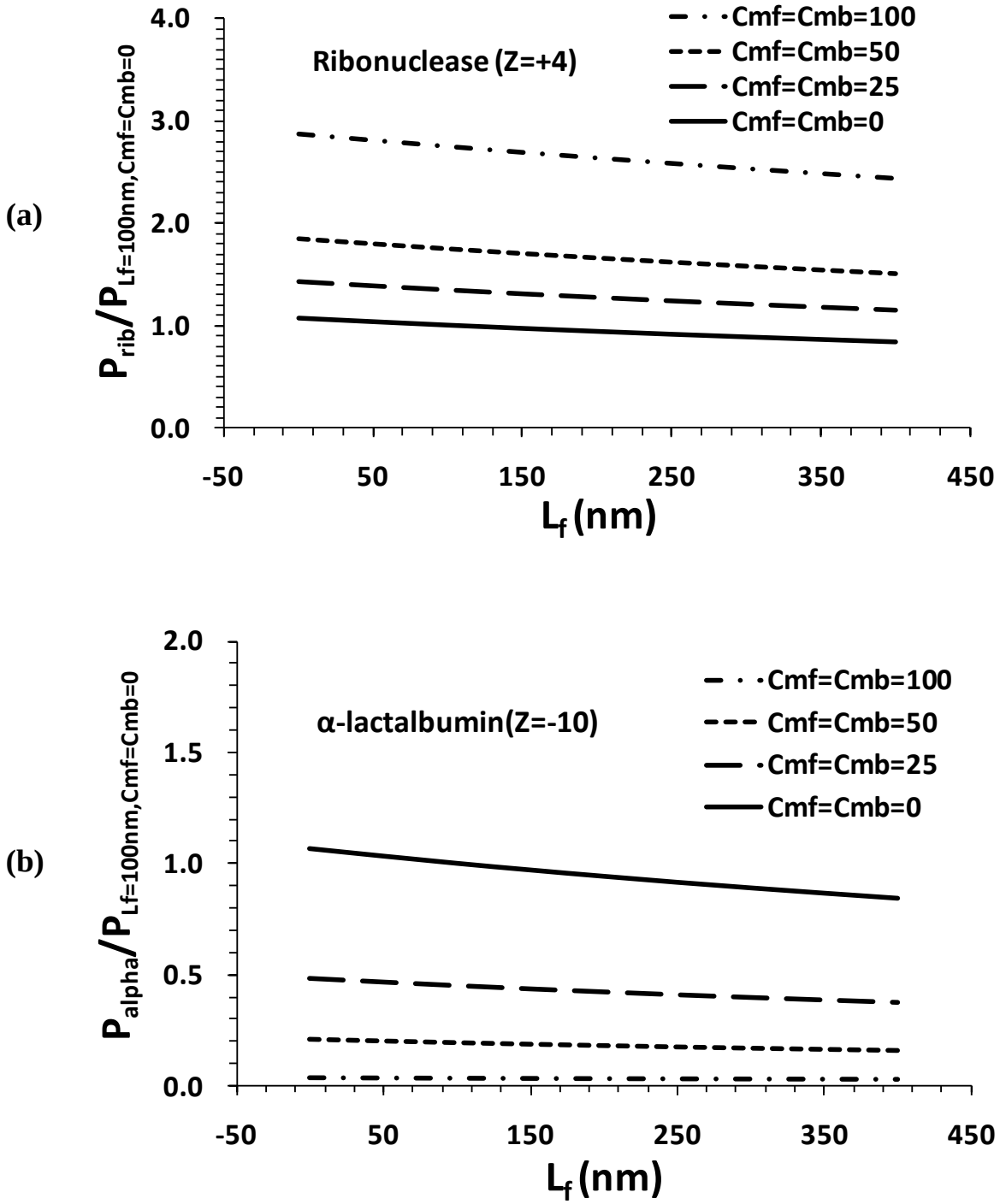

Fig. 3.6 Dimensionless permeability of ribonuclease **(a)** and α-lactalbumin **(b)** ($P/P_{Lf=100nm,Cm,f=Cm,b=0}$) as a function of the SGL thickness L_f under various charge density $C_{m,f}$ and $C_{m,b}$ ($C_{m,f} = C_{m,b}$): 0 (solid line), 25 (dashed line), 50 (short-dashed line), 100mEq/l (dash-dot-dash line).

Combined Effects of Charge Density C_{mf} , C_{mb} and Thickness L_b of the BM

Figures 3.7a,b demonstrate the ratios of microvessel permeability to ribonuclease and α-lactalbumin to that to the same-sized neutral solute (P/P_{neutral}) as a function of L_b of the BM, when $C_{mf} = C_{mb} = 0$ (solid line), 25 (dashed line), 50 (short dashed line), and 100 mEq/L (dash-dot-dash line). Both $P_{ribonuclease}$ and $P_{\alpha\text{-}lactalbumin}$ increase with increasing L_b. When L_b increases from 10 to 50 nm, the increase in $P_{ribonuclease}$ is 3.5, 3.1, 2.8 and 2.1 folds, and that in $P_{\alpha\text{-}lactalbumin}$ is 3.5, 4.4, 4.9 and 5.3 folds, when $C_{mf} = C_{mb} = 0$, 25, 50, 100 mEq/L. Increasing the thickness L_b of the BM greatly enhances the transport of all solutes, with the more enhancement for the negatively charged solutes. When $2L_b$ =20 nm, C_{mf} = C_{mb} from 0 to 50 mEq/L would increase $P_{ribonuclease}$ by 81%, while decrease $P_{\alpha\text{-}lactalbumin}$ by 81%.

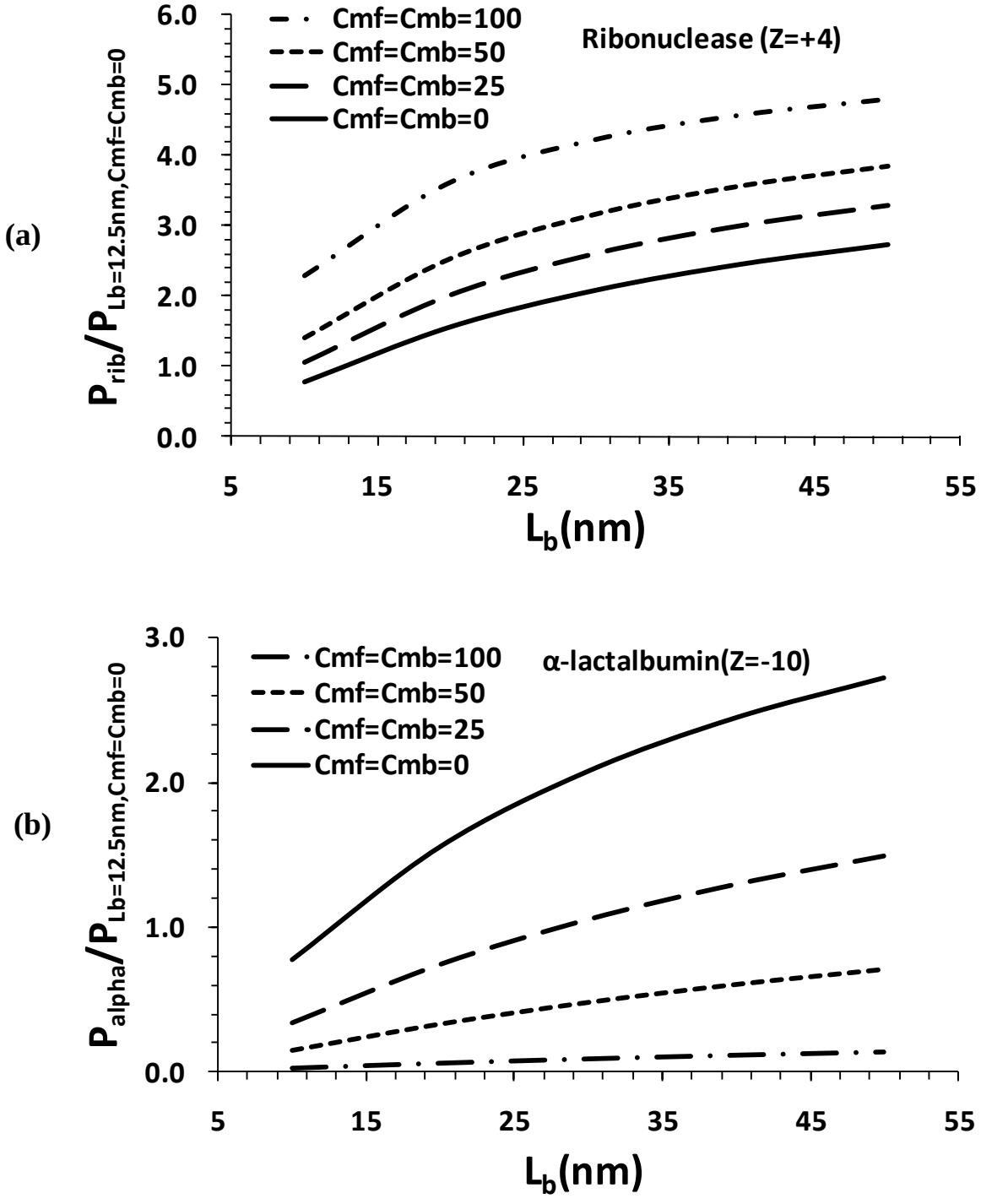

Fig. 3.7 Dimensionless permeability of **(a)** ribonuclease and **(b)** α-lactalbumin ($P/P_{Lb=12.5nm,Cm,f=Cm,b=0}$) as a function of the BM thickness L_b under various charge density $C_{m,f}$ and $C_{m,b}$ ($C_{m,f} = C_{m,b}$): 0 (solid line), 25 (dashed line), 50 (short-dashed line), 100mEq/l (dash-dot-dash line).

Sensitivity analysis

Sensitivity analysis is performed for anatomical parameters and the normalized permeability of ribonuclease and a-lactalbumin is listed in Table 3.2. The permeability is normalized compared with the control case (B=9nm, L=700nm, L_1=350nm, L_{jun}=11nm, L_a=1000nm, W_a=2500nm, D_v=10000nm). From Table 3.2 we can see that when the anatomical parameters (B, L, L_1, and L_{jun}) increases or decreases by 10% compared with normal case, the change of corresponding permeability is within 1.5%. For L_1, the corresponding permeability change is less than 0.01%. This result indicates that normalized permeability of the BBB to ribonuclease and a-lactalbumin are not very sensitive to the changes in B, L, L_1, and L_{jun}. However, when W_a and D_v increases or decreases by 10%, the corresponding permeability change is 8-11%. This results indicates that these two parameters have significant effect on the permeability.

Table **3.2** Sensitivity analysis of anatomical parameters for normalized P

Parameters	**Control Values (nm)**	**ribonuclease(Z=+4)**		**α-lactalbumin (Z=-10)**	
		-10%	**+10%**	**-10%**	**+10%**
B	9	101.73%	97.82%	100.95%	98.82%
L	700	99.12%	100.90%	99.76%	100.24%
L_1	350	100.00%	100.00%	100.00%	100.00%
L_{jun}	11	99.29%	100.72%	99.81%	100.19%
L_a	1000	99.39%	100.62%	99.83%	100.17%
W_a	2500	93.27%	107.78%	91.98%	109.55%
D_v	10000	90.91%	111.11%	90.91%	111.11%

Resistances from different regions of the BBB

To investigate the contribution of different regions of the BBB to charged solute transport, the ratio between resistance from each region of the BBB and the total resistance was calculated and listed in Table 3.3. From Table 3.3 we can see that, basement membrane is the major contributor for resistance for both ribonuclease(72.16%) and α-lactalbumin(87.17%).

Table **3.3** The ratio of resistance from each region of the BBB and the total resistance for ribonuclease and α-lactalbumin

Percentage Resistance (R_n/Rt)	SGL	Inter-endothelial cleft (region 1)	Inter-endothelial cleft (region 2)	Inter-endothelial cleft (region 3)	BM	Cleft between astrocyte processes
Ribonuclease	5.65%	4.45%	7.26%	4.31%	72.16%	6.17%
a-lactalbumin	6.83%	1.20%	1.96%	1.17%	87.17%	1.67%

3.5 Discussion

In order to determine the charge density of the SGL (C_{mf}) and that of the BM (C_{mb}) in the BBB, we developed an electro-diffusion model based on the ultra-structural parameters from the literature (Table 3.1). Combining model predictions with the measured permeability data $P_{ribonuclease}$ and $P_{\alpha\text{-}lactalbumin}$ from rat mesenteric and pial microvessels (Yuan et al., 2009a; Yuan et al., 2009b), we found the best fit is when both C_{mf} and C_{mb} are ~ 30mEq/L. This value is the same as that predicted for C_{mf} in frog mesenteric microvessels (Fu et al., 2003). Our results suggest that the fiber matrix

structure and the charge carrying ability in the SGL and the BM are similar, implying that the SGL and the BM of the BBB may have similar molecular compositions.

Fu et al. (Fu et al., 2003) showed that in addition to the tight junctions in the inter-endothelial cleft, the negative charge carried by the SGL of endothelium in the mesenteric (or other peripheral) microvessel affects the charged solute transport across the microvessel wall. Our current model further indicates that the charge carried by the BM of the BBB, is another, probably more important determinant of the BBB permeability due to its long narrow geometry (thickness $2L_b$ = 20-30nm, length $2W_a$ = 5000nm). **Figure 3.4b** shows the large concentration drop across the BM. In disease, the BM would be widened [12]. When its thickness $2L_b$ increases from 20 to 100 nm, $P_{\alpha\text{-}lactalbumin}$ would increase up to 5.3-fold. However, at $2L_b$ = 100 nm, the charge density of 100mEq/l in the SGL and BM would reduce $P_{\alpha\text{-}lactalbumin}$ by 97% compared to that without charge. Therefore, the charge of the BBB plays a crucial role in maintaining the low permeability of the BBB.

From **Eq. 3.2**, we obtained the expression for the relative concentration drop of solute i, $\Delta C_{i,n}$, in each region of the BBB,

$$\frac{\Delta C_{i,n}}{(C_{i,L}-C_{i,A})} = \frac{R^n}{R_f+R_b+R_1+R_2+R_3+R_4} \qquad \text{(n = f, b,1,2,3,4)} \qquad (3.3)$$

Under normal case when L_f =100nm, $2L_b$ = 25 nm, C_{mf} = C_{mb} = 30mEq/L, the concentration drops are 5.8%, 6.1%, and 6.9% in the SGL, 14.7%, 11.3% and 3.9% in the inter-endothelial cleft including the tight junction, 73.8%, 78.2%, and 87.7% in the BM, 5.7%, 4.4% and 1.5% in the inter-astrocyte cleft, for ribonuclease, a neutral solute and α-lactalbumin, correspondingly. We can see that more than 70% of the drop is in the BM for all the solutes, with negatively charged α-lactalbumin drops the most, by 87.7%. Because

of this largest drop in the BM for α-lactalbumin, the relative drop in the inter-endothelial cleft is the smallest, only 3.9%, compared to 14.7% for ribonuclease and 11.3% for a neutral solute. Due to this smallest drop, the concentration of α-lactalbumin is the highest at the exit of the inter-endothelial cleft (square in **Fig. 3.4b**). Thus, we have a region in the cleft with higher concentration of α-lactalbumin than ribonuclease and a neutral solute although the concentration of α-lactalbumin is always lower in the SGL and BM (Fig.3.4). This result suggests if we want to deliver drugs for targeting junction proteins in the cleft, we would use a negatively charged drug or drug carrier.

In addition to designing various charged molecules, we can also modulate the charge in the SGL and the BM by matrix binding proteins such as orosomucoid. Orosomucoid, a highly anionic glycoprotein, has been found to modulate microvessel permeability by adding the negative charge to the vessel wall(Haraldsson and Rippe, 1987; Curry *et al.*, 1989; Haraldsson *et al.*, 1992; Yuan *et al.*, 2009a; Yuan *et al.*, 2009b). As discussed earlier, the increased negative charge of the BBB would greatly decrease the permeability of negatively charged solutes while increase that of positively charged ones.

In summary, we developed an electro-diffusion model for the BBB transport, which can be used to elucidate the charge selectivity of the SGL and BM in modulating the permeability of the BBB and to provide a new method for controlling drug delivery to the CNS.

CHAPTER 4 PERMEABILITY OF ENDOTHELIAL AND ASTROCYTE COCULCTURES: IN VITRO BLOOD-BRAIN MODELS FOR DRUG DELIVERY STUDIES

4.1 Introduction

To investigate the mechanisms by which the BBB maintains and regulates its permeability in health and disease, various *in vivo* and *in vitro* models have been used to study transport across the BBB. *In vitro* BBB models have been widely used due to their low cost, repeatability, and feasibility in performing high-throughput screening and investigating regulatory mechanisms at the molecular level, despite losing some expression of the BBB efflux protein systems and having a comparatively higher permeability compared to *in vivo* models (Nicolazzo *et al.*, 2006b). The cells for these *in vitro* models are obtained either from primary/sub-passaged or immortalized cell cultures. Primary brain capillary endothelial cells have the closest resemblance to the BBB phenotype *in vivo*, and exhibit excellent characteristics of the BBB at early passages (Nicolazzo *et al.*, 2006b). They, however, have inherent disadvantages such as being extremely time consuming and costly to generate, being easily contaminated by other neurovascular unit cells, losing their BBB characteristics over passages, and requiring high technical skills for extraction from brain tissue (Deli et al., 2005; Brown et al., 2007). An immortalized mouse brain endothelial cell line, bEnd3, has recently been under investigation for *in vitro* BBB models because of its numerous advantages over primary cell culture: the ability to maintain BBB characteristics over many passages, easy growth and low cost, formation of functional barriers and amenability to numerous molecular

interventions (Soga *et al.*, 2001; Yoder, 2002; Brown *et al.*, 2007; Tyagi *et al.*, 2009; Yuan *et al.*, 2010a). Previous RT-PCR analysis showed that bEnd3 cells express the tight junction proteins ZO-1, ZO-2, occludin and claudin-5, and junctional adhesion molecules (Omidi et al., 2003; Brown et al., 2007). They also maintained functionality of the sodium- and insulin- dependent stereospecific facilitative transporter GLUT-1 and the P-glycoprotein efflux mechanism (Omidi et al., 2003), formed fairly tight barriers to radiolabeled sucrose, and responded like primary cultures to disrupting stimuli(Brown et al., 2007).

To characterize the transport properties of *in vitro* BBB models, Malina et al. (Malina et al., 2009) and others (Bowman et al., 1983; Thompson et al., 1994; Salvetti et al., 2002; Karyekar et al., 2003; Hamm et al., 2004; Kemper et al., 2004; Boveri et al., 2005; Kraus et al., 2008; Poller et al., 2008) measured the diffusive permeability of endothelial cell monolayer and coculture of endothelial cells with astrocyctes to fluorescence or isotope labeled tracers, e.g., sucrose, inulin, and mannitol. Sahagun et al.(Sahagun et al., 1990) reported the ratio between abluminal concentration and luminal concentration of different-sized dextrans (4k, l0k, 20k, 40k, 70k, and 150k) across mouse brain endothelial cells. Gaillard and de Boer (Gaillard and de Boer, 2000) measured the permeability of sodium fluorescein and FITC-labeled Dextran 4k across a coculture of calf brain capillary endothelial cells with rat astrocytes. Many investigators have measured the transendothelial electrical resistance (TER) of brain endothelial monolayers and cocultures as an indicator of ion permeability (deVries et al., 1996; Cucullo et al., 2002; Santaguida et al., 2006; Zhang et al., 2006b).

To search for an effective, relatively convenient, and inexpensive *in vitro* BBB

model, we characterized the junction protein expression and quantified the TER and permeability to water and solutes of four *in vitro* BBB models: bEnd3 monoculture, bEnd3 coculture with astrocytes, coculture with two BM substitutes: collagen type I and IV mixture, and Matrigel. Collagen type IV network is the basic framework of native BM(Engvall, 1995; Miosge, 2001) and Matrigel is a soluble and sterile extract of BM derived from the EHS tumor, which has been widely used as a reconstituted BM in studying cell morphogenesis, differentiation and growth(Kleinman and Martin, 2005). As negative controls, we also characterized the transport properties of astrocyte monoculture and astrocyte monoculture with Matrigel coating,

4.2 Materials and methods

Cell culture

Immortalized mouse endothelial cells, bEnd3, from American Type Culture Collection (Manassas, VA) were cultured in Dulbecco's modified Eagle's medium (DMEM) (Sigma, St. Louis, MO) with 10% fetal bovine serum (FBS) (Hyclone, Logan, UT), 3mM L-glutamine (Sigma, St. Louis, MO) and 1% penicillin–streptomycin (PS) (Sigma, St. Louis, MO). Cells (passage 15-30) were maintained in a humidified cell culture incubator at 37 ℃ and with 5% CO2/95% air.

The astrocytes were obtained from the cortices of 8-10 day old Sprague-Dawley rat pups. All procedures involving animals were approved by the Columbia University IACUC. Briefly, the brain was removed and placed into a Petri dish containing a few drops of salt solution. The cortex was separated, minced, and digested in papain (Sigma, St. Louis, MO) for 30 min at 32 ℃. The digested tissue was triturated and transferred to a T75 flask containing Neurobasal-A medium with 5% B27 supplement (Invitrogen,

Carlsbad, CA), 1mM glutamine and 5mg/ml D-glucose (Sigma, St. Louis, MO). After an hour, the flasks were vigorously shaken and the media was discarded. The remaining astrocytes were grown in DMEM with 10% fetal bovine serum, 1mM glutamine, and 1% PS for 2 weeks. The media in the flask was replaced every two days.

For astrocyte and bEnd3 monocultures, the Transwell filters (0.4-μm pore size, 12-well; Corning, Lowell, MA) were coated with fibronectin (30 μg/ml). Astrocytes were seeded onto the abluminal side of the filter at a density of 2.75×10^4 cells per filter and grown for 5-6 days. The bEnd3 cells were seeded onto the luminal side of the filter at a density of 6.6×104 cells per filter and grown for 3-4 days.

The procedure for coculturing bEnd3 cells and astrocytes is shown in **Fig. 4.1**. The Transwell filter was first coated with fibronectin or basement membrane substitutes (collagen type I and IV mixture or Matrigel) as described below. The Transwell filter was then inverted and astrocytes were seeded onto the abluminal side of the filter at a density of 2.75×104 cells per filter and allowed to adhere for 2 hours. After that, the filter was flipped back and astrocytes were cultured in DMEM with 10%FBS and 1%PS for 2 days. At the end of 2 days, bEnd3 cells were seeded on the luminal side of the filter at a density of 6.6×10^4 cells per filter and cocultured with astrocytes for an additional 3-4 days. The medium from both luminal and abluminal sides of the Transwell filter was changed every other day.

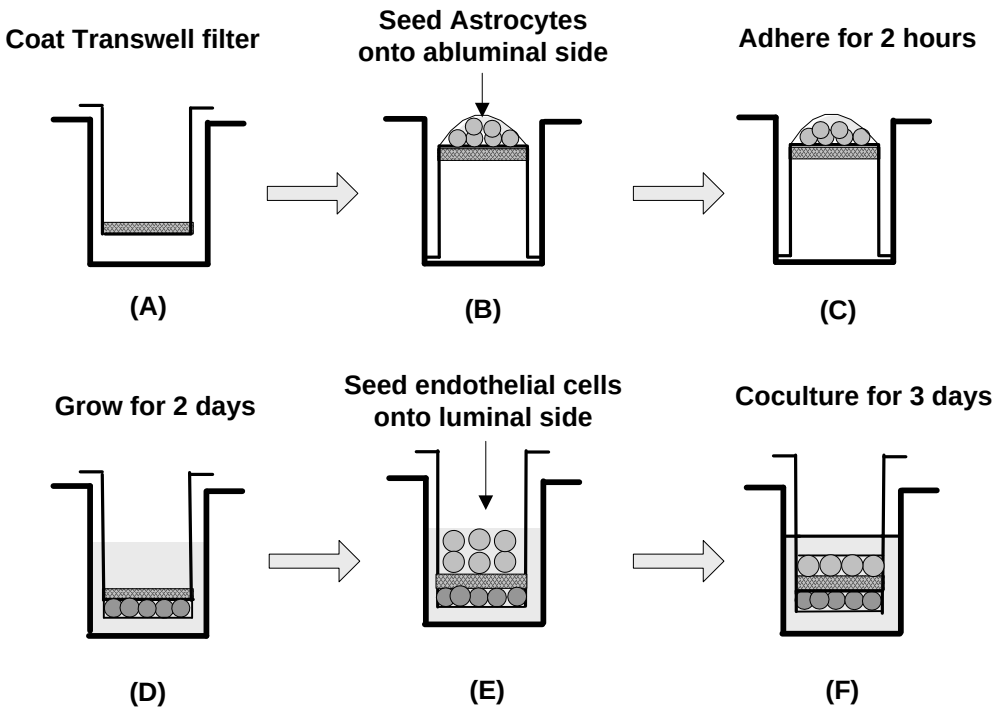

Figure 4.1 The experimental procedure for coculturing the bEnd3 cells and astrocytes on different sides of the Transwell filter with 0.4 μm diameter pores. The Transwell filter consists of a porous membrane support submerged in culture medium. The Transwell filters were coated with fibronectin or basement membrane substitute (**A**). Astrocytes were first seeded onto the abluminal side of the inverted Transwell filter at a density of 2.75×10^4 cells per filter (**B**), allowed to adhere for 2 hours (**C**), then the filter was flipped back and the astrocytes were cultured for 2 days in DMEM supplemented with 10% FBS and 1% PS (**D**). At the end of the second day, bEnd3 cells were seeded onto the luminal side of Transwell filter at a density of 6.6×10^4 cells per filter (**E**) and cocultured with astrocytes for an additional 3-4 days (**F**). The culture medium for the bEnd3 cells on the luminal side of the Transwell filter was DMEM supplemented with 10% FBS, 1% PS and 3mM L-Glutamine.

Basement membrane coating

We used Matrigel and a mixture of collagen types I and IV as the basement membrane substitutes for our *in vitro* BBB models. For Matrigel coating, Matrigel (BD Biosciences, Bedford, MA) was diluted in Dulbecco's PBS (DPBS; Mediatech, Herndon, VA) to a concentration of 476 μg/ml. The Transwell filter was reversed and 200 μl of diluted Matrigel solution was added to the abluminal side of each Transwell filter. The

Transwell plate containing the filters was placed in a 37 ℃, 5% CO_2-95% air incubator for 3 hr for the Matrigel to gel. For collagen mixture coating, types I and IV collagen (BD Bioscience, Bedford, MA) were diluted in DPBS to 0.5 mg/ml and their pH brought to 7.4 with NaOH and HCl respectively. The two collagens were then mixed thoroughly (40:60, collagen I: collagenIV, v/v) and 200 μl of the mixture was added to the luminal side of each Transwell filter. The Transwell plates with filters were incubated at 37 ℃ for 1 hr for the mixture to gel. After that, the Matrigel and collagen mixture coated Transwell filters were placed into a sterile hood and allowed to air dry for 24-72 hrs. Once dry, filters were stored at 4–8 ℃ for up to two weeks. The coated filters were rehydrated in DPBS for 1hr in a 37 ^{o}C, 5%CO_2-95% air incubator prior to cell seeding.

Immunostaining of junction proteins

Astrocytes and bEnd3 cells were grown on Transwell filters as described above. For staining astrocytes, the cells were washed 3× with DPBS, fixed in 3.7% formaldehyde for 15 min, washed 3× with DPBS, permeabilized with 0.1% Triton X-100 in DPBS for 10 min and then blocked with 5% horse serum (Sigma, St. Louis, MO) in DPBS for 30 min. The astrocytes were then incubated with rabbit anti-glial fibrillary acidic protein (GFAP, Sigma, St. Louis, MO) overnight at room temperature. The astrocytes were then washed 3× with DPBS and incubated with Alexa Fluor 594 goat anti-rabbit secondary antibody (1:200; Invitrogen, Carlsbad, CA) for one hour at room temperature. For nucleus couterstaining, the astrocytes were incubated in 4', 6-diamidino-2-phenylindole (DAPI, 1:500; Invitrogen, Carlsbad, CA) for 15 min at room temperature. For cytoplasm staining, separate unfixed astrocyte monolayers were washed 3× with DPBS and then incubated in Calcein AM (1:500; Invitrogen, Carlsbad, CA) for 15 min at

37°C.

For immunostaining bEnd3 cells, monocultures or cocultures were washed 2× with DPBS, fixed in 1% paraformaldehyde for 10 min, permeabilized with 0.2% Triton X-100 in DPBS for 10 min and blocked with 10% bovine serum albumin (BSA) and 0.1% Triton X-100 in DPBS for 1 hr. After washing with DPBS, the monolayers were incubated with a primary antibody for claudin-5, occludin, ZO-1 or VE-caherin (1:200; Zymed, San Francisco, CA) for 3 hrs at room temperature or overnight at 4°C. The cell monolayers were then washed 5× with DPBS and incubated with an Alexa Fluor 488 donkey anti-rabbit IgG secondary antibody (1:200; Invitrogen, Carlsbad, CA) for 1 hr at room temperature. The nuclei were counterstained by incubating with propidium iodide (PI, 1:1000; Invitrogen, Carlsbad, CA) for 15 min.

Immunostained cells were observed with a Nikon Eclipse TE2000-E microscope. Images were taken with a Photometrics Cascade 650 CCD camera from Roper Scientific (Tucson, AZ).

RNA extraction and gene expression analysis

Total RNA was isolated from bEnd3 cells using TRIzol LS reagent (Invitrogen, Carlsbad, CA) and quantitative reverse transcription-polymerase chain reaction (RT-qPCR) was conducted to analyze gene expression as previously described (Shi et al.). RNA was first converted to cDNA, and then real-time PCR was performed on the ABI PRISM 7000 sequence detection system (Applied Biosystems, CA). β-actin served as an internal control. The PCR reactions were performed in 25μl reaction mixture volumes containing SYBR Green PCR Master Mix (Applied Biosystems), cDNA, and specific primer pairs. RT-qPCR programs were set to 15 min at 95℃, followed by 40 cycles of 20

s at 95 ℃, 30 s at 55 ℃, and 30 s at 72 ℃. The specificity of the amplification reaction was assessed by performing a dissociation curve analysis. Table 4.1 lists the primer sequences used in the PCR experiments.

Table 4.1 Real-time PCR primers for junction proteins

Protein	Accession number	Forward primer (5' to 3')	Reverse primer (5' to 3')	Reference
claudin 5	NM_ 013805	TAA GGC ACG GGT AGC ACT CA	GCC CAG CTC GTA CTT CTG TG	
occludin	NM_ 008756.2	ATC CTG TCT ATG CTC ATT ATT GTG	CTG CTC TTG GGT CTG TAT ATC C	(Wang et al., 2006b)
VE-cadherin	X83930	TCC TCT GCA TCC TCA CTA TCA CA	GTA AGT GAC CAA CTG CTC GTG AAT	(Wang et al., 2006a)
ZO-1	NM_009386.2	GGA GCT ACG CTT GCC ACA CT	GGT CAA TCA GGA CAG AAA CAC AGT	(Johnston et al., 2004)
β-actin	NM_007393.2	GTC GTA CCA CAG GCA TTG TGA TGG	GCA ATG CCT GGG TGC ATG GTG G	(Yamamoto et al., 2005)

Measurement of L_p and P

The hydraulic conductivity L_p and solute diffusivity P of the cell layers were measured using a previously developed bubble tracker system and automated fluorometer system as shown in **Fig. 4.2** (Cancel *et al.*, 2007; Cancel and Tarbell, 2010). Briefly, the Transwell filter containing cultured cell layers was sealed within a transport chamber to form luminal and abluminal compartments. The transport chamber was connected to a laser excitation source and an emission detector via optical fibers. The fluorescent tag of the test solute in the abluminal chamber was excited by the excitation light produced by a 10-mW Crystal laser and the emission was counted by a photon counting detector. The data was recorded by the *FluoroMeasure* acquisition software (C&L Instruments, Hummelstown, PA). The abluminal compartment of the transport chamber was also connected to a water reservoir by a Tygon and borosilicate glass tube as shown in **Fig. 4.2**.

A hydrostatic pressure difference could be created across the filters by adjusting the height of the reservoir with respect to the height of the fluid covering the cell layers. Water flux across the cell layers was measured by tracking the position of a bubble pre-inserted into the glass tube. Both the luminal compartment and abluminal reservoir were continuously supplied with 5% CO_2- 95% air to maintain the pH of the medium at 7.4. The temperature of the whole permeability measurement system was maintained at 37°C.

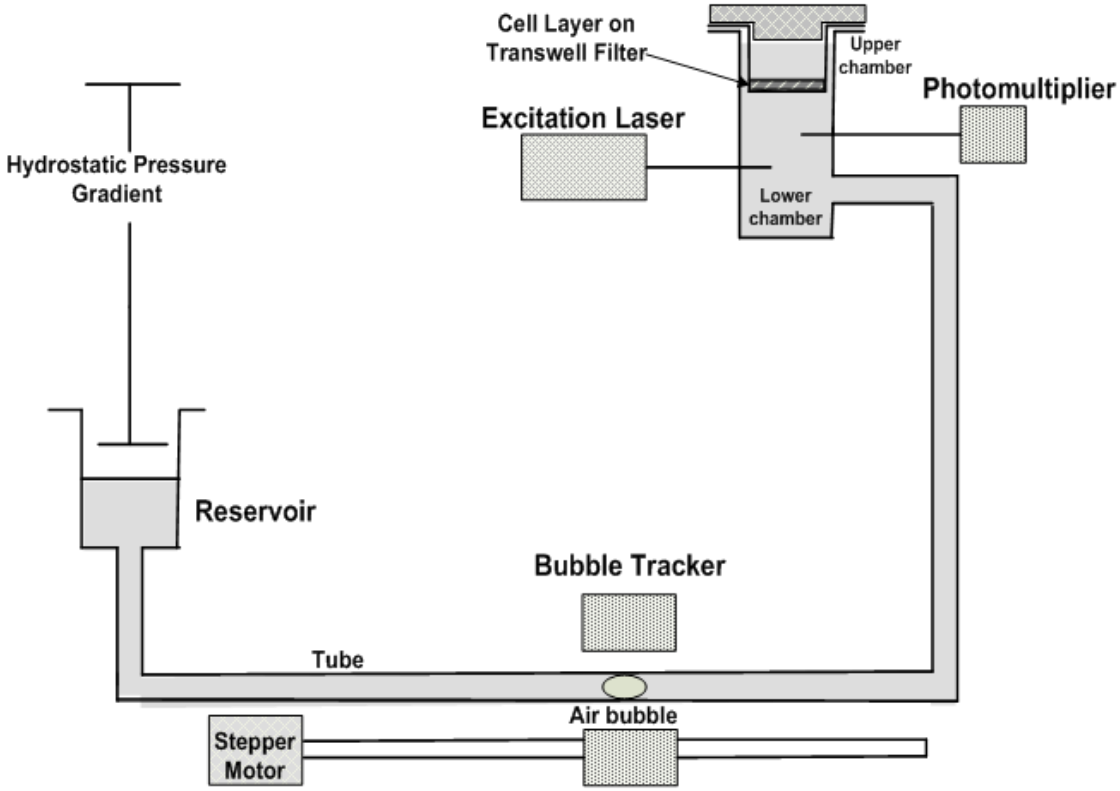

Figure 4.2 Schematic of the experimental system used to measure the permeability of the *in vitro* BBB models to water and fluorescently-labeled solutes. The Transwell filter with the cell layers was sealed in a chamber. For solute transport, the fluorescently-labeled test solute was added to the upper chamber, transport of test solutes across the cell layer was quantified by an automated fluorometer and the solute permeability was calculated accordingly. For water transport, the reservoir was lowered to create a pressure gradient across the cell layer, the water flux across the cell monolayer was measured by a bubble tracker, and the hydraulic conductivity was determined accordingly.

Before the transport experiment, the abluminal compartment of the chamber was

filled with the experimental medium (1% bovine serum albumin and 1% Penicillin/Streptomycin in DMEM medium free of phenol red). The Transwell filter with the cell layer was rinsed twice with the experimental medium and then sealed in the transport chamber. A high concentration of test solute with fluorescent tag was added to the luminal compartment of the chamber. Each experiment lasted three hours: the first hour for equilibration, the second hour for data collection under convective condition ($\Delta p=10 cmH_2O$), and the final hour of data collection under diffusive conditions ($\Delta p=0$).

Calculation of L_p and P

During the second hour of the transport experiments, the reservoir was lowered by 10cm, thus applying a hydraulic pressure difference of 10 cmH_2O across the cell layer. To measure the volumetric flow rate (J_v), the air bubble displacement was tracked and converted to J_v according to the following equation

$$J_v = (\Delta d / \Delta t) \times F \tag{4.1}$$

where $\Delta d / \Delta t$ is the bubble displacement rate, and F is a tube calibration factor (fluid volume occupying a known length of tubing). Because the upper and lower chambers contained the same medium (DMEM with 1%BSA), there was no osmotic pressure difference across the cell layer. The hydraulic conductivity L_p was thus calculated as (Michel and Curry, 1999)

$$L_p = J_v / A / \Delta p \tag{4.2}$$

where A is the surface area of the Transwell filter ($1.1 cm^2$), and Δp is the hydraulic pressure difference across the cell layer.

The fluorescence intensity in the abluminal compartment was recorded during the experiment and converted to concentration through a calibration curve. The solute flow

across the cell layer (J_s) was calculated by the following equation

$$J_s = (\Delta C_a / \Delta t) \times V_a \tag{4.3}$$

where $\Delta C_a/\Delta t$ is the rate change of concentration in the lower chamber and V_a is the fluid volume in the lower compartment. The diffusive solute permeability (P) was then calculated by

$$P = J_s / A / (C_L - C_a) = J_s / A / C_L \tag{4.4}$$

where C_L is the solute concentration in the upper compartment, and A is the surface area of the filter. The concentration in the lower chamber C_a was neglected in Eq.4 because the solute concentration in the upper chamber, C_L, is much larger than C_a.

To calibrate the fluorometer system, ten different concentrations of test solute were made according to the test solute concentration in the abluminal compartment obtained during a typical experiment. The fluorescent intensity of 3ml of each solution was measured for 20min in each chamber. A linear regression of the concentration vs average intensity data was used to create a calibration curve.

The L_p and P measurements included both the cell layers and the Tranwell insert. The Transwell insert itself also provides resistance to the transport of water and solutes, therefore we also measured the L_p and P of the Transwell insert to various-sized solutes. The final permeability results presented for the *in vitro* models were adjusted to account for the Transwell insert.

Measurement of Transendothelial Electrical Resistance (TER)

The TERs of the *in vitro* BBB models grown on the Transwell inserts were recorded using an Endohm chamber connected to an EVOM resistance meter (World

Precision Inst. Inc., Sarasota, FL). The TER of each model was calculated after subtracting the TER of the blank Transwell filters and reported as Ωcm^2.

Statistical analysis

The L_p and P are presented as mean ± SD. Data were analyzed for statistical significance by ANOVA with $p < 0.05$ being considered statistically significant.

4.3 Results

Immunostaining of astrocytes

The astrocytes used in our *in vitro* BBB models were isolated from 8-10 days old rats. Since brain tissue contains many other cell types such as neurons, endothelial cells, and glial cells, it was important to examine the purity of the primary astrocyte cultures. Astrocytes were immunolabeled with an antibody against GFAP (red) as shown in **Fig. 4.3A**, and counterstained with cell nucleus dye DAPI (blue). Since DAPI stains the nuclei of all cell types while GFAP is only specific to astrocytes, the purity of astrocytes could be determined by matching the astrocyte body with the corresponding cell nucleus. As shown in **Fig. 4.3A**, the percentage of astrocytes was higher than 90%. For the transport experiments, it was required that the cells formed a confluent monolayer. **Figures 4.3B, C** demonstrate the fluorescence labeling of cytoplasm and GFAP of astrocytes both in monoculture and in coculture with bEnd3 cells, respectively. Astrocytes formed a fairly complete cell layer in both cases. Due to the special morphology of astrocytes, in some regions astrocyte foot processes were on top of other cell bodies so that the astrocyte monolayer was not as flat and compact as the endothelial monolayer.

(A)

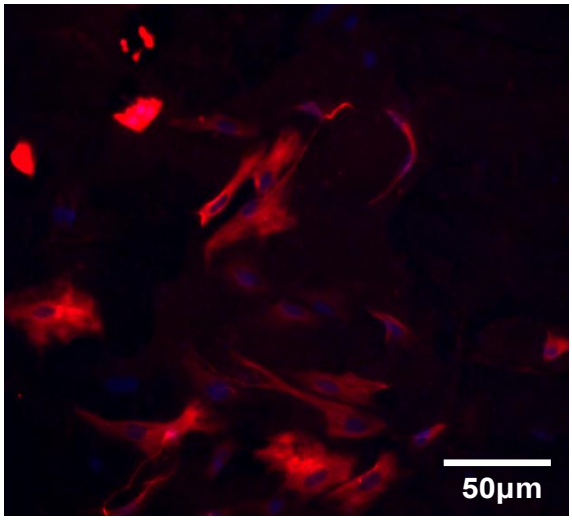

(B)

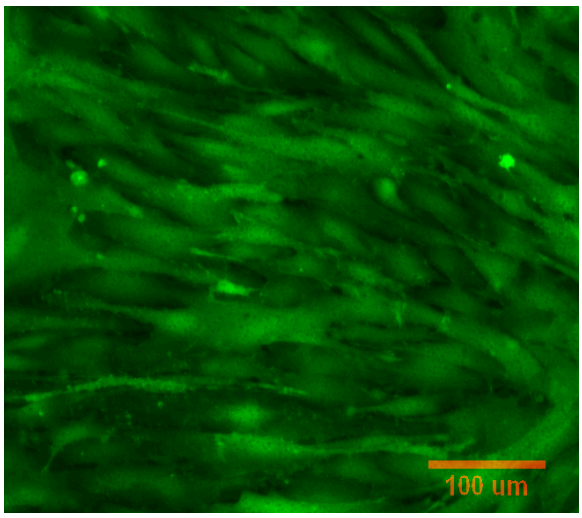

(C)

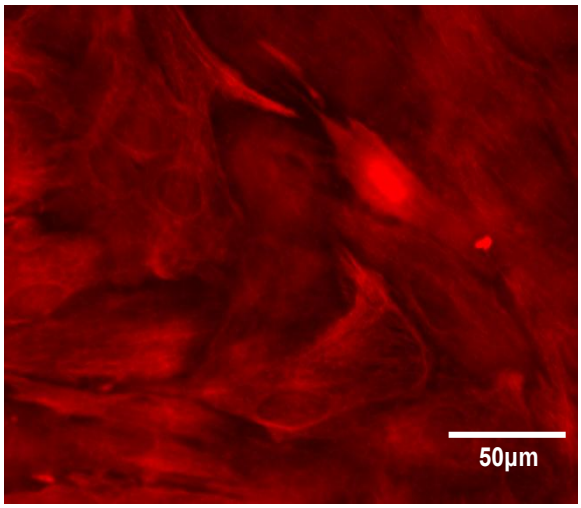

Figure 4.3 Immunostaining results for astroyctes **(A)** Astrocytes immunolabeled with antibodies against glial fibrillary acidic protein (GFAP, red) and counterstained with cell nucleus dye DAPI (blue). Primary astrocytes (passage P3-P5) were seeded on the luminal side of the Transwell filter at a density of 5.5×10^3 cells per filter and cultured for 3 days

before immunostaining. The purity of isolated astrocytes was >90%. **(B)** Cytoplasmic labeling (green) of the astrocyte monoculture by Calcein AM. Astrocytes were seeded onto the luminal side of the Transwell filter at a seeding density of 2.75×10^4 cells per filter and grown for 5 days, forming a confluent monolayer on the luminal side of the Transwell filter which was used to perform the permeability measurement. **(C)** Labeling of GFAP (red) in astrocytes when cocultured with bEnd3 cells at the end of 5^{th} day.

Protein and gene expressions of bEnd3 monolayer and coculture

The expression of various junction proteins in our *in vitro* BBB models was examined by immunostaining. **Figure 4.4** shows images of the tight junction transmembrane protein claudin-5 (**Figs. 4.4A, B**), occludin **(Figs. 4.4C, D)**, accessory protein ZO-1(**Figs. 4.4E, F**), and adherens junction transmembrane protein VE-cadherin **(Figs. 4.4G, H)**. The left column shows staining of the bEnd3 monolayer alone, while the right column shows bEnd3 cells cocultured with astrocytes. In both cases, the bEnd3 cells formed confluent monolayers on the luminal side of the Transwell filter. Coculture with astrocytes did not alter the expression of claudin-5, occludin, ZO-1, and VE-cadherin of endothelial cells.

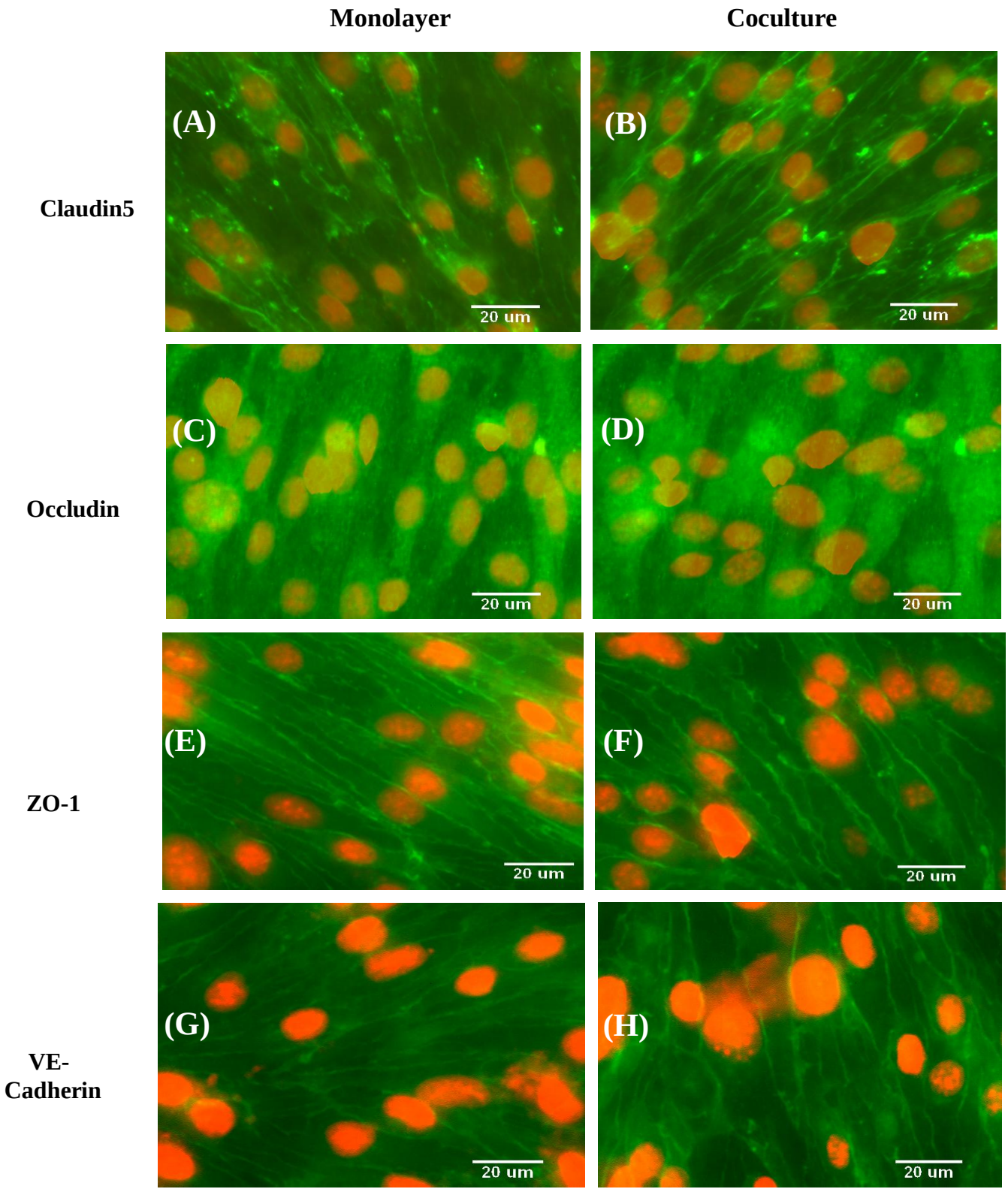

Figure 4.4 Comparison of essential junction proteins expressed by bEnd3 cells when cultured alone (left panel) or cocultured with astrocytes (right panel). Immunostaining of claudin-5 **(A, B)**; occludin **(C, D)**; ZO-1 **(E, F)**; and VE-cadherin **(G, H)**. Endothelial

cells were seeded to the luminal side of the Transwell filter with a density of 6.6×10^4 cells per filter and cultured for 3-4 days in DMEM supplemented with 10%FBS, 1%PS and 3mM Glutamine (left panel). Astrocytes were seeded onto the abluminal side with a density of 2.75×10^4 cells per filter two days before endothelial cell seeding and then cultured in DMEM supplemented with 10%FBS for an additional 3-4 days (right panel).

The gene expression of various junction proteins in the bEnd3 monocultures and cocultures is shown in **Fig.4.5**. RNA was isolated from the confluent bEnd3 cell layer grown on the Transwell filter and the RT-qPCR was performed for claudin-5, occludin, ZO-1, VE-cadherin, and actin (internal control). The empty and filled bars show the results for the bEnd3 monolayer and the bEnd3 layer cocultured with astrocytes, respectively. As shown in **Fig. 4.5,** there was no significant difference in the mRNA level of all four junctional proteins between the bEnd3 monoculture and coculture, though the mRNA level for each of the proteins was slightly increased when the bEnd3 cells were cocultured with astrocytes ($p > 0.2$). These results indicate that there was no dramatic change in the expression of junction protein components when bEnd3 cells were exposed to astrocytes for 3-4 days. The gene expression result was consistent with the observation of junction protein expression by immunostaining.

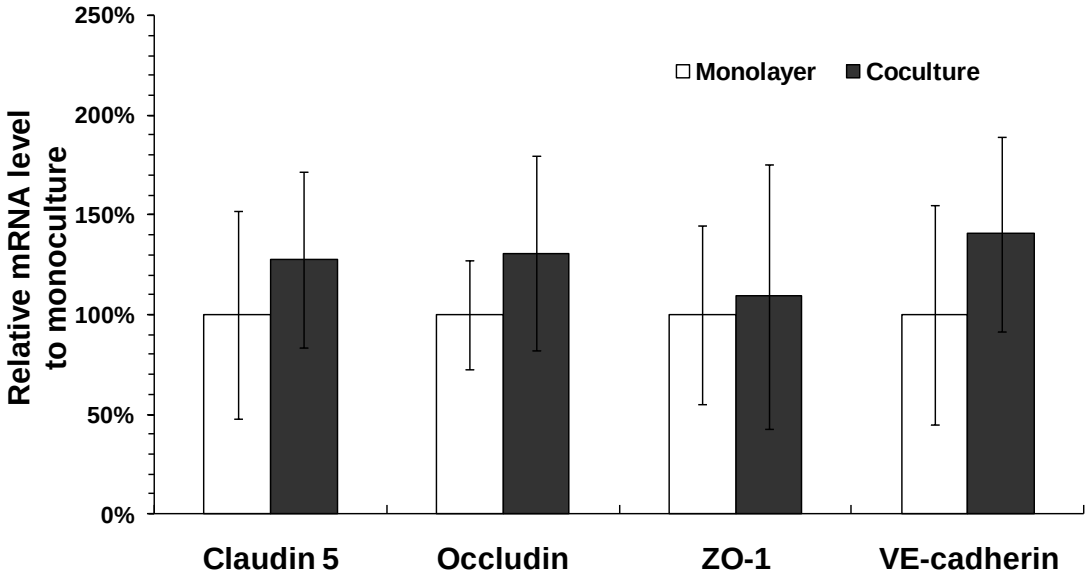

Figure 4.5 Comparison of gene expressions of bEnd3 cells by RT-qPCR when cultured alone (empty bars) and cocultured with astrocytes (filled bars) for claudin-5, occludin, ZO-1, VE-cadherin. Data shown in mean ± SD (n=3).

Hydraulic conductivity (L_p) of in vitro BBB models

Figure 4.6 shows the measured hydraulic conductivity (L_p) of the *in vitro* BBB models: astrocyte monoculture and astrocyte monoculture on top of Matrigel (Astrocyte + Matrigel) as negative controls; bEnd3 monoculture; coculture of astrocytes and bEnd3 on different sides of the Transwell filter (coculture); coculture with the collagen type I and IV mixture (coculture + collagen mixture) and coculture with the Matrigel (coculture + Matrigel) coating on the luminal side of the Transwell filter. L_p of astrocyte monoculture was $5.0 \pm 2.7 \times 10^{-7}$ (n=15) cm/s/cmH_2O, which was slightly lower than that of the astrocyte monoculture with Matrigel, $5.1 \pm 2.9 \times 10^{-7}$ (n=10) cm/s/cmH_2O. L_p of bEnd3 monoculture was $1.7 \pm 1.1 \times 10^{-7}$ (n=15) cm/s/cmH_2O, which was ~1/3 of that of the astrocyte monoculture with or without Matrigel coating ($p < 0.01$). The L_p of the coculture of bEnd3 with astrocytes was $1.4 \pm 0.6 \times 10^{-7}$ (n=16) cm/s/cmH_2O, ~18% lower

than that of bEnd3 monoculture, but not significantly different (p=0.13). Coating with a mixture of collagen types I and IV decreased the L_p of the cocultures to $1.1 \pm 0.9 \times 10^{-7}$ (n=10) cm/s/cmH_2O but not significantly (p=0.07), while coating with Matrigel insignificantly increased the L_p of cocultures to $1.6 \pm 0.8 \times 10^{-7}$ (n=8) cm/s/cmH_2O (p=0.45). These results suggest that bEnd3 cells provide the majority of the resistance to water transport in our *in vitro* BBB models.

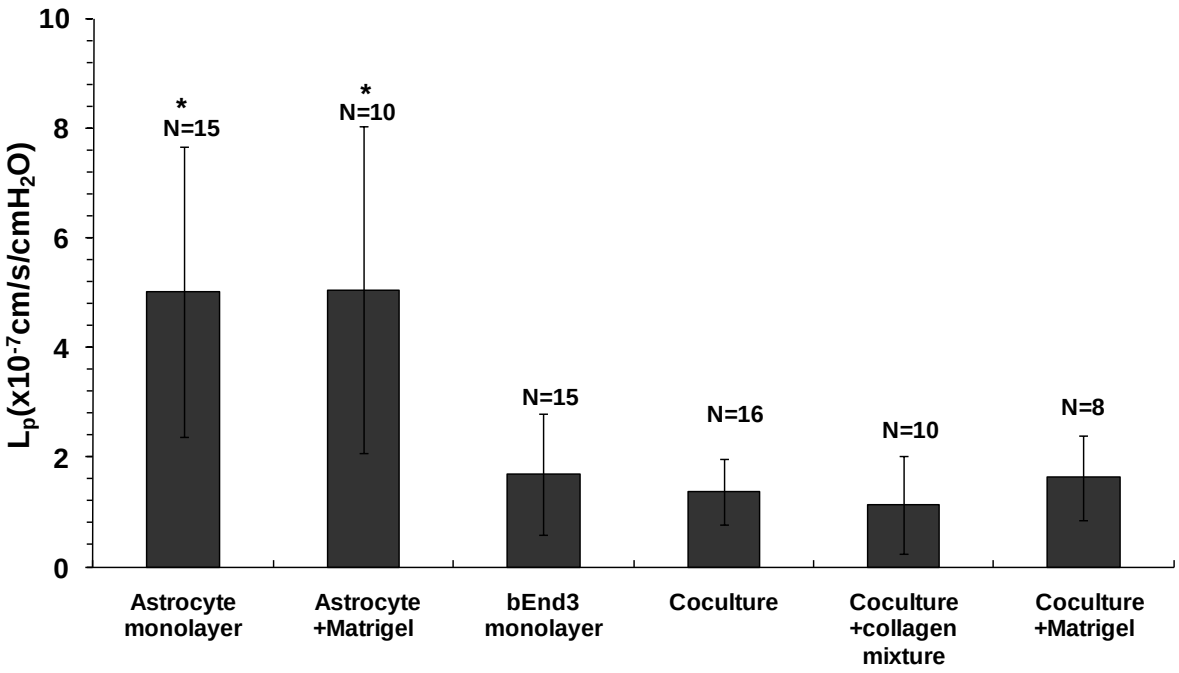

Figure 4.6 Hydraulic conductivity (L_p) of the *in vitro* BBB models: astrocyte monoculture, astrocyte monoculture on top of a thin Matrigel coating (Astrocyte +Matrigel), bEnd3 monoculture, coculture of astrocytes and bEnd3 cells on different sides of a Transwell filter (coculture), coculture with a thin coating of a mixture of collagen types I and IV on the luminal side of a Transwell filter (coculture + collagen mixture), coculture with a thin Matrigel coating on the abluminal side of a Transwell filter (coculture + Matrigel). The values are presented as mean ± SD. * $p<0.05$ compared to bEnd3 monolayer.

Diffusive permeability (P) of in vitro BBB models to different-sized solutes

Figure 4.7 shows the measured diffusive permeability (P) of the *in vitro* BBB models to three different-sized solutes: **(A)** TAMRA (MW=467), **(B)** Dextran 10K and **(C)** Dextran 70K. P^{TAMRA}, P^{Dex10k} and P^{Dex70k} of the astrocyte monoculture were 30.9 ± 18.7 (n=10), 4.1 ± 1.2 (n=12), and 0.9 ± 0.4 (n=13) $\times 10^{-6}$ cm/s, respectively. Coating with Matrigel insignificantly increased P^{TAMRA}, P^{Dex10k}, and P^{Dex70k} of the astrocyte monoculture to 31.5 ± 12.5 (n=8), 4.5 ± 1.7 (n=11), and 1.2 ± 0.4 (n=18) $\times 10^{-6}$ cm/s ($p > 0.11$), respectively. P^{TAMRA}, P^{Dex10k}, and P^{Dex70k} of bEnd3 monoculture were 8.1 ± 3.6 (n=7), 1.0 ± 0.45 (n=15) and 0.21 ± 0.07 (n=14) $\times 10^{-6}$ cm/s, respectively, which were 18-26% lower than those of the astrocyte monoculture with or without Matrigel coating ($p<0.02$). P^{TAMRA}, P^{Dex10k}, and P^{Dex70k} of the coculture of bEnd3 with astrocytes were 5.9 ± 1.9 (n=10), 0.78 ± 0.24 (n=10) and 0.16 ± 0.09 (n=11) $\times 10^{-6}$ cm/s, respectively, which were 20-27% lower than those of the bEnd3 monoculture, but this difference was not significant ($p>0.13$). Coating with the mixture of collagen types I and IV insignificantly decreased P^{TAMRA}, P^{Dex10k}, and P^{Dex70k} of the coculture to 5.8 ± 2.2 (n=8), 0.67 ± 0.24 (n=12) and 0.16 ± 0.09 (n=11) $\times 10^{-6}$ cm/s, respectively ($p > 0.27$), while coating with Matrigel insignificantly increased P^{TAMRA}, P^{Dex10k}, and P^{Dex70k} of the coculture to 6.0 ± 2.5 (n=16), 0.84 ± 0.20 (n=7) and 0.17 ± 0.07 (n=10) $\times 10^{-6}$ cm/s, respectively ($p>0.6$). These results suggest that the endothelium of the *in vitro* BBB also provides the majority of the resistance to the transport various-sized solutes.

(A)

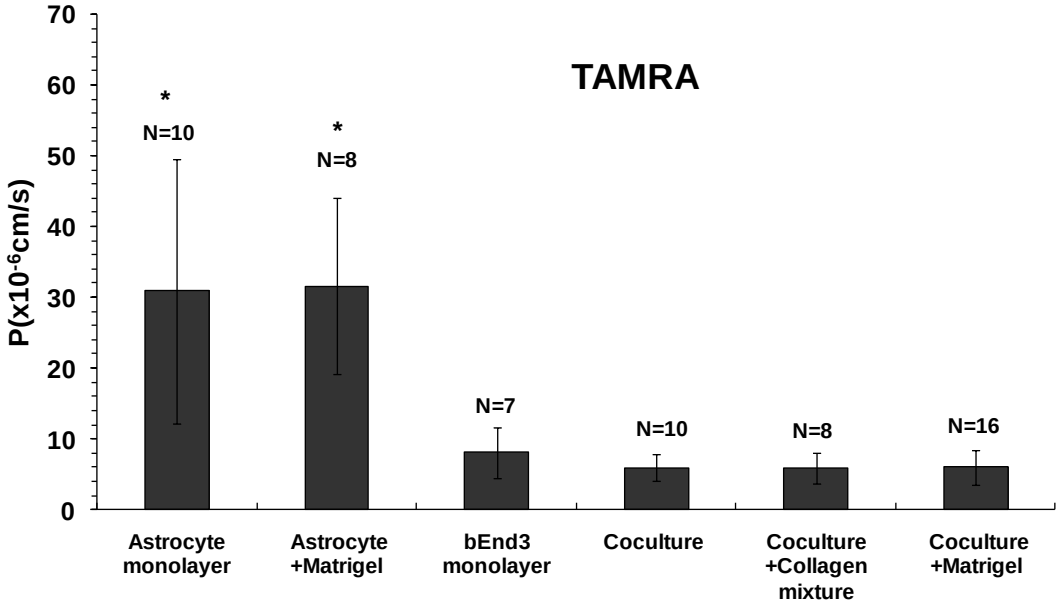
TAMRA
P(x10-6cm/s)
70
60
50
40
30
20
10
0
*
N=10
*
N=8
N=7
N=10
N=8
N=16
Astrocyte monolayer
Astrocyte +Matrigel
bEnd3 monolayer
Coculture
Coculture +Collagen mixture
Coculture +Matrigel

(B)

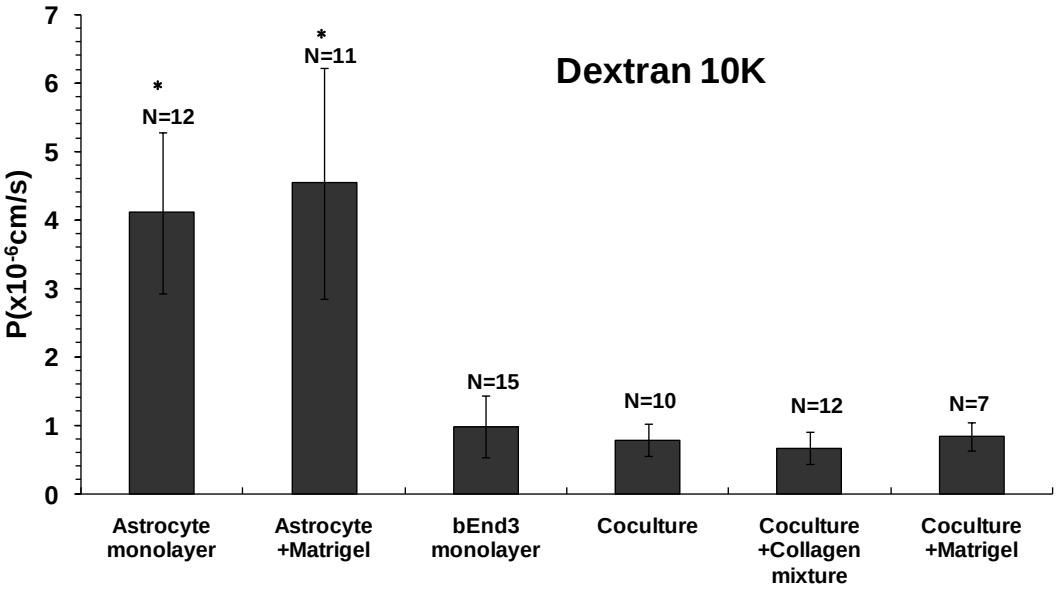
Dextran 10K
P(x10-6cm/s)
7
6
5
4
3
2
1
0
*
N=12
*
N=11
N=15
N=10
N=12
N=7
Astrocyte monolayer
Astrocyte +Matrigel
bEnd3 monolayer
Coculture
Coculture +Collagen mixture
Coculture +Matrigel

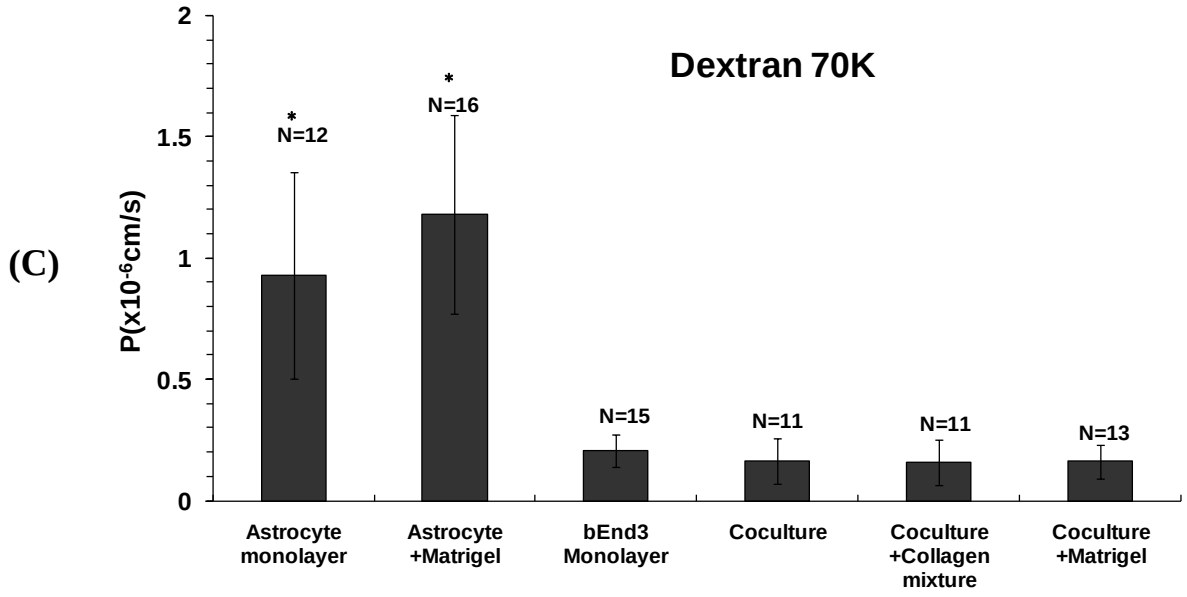

Figure 4.7 Diffusive permeability (P) of the *in vitro* BBB models to three solutes: **(A)** Tetramethyl-6-Carboxyrhodamine(TAMRA) (MW=467); **(B)** Dextran 10K; **(C)** Dextran 70K. The definitions for the *in vitro* BBB models are the same as in **Fig. 4.6**. The values are presented as mean ± SD. *p< 0.01 compared to bEnd3 monolayer.

Transendothelial Electrical Resistance (TER) of in vitro BBB models

We also measured the TER of our *in vitro* models. After culturing for 5 days, the astrocyte monolayer had a TER of 8.6 ± 3.2 (n=3) Ωcm^2; the astrocyte monolayer on Matrigel had a lower TER of 4.0 ± 1.8 (n=4) Ωcm^2. After culturing or coculturing for 3-4 days, bEnd3 monolayers had a TER of 19.6 ± 2.7 (n=7) Ωcm^2; coculture had a higher TER of 30.3 ± 6.4 (n=6) Ωcm^2; coculture with collagen I and IV mixture had a TER of 24.2 ± 1.3 (n=10) Ωcm^2 while coculture with Matrigel had a TER of 33.4 ± 2.8 (n=3) Ωcm^2. **Figure 4.8** shows the percent difference of the TER of each *in vitro* model compared to the bEnd3 monoculture. The TERs of the astrocyte monoculture and astrocyte monoculture on Matrigel were only 44% and 20% of the bEnd3, respectively ($p < 0.02$). However, coculture, coculture with collagen mixture and coculture with Matrigel

had TERs that were 154%, 123% and 170% of the bEnd3 monolayer, respectively ($p < 0.01$).

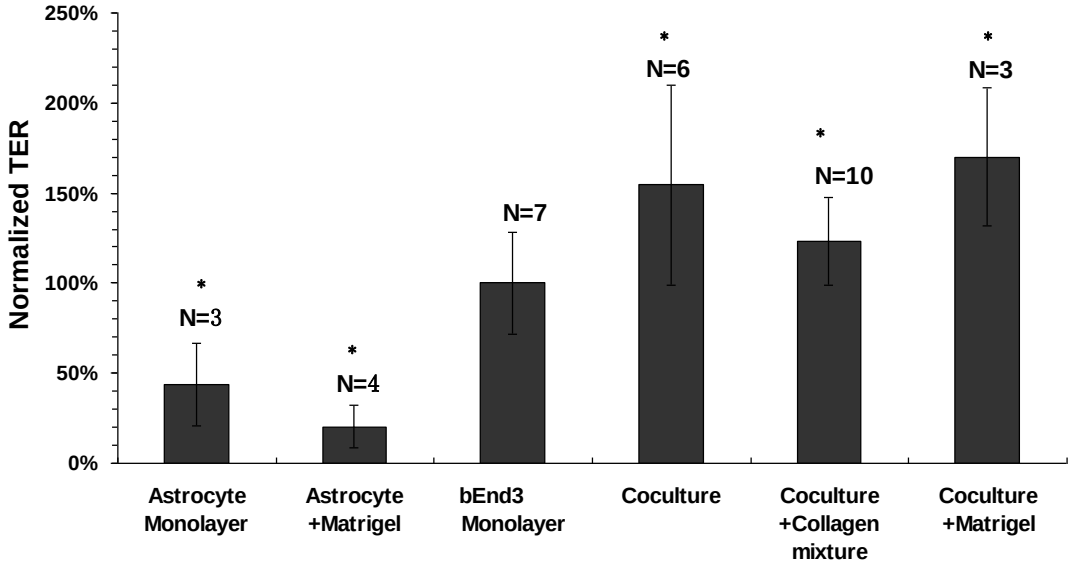

Figure 4.8 The ratio of the transendothelial electrical resistance (TER) of different *in vitro* BBB models to that of the bEnd3 monolayer. The abbreviations for the *in vitro* BBB models are the same as in **Fig. 4.6**. The values are presented as mean±SD. *p< 0.02 compared to bEnd3 monolayer.

Resistance from different components of in vitro BBB models

To investigate the contribution of different structural components to the BBB permeability regulation, the percentage resistances of astrocyte monolayer, bEnd3 monolayer, and basement membrane substitute (collagen I & IV mixture, Matrigel) were calculated by normalizing their resistance compared to the total resistance of the coculture + basement membrane model. The resistances of different types of *in vitro* BBB models to water and different-sized solutes (TAMRA, dextran 10K, and dextran 70K) are listed in Table 3.2. From Table 3.2, we can see that astrocyte monolayer, bEnd3 monolayer, and basement membrane accounts for 15-22%, 70-80%, and 2-9% of the total resistances for solute transport. For water transport, astrocyte monolayer, bEnd3

monolayer, and basement membrane accounts for 22-24%, 67-74%, and 2-10% of the total resistances. In conclusion, bEnd3 are the major contributor for restricting water and solute transport in our *in vitro* BBB model. This result is consistent with the observations that the permeability of bEnd3 monolayer and coculture systems are not significantly different from each other.

Table **4.2** The percentage resistances of different structural components of *in vitro* BBB

Solutes	**in vitro BBB models**	**astrocyte monolayer**	**bEnd3 monolayer**	**basement membrane**
water	Coculture +collagen mixture	22.6%	67.4%	10.1%
	Coculture+Matrigel	24.6%	73.2%	2.2%
TAMRA	Coculture +collagen mixture	18.8%	72.0%	9.3%
	Coculture+Matrigel	19.3%	74.2%	6.4%
Dex 10K	Coculture +collagen mixture	20.1%	70.1%	9.7%
	Coculture+Matrigel	22.0%	76.5%	1.5%
Dex 70K	Coculture +collagen mixture	15.4%	76.6%	8.0%
	Coculture+Matrigel	15.9%	78.7%	5.4%

4.4 Discussion

In this study, we characterized four *in vitro* BBB models by examining the expression of junction proteins that characterize the endothelium and quantifying their permeability to water and solutes. The immortalized mouse brain microvessel endothelial cell line bEnd3 showed good expression of essential junction proteins: claudin-5,

occludin, ZO-1, and VE-cadherin, while the primary rat astrocytes used in the coculture expressed GFAP.

Basement membrane (BM) is an important structural component of the BBB which has not been included in previous *in vitro* models of the BBB. In this work, two BM substitutes (Matrigel and collagen type I and IV mixture) were used and their effect on the transport properties of the BBB was examined. Although the major collagen existing in the native BM of the BBB is type IV (Leblond and Inoue, 1989; Miosge, 2001; Kleinman and Martin, 2005; LeBleu *et al.*, 2007) , we used a mixture of type I and IV (40:60, v/v) because collagen IV alone cannot form a gel. Among the tested *in vitro* models, the one with the collagen I and IV mixture had the lowest permeability, indicating that this mixture can enhance the integrity of the BBB. In contrast, the *in vitro* models with Matrigel had the highest permeability, suggesting that it is not a good BM for growing a tight BBB *in vitro*.

Astrocyte foot processes cover ~99% of the abluminal surface of cerebral microvessels *in vivo* (Pardridge, 1999). The proximity of astrocytes to endothelial cells is thought to be important for the normal function of the BBB(Abbott, 2002) . In this work, we examined the expression of the specific astrocytic protein, GFAP, and measured the permeability of an astrocyte monoculture, astrocyte monoculture with Matrigel, and astrocyte coculture with bEnd3 cells, and an astrocyte coculture with bEnd3 cells containing either a collagen I and IV mixture or Matrigel. **Figures 4.6** and **4.7** indicate that astrocytes provide ~25% of total BBB resistance to water and ~20% of the resistance to various-sized solutes. The endothelium provides ~75-80% of the *in vitro* BBB resistance.

Among the tested *in vitro* BBB models, the coculture of bEnd3 cells and astrocytes with the collagen I and IV mixture had the lowest permeability to water and solutes, although there was no significant difference between the coculture and the bEnd3 monoculture. **Figure 4.9** shows a comparison of our measured diffusive solute permeabilities (P) with *in vivo* data from rat pial microvessels from Yuan et al.(Yuan et al., 2009b), and data from an *in vitro* coculture model from Gaillard and Boer that used bovine brain capillary endothelial cells and rat astrocytes (Gaillard and de Boer, 2000). P was plotted as a function of the Stokes radius of the solutes. The Stokes radii for all the solutes except Dextran 70K were calculated using the Stokes-Einstein Equation based on their measured diffusion coefficients in the aqueous solution(Lawrence et al., 1994; Braeckmans et al., 2003; Braga et al., 2004; Sugaya et al., 2006) . The Stokes radius of Dextran 70K was estimated from that of albumin with similar molecular weight(Yuan et al., 2009b). The measured P of our bEnd3 monoculture, coculture, and coculture with collagen mixture to TAMRA, Dextrans 10K and 70K in our current study are represented by triangles, open circles and diamonds, respectively. The open squares represent data for NaFl and Dextran 4K from Gaillard and Boer (Gaillard and de Boer, 2000). The *in vivo* data for NaFl, Dextrans 4K, 10K, 20K, 40K, and 70K are represented by solid circles. For all three *in vitro* BBB models with bEnd3, the permeability to TAMRA and Dextran 10K is 2.4-3.3 and 2.6-3.8 times those of *in vivo* pial microvessels ($p < 0.005$), respectively, while the permeability to Dextran 70k is comparable to the *in vivo* data ($p > 0.2$). Our results indicate that the *in vitro* BBB models with bEnd3 cells are fairly good models for the transport of relatively large solutes across the BBB. **Figure 4.9** also shows that our *in vitro* models using bEnd3 cells and primary rat astrocytes have

comparable permeabilities to small solutes as the previous coculture model using bovine brain capillary endothelial cells and rat astrocytes (Gaillard and de Boer, 2000).

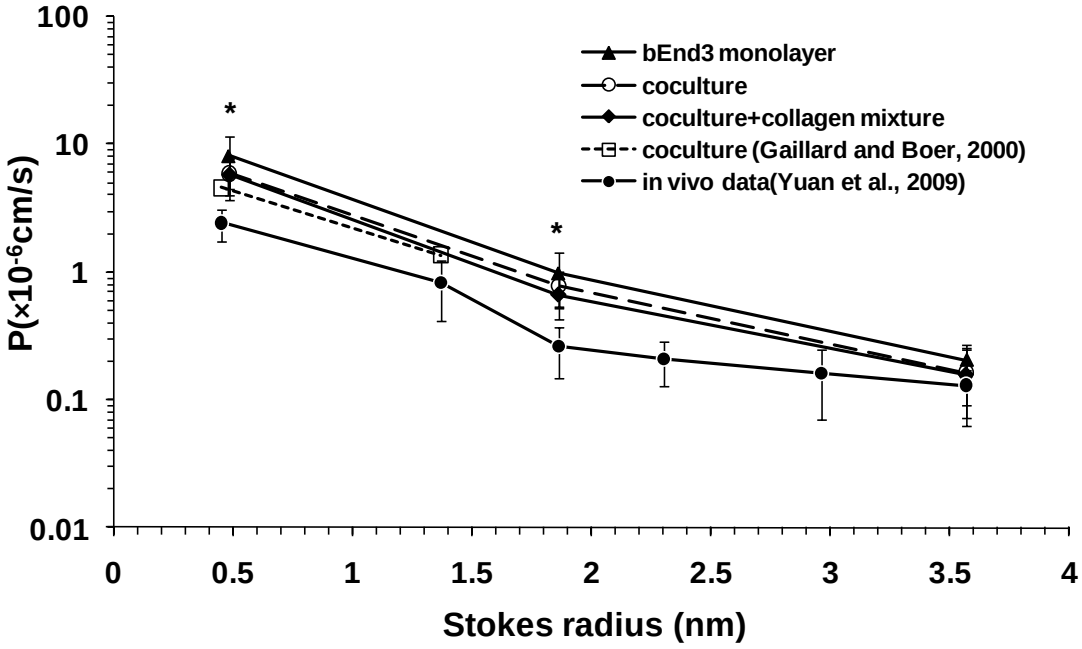

Figure 4.9 Comparison of diffusive permeability P of the bEnd3 monoculture, coculture, and coculture with collagen mixture with *in vivo* data from rat pial microvessels in Yuan et al. (2009) and that from a coculture model in Gaillard and Boer (2000). The values are presented as mean ± SD. * $p<0.005$ compared to corresponding *in vivo* data.

Fraser et al. (Fraser et al., 1990) measured an L_p of 2.0×10^{-9}cm/s/cmH_2O in frog pial microvessels *in vivo*. Compared with this *in vivo* data, L_p of all the *in vitro* BBB models are two orders of magnitude higher, indicating that our current *in vitro* models may not be ideal for water transport.

Although the TER of the bEnd3 monoculture is much smaller than ~1800 Ωcm^2, the *in vivo* value for rat cerebral microvessels (Crone and Olesen, 1982; Gumbleton and Audus, 2001; Deli *et al.*, 2005; Santaguida *et al.*, 2006; Malina *et al.*, 2009), the cocultures can increase the TER by up to 170% of that of the bEnd3 monoculture.

Fletcher et al. (Fletcher et al., 2006) developed *in vitro* BBB models using primary feline brain capillary endothelial cell monocultures and cocultures with astrocytes. The TERs of their monocultures and cocultures were 20-25 Ωcm^2 and 30-35 Ωcm^2 respectively, which are comparable to our data. Koto et al.(Koto et al., 2007) measured the TER of a bEnd3 monoculture from 1 to 11 days after confluence (or 3-13 days after cell seeding). They found that the TER increased with days of culture, reaching the maximum of ~110 Ωcm^2 at day 8, and decreased afterwards. However, we observed that culturing for more than 3 days after confluence (or 5 days after cell seeding) resulted in obvious cell overgrowth. Compared to the *in vivo* TER data, the bEnd3 monoculture and the coculture with bEnd3 cells and astrocytes on different sides of the filter are not ideal barrier models for ion transport. The porous membrane in the Transwell filter separating the bEnd3 cells and the primary astrocytes is ~10 microns thick, thus the direct contact between the two cell types was missing in our coculture models. This may be one of the reasons for the low TER of the current coculture models. Although coculture on opposite sides of the Transwell filter has resulted in TERs of up to 1650Ωcm^2 (Malina et al., 2009), and the paracine effects of glia or glioma cells have been found to be important in the induction and maintenance of BBB phenotype (Omidi et al., 2003), a coculture model with direct contact of endothelial and glial cells like astrocytes is expected to increase the transport barrier to water and small ions. In addition, using primary brain endothelial cells and primary astrocytes or other glial cells from the same species, as well as controlling the maturation time using different ECMs, may improve the TER and L_p. Furthermore, since the endothelium *in vivo* is constantly exposed to the blood flow, coculture of endothelial cells with glial cells under a dynamic flow condition should also increase the TER

(Santaguida et al., 2006).

In summary, we established and characterized four *in vitro* BBB models of either bEnd3 cultured alone, or cocultured together with astrocytes with or without basement membrane substitutes. Astrocytes alone or astrocytes with Matrigel are by no means a good barrier model for monitoring transport across the BBB. Although both bEnd3 monocultures and cocultures had relatively high permeabilities to water and ions, they had solute permeabilities comparable to that of the *in vivo* BBB, especially to relatively large solutes. The models used in this study are abundantly available, reproducible, convenient and cost effective, and thus are well suited for pharmacological studies.

CHAPTER 5 SUMMARY AND FUTURE WORKS

The blood-brain barrier protects the central nervous system from blood-borne neurotoxics and limits drug delivery into the brain because of its unique structures. The first step to develop new drugs for the CNS disease starts from searching the chemicals or drug carriers that are capable of penetrating the barrier. The transport of these drugs and drug carriers across the BBB is through either the paracellular (through tight junction, BM, and cleft between astrocytes) or the transcellular pathway.

In the first part of this study, we have developed a mathematical model to predict the permeability of water and various-sized hydrophilic solutes to the BBB, which is essential for assessing the ability of those molecules to cross the BBB. Our model predicts that compared to the peripheral microvessels with endothelium only, the BM and the wrapping astrocytes can reduce hydraulic conductivity (L_p) of the BBB and the permeability to sodium fluorescein (P^{NaFl}) by up to 6-fold when the fiber density in the BM is the same as that in the SGL. Even when the SGL and the tight junctions of the endothelium are compromised, the BM and astrocyte foot processes can still maintain the low L_p and P^{NaFl} of the BBB. This model prediction indicates that the BM and astrocytes provide great resistances to water and solute transport as well as protections to the CNS under both physiological and pathological conditions.

In the second part of this study, to investigate the charge effect of the SGL and BM on the BBB permeability to charged solutes, an electro-diffusion model for the transport of charged molecules across the BBB was developed. This model predicts the permeability of charged hrdrophilc molecules across the BBB. The charge densities in the SGL and BM were determined based on measured permeability data for positively

charged ribonuclease and negatively charged α-lactalbumin from intact rat mesenteric and pial microvessels.

The above models are very useful for quantifying the transport of water and small hydrophilic solutes (both neutral and charged) across the BBB through paracellular pathway. However, numerous therapeutic drugs or drug carriers for the treatment of CNS diseases are too large to go through the paracellular pathway. Therefore, it is important to understand the mechanism of transcellular transport (transcytosis) across the BBB if we want to efficiently deliver drugs to the CNS. The transcytosis of macromolecules across the BBB can occur by (1) nonspecific processes, e.g., adsorptive transcytosis and fluid phase, and by (2) specific mechanisms, e.g., receptor-mediated transcytosis. Nonspecific adsorptive transcytosis implies an electrostatic attachment of permeant molecule to a vesicle carrier, which translocates the probe across cells. For adsorptive transcytosis, the deciding factor is the number and affinity of binding sites. In fluid phase transcytosis, a fraction of plasmalemmal vesicles take up the bulk portion of plasma and then shuttle through the cytoplasm to reach the abluminal front where they apparently discharge their content. For fluid phase transcytosis, the rate of uptake depends on the size of vesicle or channel opening, solute concentration of the macromolecule, and the steric competition. Some molecules use a dual process: fluid phase and adsorptive transcytosis. Specific transcytosis implies a receptor mediated process by which plasma molecules bind to specific binding sites or receptors localized on the cell uncoated pits or caveolae. The receptor mediated transcytosis has been identified for several molecular species such as LDL, transferrin, ceruloplasmin, insulin, and albumin.

Previous mathematical models has been developed to describe the mechanism of

receptor-mediated transcytosis (Gao *et al.*, 2005; Decuzzi and Ferrari, 2007). In contrast, the mechanism of nonspecific transcytosis remains unknown. It would be very interesting to study the mechanism of nonspecific adsorptive transcytosis and quantify the transport of charged or non-charged macrolecules and nanoparticles. Since the SGL and BM carry negative charges, the electrostatic interaction between them and charged molecules will favor the transport of cationic macrolecules across the BBB. One future study is to understand how the nonspecific adsorptive transcytosis of cationic macromolecules occurs and quantify their permeability across brain endothelium through mathematical modeling. The model prediction could be compared with the measured permeability of cationic drug carriers QAβCD nanoparticles across brain endothelial cell monolayer (Yuan *et al.*, 2010a). In this study, they found that permeability of the cell monolayer to these large nanoparticles (65-88 nm diameter) was comparable to that of dextran-4K (~2.8 nm diameter).

In the third part of this study, we have developed *in vitro* BBB models by using bEnd3 cell line monoculture, and coculturing of bEnd3 and primary rat astrocytes with two different types of basement membrane substitutes (Matrigel and Collagen I &IV mixture). The hydraulic conductivity, transendothelial electrical resistance and diffusive solute permeability of these models to various-sized solutes were quantified and expression of the BBB tight junction proteins in these *in vitro* models was assessed. Our results show that L_p and P of the endothelial monoculture and coculture models are not different from each other. Compared with *in vivo* permeability data from rat pial microvessels, P of the endothelial monoculture and coculture models are not significantly different from *in vivo* data for Dextran 70K, but they are 2-4 times higher for TAMRA

and Dextran 10K. This suggests that the endothelial monoculture and all of the coculture models are fairly good models for studying the transport of relatively large solutes across the BBB.

Nevertheless, our *in vitro* BBB models could be improved in several aspects. First, the endothelial cells we used in this study were immortalized cell line (bEnd3) and it is possible that these cells would lose some special features of the *in vivo* BBB. So primary cells should be employed in the future study. Second, endothelial cells and astrocytes could be obtained from the same species so that the interaction between these two types of cells could be enhanced. Third, the porous membrane in the Transwell filter separating the bEnd3 cells and the primary astrocytes is ~10 microns thick, thus the direct contact between the two cell types was missing in our coculture models. Fourth, since the endothelium *in vivo* is constantly exposed to the blood flow, coculture of endothelial cells with glial cells under a dynamic flow condition should better mimic the *in vivo* environment.

APPENDIX A

This appendix presents the two-dimensional model formation for the BBB, the numerical results for the two-dimensional model and the comparison between the two-dimensional and the simplified unidirectional model results for the resistance (or its reciprocal, the permeability) of the BBB.

A.1 Water Transport

Surface Glycocalyx Layer

The surface glycocalyx layer (SGL) is considered as a 2-D Darcy or Brinkman medium. The difference is that the Darcy flow does not satisfy the non-slip boundary condition at the endothelial cell surface ($x=-L-L_b$, $B < Z < W_a+B_a$), but the Brinkman flow does.

For the Darcy flow, the momentum equation is,

$$-\frac{\mu}{K_p}\bar{v}^{(f)} = \nabla p^{(f)} \tag{A1}$$

Here K_p is Darcy permeability in the SGL, μ is fluid viscosity, $p^{(f)}$ is pressure in the SGL, $\bar{v}^{(f)} = (u^{(f)}, 0, w^{(f)})$ is the velocity in the SGL, $u^{(f)}$ and $w^{(f)}$ are the x and z direction components of velocity, respectively. For an incompressible flow,

$$\nabla \cdot \bar{v}^{(f)} = 0 \tag{A2}$$

Put (A2) into (A1) gives

$$\frac{\partial^2 p^{(f)}}{\partial x^2} + \frac{\partial^2 p^{(f)}}{\partial z^2} = 0 \tag{A3}$$

For the Brinkman flow, the momentum equation is

$$\mu \nabla^2 \bar{v}^{(f)} - \frac{\mu}{K_p} \bar{v}^{(f)} - \nabla p^{(f)} = 0 \tag{A4}$$

The boundary conditions for Eqs. (A2), (A3) and (A4) are as following. In the vessel lumen, the pressure is a constant,

$$p^{(f)} = p_L \qquad \text{at } x = -L - L_b - L_f \text{ and } 0 < z < W_a + B_a \tag{A5}$$

At the horizontal centerline and upper horizontal boundaries of the SGL, symmetric conditions give,

$$\frac{\partial p^{(f)}}{\partial z} = 0 \qquad \text{at} \quad z = 0 \text{ and } z = W_a + B_a,\ -L - L_b - L_f < x < -L - L_b \tag{A6}$$

At the luminal surface of endothelial cells, impermeable condition is applied,

$$u^{(f)} = 0 \text{ at } x = -L - L_b,\ B < z < W_a + B_a \tag{A7}$$

For the Brinkman flow, non-slip boundary condition is also applied at the luminal surface of endothelial cells,

$$w^{(f)} = 0 \quad \text{at} \quad x = -L - L_b,\ B < z < W_a + B_a \tag{A8}$$

At the entrance to the inter-endothelial cleft, continuous boundary conditions are satisfied,

$$p^{(f)} = p^{(1)},\ u^{(f)} = u^{(1)} \text{ at } x = -L - L_b,\ 0 < z < B \tag{A9}$$

Here $p^{(1)}$ and $u^{(1)}$ are the pressure and velocity in x-dir in region 1 of the inter-endothelial cleft (see **Fig. 2.2**).

Inter-endothelial Cleft

In the inter-endothelial cleft, the flow is considered as incompressible viscous flow and the governing equations are

$$\nabla \cdot \bar{v}^{(i)} = 0 \qquad \text{i=1,2,3} \tag{A10}$$

$$-\nabla p^{(i)} + \mu \nabla^2 \bar{v}^{(i)} = 0 \qquad \text{i=1,2,3} \tag{A11}$$

Here $\bar{v}^{(i)} = (u^{(i)}, v^{(i)}, w^{(i)})$ and $p^{(i)}$ are the velocity and pressure in regions 1, 2, 3 of the interendothelial cleft. $u^{(i)}, v^{(i)}, w^{(i)}$ are the *x, y* and *z* direction components of the velocity. $B_{(i)}$= B when i = 1, 3; $B_{(i)} = B_s$ when i = 2.

Since the height of the cleft 2B is much smaller, compared to both the length of the blood vessel L_v and the depth L of the cleft, the water flow in the cleft can be approximated by a Hele-Shaw channel flow (Fu et al., 1994),

$$\bar{v}^{(i)}(x, y, z) = \bar{v}^{(i)}(x, y)(1 - \frac{z^2}{B_{(i)}^{\ 2}}) \qquad \text{i=1, 3} \tag{A12}$$

which satisfies non-slip condition at z=B and symmetric condition at z=0. $\bar{v}^{(i)}(x, y) = (u_0^{\ (i)}, v_0^{\ (i)})$ is the velocity at the center line z=0, which satisfies

$$\bar{v}_0^{\ (i)} = -\frac{B_{(i)}^{\ 2}}{2\mu} \nabla p^{(i)} \qquad \text{i=1, 3} \tag{A13}$$

$$\bar{v}^{(i)}(x, y, z) = -\frac{B_{(i)}^{\ 2}}{2\mu} \nabla p^{(i)} (1 - \frac{z^2}{B_{(i)}^{\ 2}})$$

Along the tight junction in the interendothelial cleft of the BBB, there is a continuous small slit in the y direction but no large discontinuous pores as in the mesenteric microvessel (Fu et al., 1994), thus the flow in the cleft is unidirectional, $\bar{v}_0^{\ (i)}(x) = (u_0^{\ (i)}(x), 0)$. Put this into *Eq.(A13),*

$$u_0^{\ (i)} = -\frac{B_{(i)}^{\ 2}}{2\mu} \frac{dp^{(i)}}{dx} \qquad \text{i=1, 3} \tag{A14}$$

Eq. (A10) into (A14) gives,

$$\frac{d^2 p^{(i)}}{dx^2}=0 \qquad \text{i=1, 3} \tag{A15}$$

Integration of Eq. (A15) gives,

$$\frac{dp^{(i)}}{dx} = a_i \qquad \text{i=1, 3} \tag{A16}$$

a_i are constants. (A16) into (A14) and (A12) gives,

$$u^{(i)}(z) = -\frac{B_{(i)}{}^2}{2\mu} a_i \left(1-\frac{z^2}{B_{(i)}{}^2}\right) \qquad \text{i=1,2,3} \tag{A17}$$

Eq. (A17) indicates that the flow in the cleft is the Poiseuille channel flow. In (A17), we also included the Poiseuille flow in region 2 (the small slit in the tight junction) of the cleft. Continuous boundary conditions for the pressure and flow rate are satisfied at interfaces between regions of the inter-endothelial cleft,

$$p^{(1)} = p^{(2)}, \; B^3 \frac{\partial p^{(1)}}{\partial x} = B_s{}^3 \frac{\partial p^{(2)}}{\partial x} \text{ at } x = -L - L_b + L_1, \; 0 < z < B_s \tag{A18}$$

$$p^{(2)} = p^{(3)}, \; B_s{}^3 \frac{\partial p^{(2)}}{\partial x} = B^3 \frac{\partial p^{(3)}}{\partial x} \text{ at } x = -L - L_b + L_1 + L_{jun}, \; 0 < z < B_s \tag{A19}$$

Basement Membrane

The basement membrane (BM) is considered as the Brinkman medium and the governing equations are

$$\nabla \cdot \bar{v}^{(4)} = 0 \tag{A20}$$

$$\mu \nabla^2 \bar{v}^{(4)} - \frac{\mu}{K_b} \bar{v}^{(4)} - \nabla p^{(4)} = 0 \tag{A21}$$

Here $\bar{v}^{(4)}(x,z) = (u^{(4)}(x,z), 0, w^{(4)}(x,z))$ and $p^{(4)}$ are the velocity and pressure in the BM, and K_b is the Darcy permeability in the BM.

At the interface of the inter-endothelial cleft and BM, continuity in the pressure and velocity gives,

$$p^{(3)} = p^{(4)}, \; -\frac{B^3}{2\mu}\frac{\partial p^{(3)}}{\partial x}\left(1-\frac{z^2}{B^2}\right) = u^{(4)} \quad \text{at } x = -L_b, \; 0 < z < B \tag{A22}$$

At the abluminal side of the endothelial cell surface and at the luminal side of astrocyte foot processes, impermeable and non-slip boundary conditions give,

$$u^{(4)} = w^{(4)} = 0 \quad \text{at} \quad x = -L_b, \; B < z < W_a + B_a \tag{A23}$$

$$u^{(4)} = w^{(4)} = 0 \quad \text{at} \quad x = L_b, \; 0 < z < W_a \tag{A24}$$

At the horizontal centerline and upper horizontal boundaries of BM, symmetric condition gives:

$$\frac{\partial p^{(4)}}{\partial z} = 0 \text{ at } z = 0 \text{ and } z = W_a + B_a, \; -L_b < x < L_b \tag{A25}$$

At the interface of the BM and the cleft between astrocyte foot processes, continuity in the pressure and the velocity gives,

$$p^{(4)} = p^{(5)}, \; u^{(4)} = u^{(5)} \quad \text{at } x = L_b, \; W_a < z < W_a + B_a \tag{A26}$$

Here $p^{(5)}$ and $u^{(5)}$ are the pressure and the x-dir velocity in the cleft between astrocyte foot processes.

Cleft between Astrocyte Foot Processes

The flow in the cleft between astrocyte foot processes is an incompressible viscous flow and the governing equations are

$$\nabla \cdot \bar{v}^{(5)} = 0 \tag{A27}$$

$$-\nabla p^{(5)} + \mu \nabla^2 \bar{v}^{(5)} = 0 \tag{A28}$$

Here $\bar{v}^{(5)} = (u^{(5)}, 0, w^{(5)})$ is the velocity in the cleft between astrocyte foot processes. Similar

to the interendothelial cleft, flow in the cleft between astrocyte foot processes can also be approximated as the Poiseuille flow since the height of the cleft $2B_a$ is small compared to both the length of the blood vessel L_v and the width L_a of the astrocyte foot processes. So the velocity in the interendothelial cleft can be expressed as,

$$u^{(5)} = u_0^{(5)}[1 - \frac{(z - W_a - B_a)^2}{B_a{}^2}] \tag{A29}$$

which satisfies non-slip condition at $z=W_a$ and symmetric condition at $z=W_a+B_a$. Here $u_0^{(5)}$ is the velocity in the center line $z=W_a+B_a$,

$$u_0^{(5)} = -\frac{B_a{}^2}{2\mu}\frac{\partial p^{(5)}}{\partial x} \tag{A30}$$

Eq. (A27) into (A30) gives,

$$\frac{d^2 p^{(5)}}{dx^2} = 0 \tag{A31}$$

Integration of (A31) gives,

$$\frac{dp^{(5)}}{dx} = a_5 \tag{A32}$$

a_5 is a constant. At the cleft exit, the pressure in the tissue is assumed to be constant,

$$p^{(5)} = p_A \quad \text{at } x = L_a + L_b,\ W_a < z < W_a + B_a \tag{A33}$$

The pressures and velocities in all regions of the BBB were calculated simultaneously with corresponding boundary conditions using a numerical method similar to that in Fu and Chen (2003) and Hu and Weinbaum (1999). The convergence was satisfied when the relative error between the n^{th} and $(n+1)^{th}$ iteration for p and u, w at each point, $|[p_{(n+1)}-p_{(n)}]/ p_{(n+1)}|$, $|[u_{(n+1)}-u_{(n)}]/ u_{(n+1)}|$, $|[w_{(n+1)}-w_{(n)}]/ w_{(n+1)}|$ were less than

10^{-7}.

The hydraulic conductivity is defined as

$$L_p = \frac{Q^f{}_{2D}}{p_L - p_A}\frac{L_{jt}}{L_v} \tag{A34}$$

where p_L and $p_{A,}$ are constant pressures in the vessel lumen and in the tissue space, respectively. L_{jt} is the total length of the cleft per unit surface area of the microvessel wall. Q^f_{2D} (see **Fig. A1**) is the 2-D volume flow rate through the BBB with a length of L_v in the y direction

$$Q^f_{2D} = 2L_v\int_0^{W_a+B_a} \mathrm{u^{(f)}}(\text{-L - L}_\text{b}\text{ - L}_\text{f}\text{, z})\mathrm{dz} \tag{A35}$$

If we neglected the 2D effect at the entrance/exit regions of the clefts and the BM, and considered a unidirectional Darcy flow in the SGL, the 1-D volume flow rate Q^f_{1D} (see **Fig. A1**), which was used to approximate $\mathrm{Q^f_{2D}}$ in (A35), is,

$$Q^f_{1D} = \frac{(p_L - p_A)L_v}{\mu L_f/(2K_pB) + 3\mu L_1/(2B^3) + 3\mu L_{jun}/(2B_s^3) + 3\mu(L - L_1 - L_{jun})/(2B^3) + \mu W_a/\{4K_b[L_b - \sqrt{K_b}\tanh(L_b/\sqrt{K_b})]\} + 3\mu L_a/(2B_a^3)}$$

Q^f_{1D} was used as Q_L in Eq. (7a) of Chapter 2 of the main text to calculate the hydraulic conductivity $\mathrm{L_p}$.

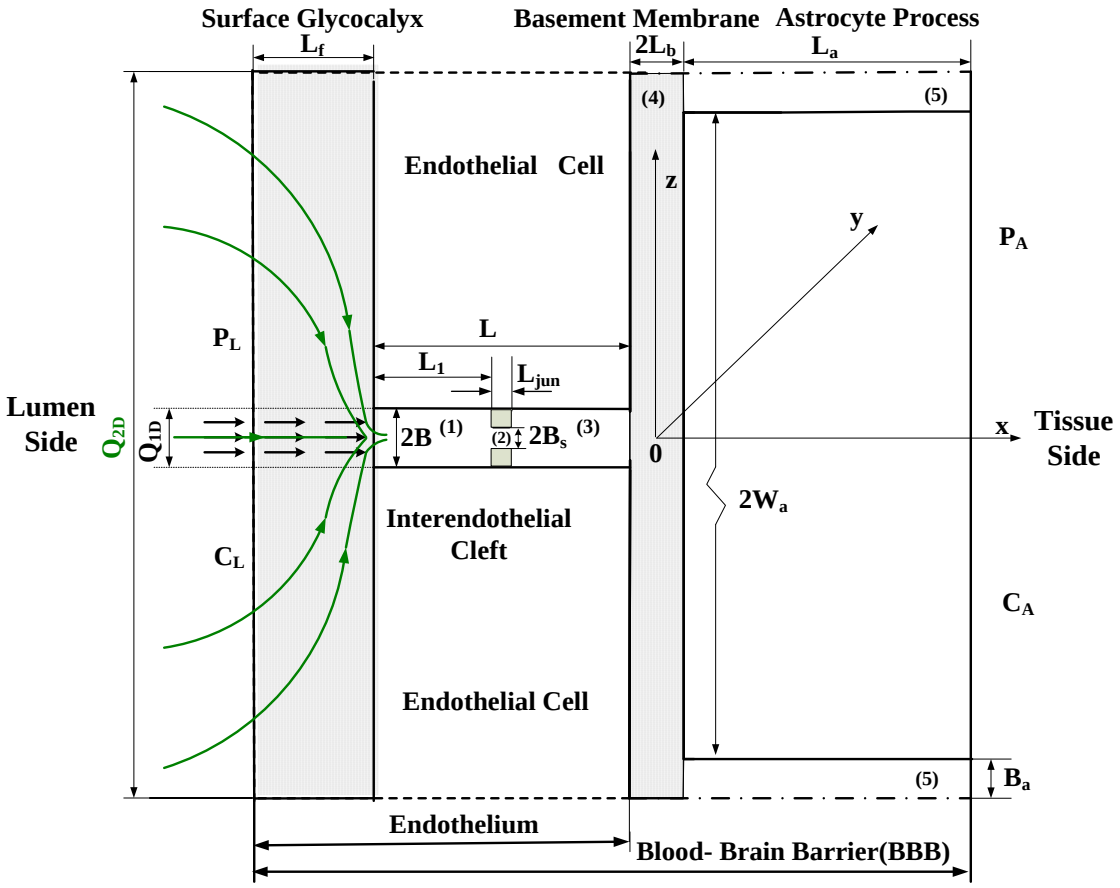

Figure A1 The sketch showing the 2-D (green arrows) and 1-D (black arrows) flows in the SGL.

In **Fig. A2**, we plotted the pressure contours and velocity vectors at the entrance to the interendothelial cleft from the SGL when employing the Darcy flow model (**Fig. A2(a)**) or the Brinkman flow model (**Fig. A2(b)**), at the entrance to the BM from the interendothelial cleft (**Fig. A2(c)**), and at the exit of the BM to the cleft between astrocyte foot processes (**Fig. A2(d)**). We can see from **Fig. A2.2** that the 2-D effects only reside the small entrance/exit regions, which account for less than 1% of the total area in the corresponding regions.

(a)

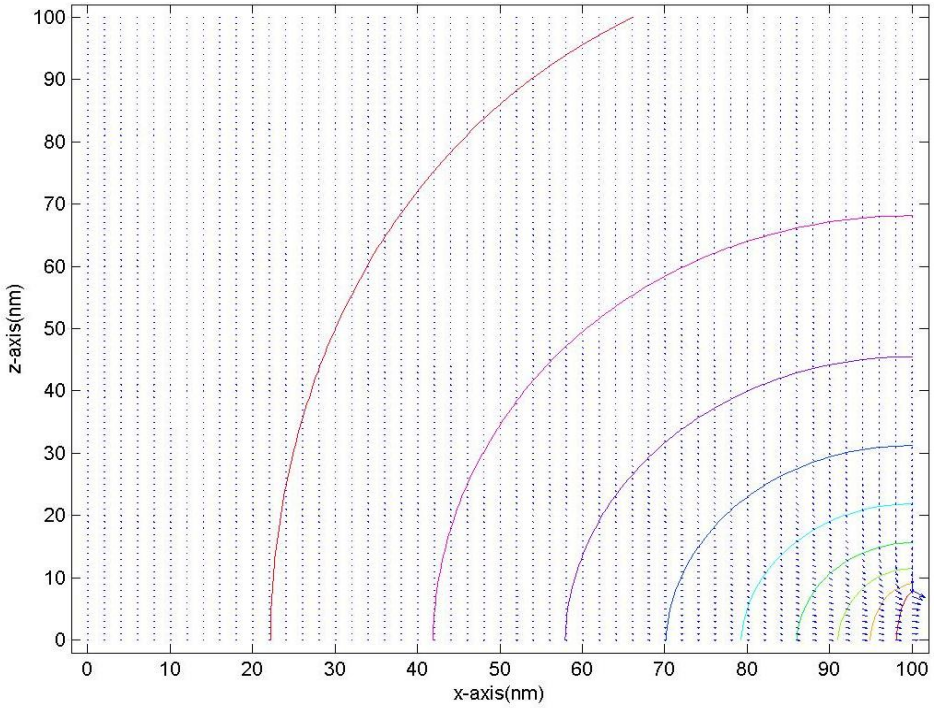
z-axis(nm)
x-axis(nm)
0
10
20
30
40
50
60
70
80
90
100

(b)

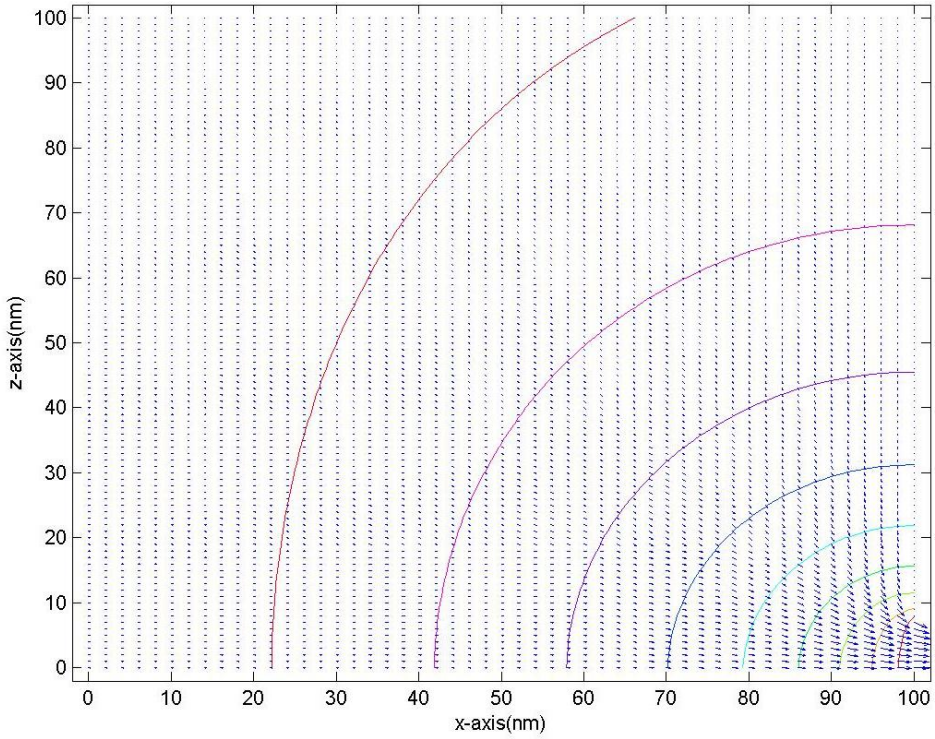
z-axis(nm)
x-axis(nm)
0
10
20
30
40
50
60
70
80
90
100

(c)

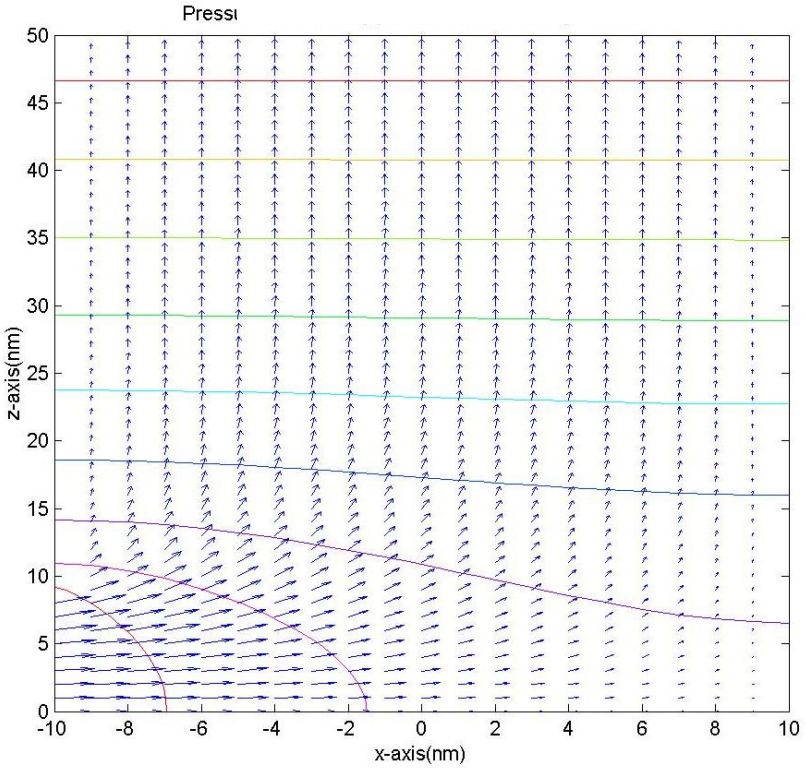

(d)

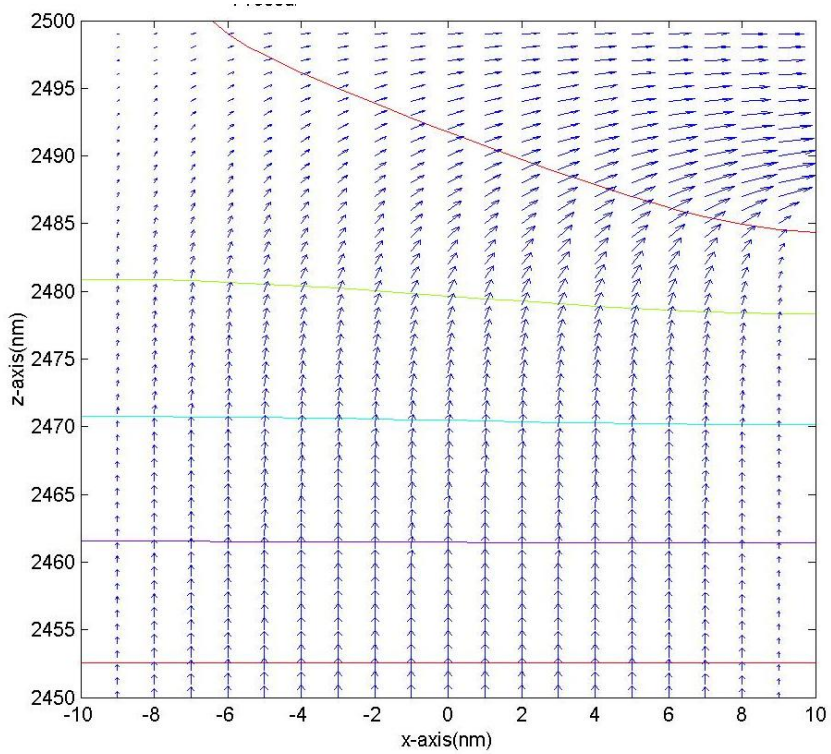

Figure A2 The velocity (arrows) and pressure (contour lines) profiles near the entrance region to the interendothelial cleft from the SGL ($0 \leq z \leq 9$ nm is the half entrance region) when using **(a)** the Darcy flow or **(b)** the Brinkman flow in the SGL; their profiles near **(c)** the entrance region to the BM from the interendothelial cleft ($0 \leq z \leq 9$ nm is the half

entrance region) and **(d)** the exit region of the BM to the cleft between astrocyte processes ($0 \le z \le 15$ nm is the half exit region).

In **Fig. A3**, we compared the resistance of the BBB to water (the reciprocal is L_p) R^f_{2D} calculated using Q^f_{2D} from the 2-D model and the resistance R^f_{1D} using Q^f_{1D} from the approximate unidirectional model. Our results (solid line in **Fig. A3**) show that using Q^f_{1D} would overestimate the BBB resistance to water by less than 5% in our case by employing either the Darcy or the Brinkman medium model for the SGL. The difference in the SGL resistance between the result from the Darcy medium model and that from the Brinkman medium model is less than 0.3%. However, almost all the discrepancy is due to neglecting the 2D effect at the entrance to the interendothelial cleft from the SGL. We show the underestimation in L_p by neglecting this 2D effect in the solid line of **Fig. 2.8**.

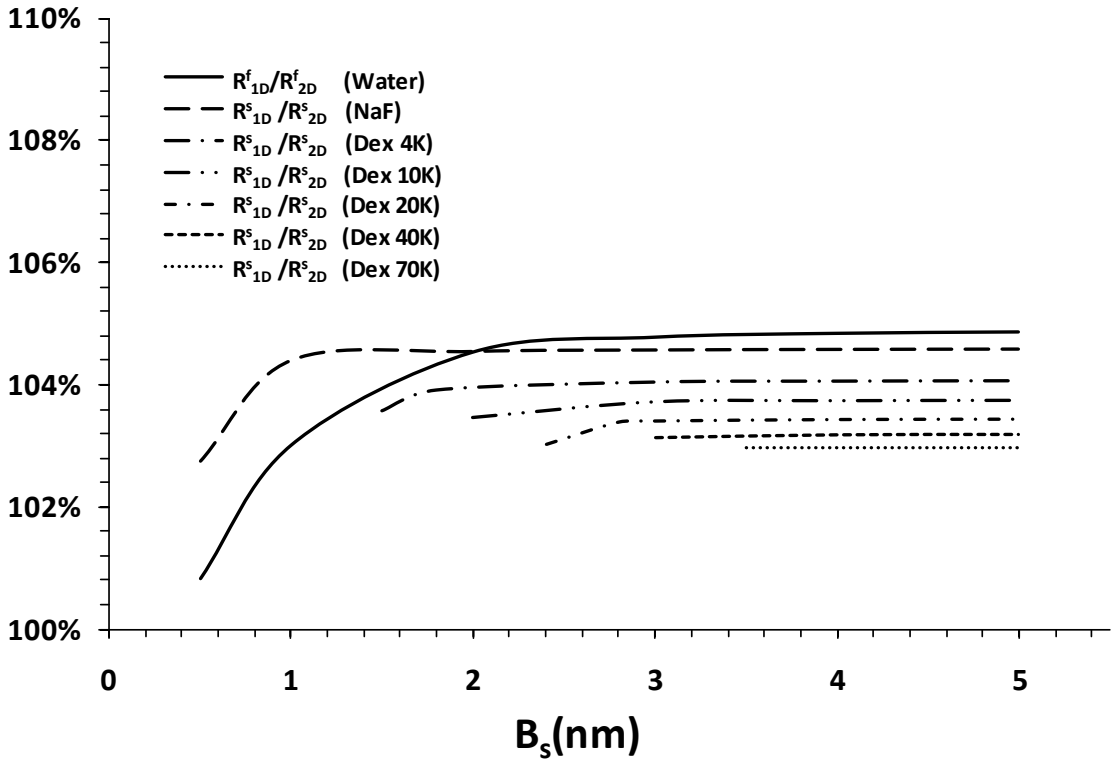

Figure A3 The ratio of the resistances of the BBB to water and to solutes from the 1-D model to those from the 2-D model as a function of B_s, the half width of the small slit in the junction strand.

A.2 Solute Transport

To calculate the diffusive solute permeability P of the BBB, which is defined as the solute flow rate per unit vessel surface area divided by the concentration difference across the BBB, we need to solve the following 2-D diffusion equation for the solute transport in each region of the BBB,

$$\frac{\partial^2 C^{(i)}}{\partial x^2} + \frac{\partial^2 C^{(i)}}{\partial z^2} = 0 \tag{A36}$$

Here $C^{(i)}(x, z)$ are the solute concentration in the SGL (i=f), in the inter-endothelial clefts (i=1,2,3), in the BM (i=4), and in the cleft between astrocyte foot processes (i=5) . The

corresponding boundary conditions are shown below.

Surface Glycocalyx Layer

The concentration in the lumen of microvessel is assumed to be constant,

$$C^{(f)} = C_L \quad \text{at} \quad x = -L - L_b - L_f \text{ and } 0 < z < W_a + B_a \tag{A37}$$

At the horizontal centerline and upper horizontal boundary of the SGL, symmetric condition gives,

$$\frac{\partial C^{(f)}}{\partial z} = 0 \quad \text{at} \quad z = 0 \text{ and } z = W_a + B_a,\ -L - L_b - L_f < x < -L - L_b \tag{A38}$$

The impermeable condition is used at the luminal surface of endothelial cells,

$$\frac{\partial C^{(f)}}{\partial x} = 0 \quad \text{at} \quad x = -L - L_b,\ B < z < W_a + B_a \tag{A39}$$

At the interface of the SGL and inter-endothelial cleft, continuity in concentration and flux gives,

$$C^{(f)} = C^{(1)},\ D_s^f \frac{\partial C^{(f)}}{\partial x} = D_s^c \frac{\partial C^{(1)}}{\partial x} \quad \text{at } x = -L - L_b,\ 0 < z < B \tag{A40}$$

where $D_s{}^f$ and $D_s{}^c$ are effective solute diffusion coefficients in the SGL and in the wide part of the inter-endothelial cleft, respectively.

Interendothelial Cleft

Continuity in the concentration and solute flux at the interface between regions of interendothelial cleft gives,

$$C^{(1)} = C^{(2)},\ D_s^c \frac{\partial C^{(1)}}{\partial x} = D_s^{sl} \frac{\partial C^{(2)}}{\partial x} \quad \text{at } x = -L - L_b + L_1,\ 0 < z < B_s \tag{A41}$$

$$C^{(2)} = C^{(3)},\ D_s^{sl}\frac{\partial C^{(2)}}{\partial x} = D_s^{c}\frac{\partial C^{(3)}}{\partial x} \text{ at } x = -L - L_b + L_1 + L_{jun},\ 0 < z < B_s \tag{A42}$$

where D_s^{sl} is the effective solute diffusion coefficient in the continuous small silt of the junction strand.

At the horizontal centerline symmetric boundary condition gives,

$$\frac{\partial C^{(i)}}{\partial z} = 0 \text{ at } z = 0,\ -L - L_b < x < -L_b,\ i=1,2,3 \tag{A43}$$

The tight junction wall is impermeable,

$$\frac{\partial C^{(1)}}{\partial x} = 0 \text{ at } x = -L - L_b + L_1,\ B_s < z < B + B_s \tag{A44}$$

$$\frac{\partial C^{(3)}}{\partial x} = 0 \text{ at } x = -L - L_b + L_1 + L_{jun},\ B_s < z < B + B_s \tag{A45}$$

Basement Membrane

At the interface of the interendothelial cleft and the BM, continuity in concentration and flux gives,

$$C^{(3)} = C^{(4)},\ D_s^{c}\frac{\partial C^{(3)}}{\partial x} = D_s^{b}\frac{\partial C^{(4)}}{\partial x} \text{ at } x = -L_b,\ 0 < z < B \tag{A46}$$

where D_s^{b} is the effective solute diffusion coefficient in the BM.

The abluminal side of endothelial cells and the luminal side of astrocyte foot processes are impermeable,

$$\frac{\partial C^{(4)}}{\partial x} = 0 \text{ at } x = -L_b,\ B < z < W_a + B_a \tag{A47}$$

$$\frac{\partial C^{(4)}}{\partial x} = 0 \text{ at } x = L_b,\ 0 < z < W_a \tag{A48}$$

At the horizontal centerline and upper horizontal boundary of the BM, symmetric condition gives:

$$\frac{\partial C^{(4)}}{\partial z} = 0 \text{ at } z = 0 \text{ and } z = W_a + B_a,\ -L_b < x < L_b \tag{A49}$$

At the interface of the BM and the cleft between astrocyte foot processes, continuity in the concentration and flux gives,

$$C^{(4)} = C^{(5)},\ D_s^b \frac{\partial C^{(4)}}{\partial x} = D_s^a \frac{\partial C^{(5)}}{\partial x} \text{ at } x = L_b,\ W_a < z < W_a + B_a \tag{A50}$$

where D_s^a is the effective solute diffusion coefficient in cleft between astrocyte foot processes.

Cleft between Astrocyte Foot Processes

The wall of the astrocytes processes is impermeable,

$$\frac{\partial C^{(5)}}{\partial z} = 0 \quad \text{at} \quad z = W_a,\ L_b < x < L_a + L_b \tag{A51}$$

At the horizontal centerline of the astrocyte cleft, symmetric boundary condition gives,

$$\frac{\partial C^{(5)}}{\partial z} = 0 \quad \text{at} \quad z = W_a + B_a,\ L_b < x < L_a + L_b \tag{A52}$$

The concentration at the tissue side is a constant,

$$C^{(5)} = C_A \text{ at } x = L_a + L_b, W_a < z < W_a + B_a \tag{A53}$$

The concentrations in the BBB were solved with corresponding boundary conditions using the numerical method similar to that in Fu and Chen (2003) and Hu and Weinbaum (1999). The convergence was satisfied when the relative error between the n^{th} and $(n+1)^{th}$ iteration for C, $|[C_{(n+1)}-C_{(n)}]/ C_{(n+1)}|$ was less than 10^{-7}.

Finally, the diffusive solute permeability P was calculated as,

$$P = \frac{Q^{s}{}_{2D}}{C_L - C_A}\frac{L_{jt}}{L_v} \tag{A54}$$

where C_L and C_A are concentrations in the vessel lumen and in the tissue space, respectively. L_{jt} is the total length of the cleft per unit surface area of the microvessel wall. The 2-D solute flow rate Q^{s}_{2D} (see **Fig. A1**) was obtained by integrating the flux at the entrance of SGL within a length of L_v in the y-direction,

$$Q^{s}_{2D} = 2L_v\int_0^{W_a+B_a} D^{f}_{s}\frac{\partial C^{(f)}}{\partial x}\mathrm{dz} \tag{A55}$$

When neglecting the 2D effect in the entrance/exit regions of the SGL, the cleft and the BM, the unidirectional solute flux through the SGL entrance with a length of L_v in the y-direction could be expressed as

$$Q^{s}_{1D} = \frac{(C_L - C_A)L_v}{L_f/(2BD^{f}_{s}) + L_1/(2BD^{c}_{s}) + L_{jun}/(2B_sD^{sl}_{s}) + (L - L_1 - L_{jun})/(2BD^{c}_{s}) + W_a/(4L_bD^{b}_{s}) + L_a/(2B_aD^{a}_{s})}$$

Q^{s}_{1D} was used as Q^{s}_{L} in Eq. (9) of the main text to calculate the diffusive solute permeability P.

As in the pressure and velocity distributions, the 2-D concentration and the solute flux distributions are restricted in small entrance/exit regions of the clefts and the BM, which account for less than 1% of the total area of the corresponding regions (not shown here). In **Fig. A3**, we compared the resistance of the BBB to various-sized solutes (the reciprocal is P) $R^{s}{}_{2D}$ calculated using Q^{s}_{2D} from the 2-D model and the resistance $R^{s}{}_{1D}$ using Q^{s}_{1D} from the approximate unidirectional model. Our results shown in **Fig. A3**

indicate that using Q_{1D}^{s} would overestimate the BBB resistance to solutes by less than 2% for all the solutes in our study. As for the resistance to water, almost all the discrepancy is due to neglecting the 2D effect at the entrance to the interendothelial cleft from the SGL. We show the underestimation in P to a variety of solutes by neglecting this 2D effect in **Fig. 2.8**.

APPENDIX B

This appendix describes the detailed mathematical formation of the electro-diffusion model for charged solutes transport across the BBB. The results for ion concentration and dimensionless electric potential profile are also presented.

B.1 Mathematical Formation

Surface glycocalyx layer

As shown in Figs. 3.1 and 3.2, the SGL covers the entire luminal surface of endothelium. In the microvessel lumen, the solution consists of monovalent cations (C_+) and monovalent anions(C_-), the test solutes (FITC-ribonuclease and FITC-α-lactalbumin) as well as a small amount of proteins (e.g., albumin). Under the assumption of dilute solution, the solute flux of species i could be expressed as following by modified Nernst-Plank equation considering the contributions from diffusion, ion migration and convection, (Deen *et al.*, 1980; Chen and Fu, 2004; Chen and Fu, 2009),

$$\boldsymbol{J}_{i,f} = -D_{i,f}\left(\nabla C'_{i,f} + Z^i C'_{i,f} \nabla \psi'_f\right) + K_{i,f} J_v C'_{i,f} \qquad \mathrm{i} = +, -, \mathrm{TS} \tag{B1}$$

Where $C'_{i,f}$ and $D_{i,f}$ are concentrations and effective diffusion coefficients of positive ($i = +$), negative ions ($i = -$), and test solutes (i=TS) within the SGL. $\psi'_f = FE_f/RT$ is the dimensionless electrical potential in the SGL, E_f is the electrical potential in the SGL, R is the universal gas constant, F is Faraday's constant, T is the absolute temperature. Z^i is the molecular charge number of species i, J_v is the fluid flux across microvessel wall, $K_{i,f}$ is the hindrance factor or retardation coefficient of species i in the SGL. $K_{i,f}$ is ~0.65 for the test solutes (FITC-ribonuclease and FITC-α-lactalbumin), ~0.98 for ions (mainly Na^+ and Cl^-) (Chen and Fu, 2004).

Since the blood-brain barrier has very low hydraulic conductivity L_p, $L_p \sim 2.0 \times$

10^{-9}cm/s/cmH_2O, which was measured in pial microvessels (Fraser *et al.*, 1990), the effective filtration pressure (including both hydrostatic and oncotic pressure differences) across the microvessel wall Δp_{eff} ~ 5 cmH_2O (Mayhan and Heistad, 1986; Yuan *et al.*, 2009), the Peclet number in the SGL $Pe_f = K_{i,f} J_v L_f/D_{i,f} = K_{i,f} L_p \Delta p_{eff} (\pi D_v/2B) L_f/D_{i,f}$ ~ O(10^{-3}) for the test solutes and ~O(10^{-4}) for ions (see parameter values in Tables). Therefore, we can neglect the convective contribution due to fluid filtration in the solute flux, Eq. A1 can be simplified as

$$J_{i,f} = -D_{i,f}\left(\nabla C'_{i,f} + Z^i C'_{i,f} \nabla \psi'_f\right) \quad \text{i} = +, -, \text{TS} \tag{B2}$$

Ion Transport. The overall electro-neutrality is assumed to be satisfied in the SGL(Deen *et al.*, 1980; Fu *et al.*, 2003; Chen and Fu, 2004; Chen and Fu, 2009),

$$\sum_i Z^i C'_{i,f} - C_{mf} = 0 \qquad i = +, -, TS \tag{B3}$$

Here, $C'_{i,f}$ is the concentration of positive (i=+) and negative (i=-) ions and charged test solutes in the SGL, Z^i is the corresponding electrical valence of ions and charged molecules, C_{mf} is charge density of the SGL. Equation B3 indicates that the fixed negative charge carried by the SGL must be balanced by an excess of mobile positive ions.

In the *in vivo* experiments, the concentration of test solutes is 1mg/ml(Yuan *et al.*, 2010). For ribonuclease, $Z^{rib} C'_{rib,f}$ ~ (+4)×7×10^{-2}mM = 0.28 mM. For α-lactalbumin, $Z^{alpha} C'_{alpha,f}$ = (-10)×7×10^{-2}mM = -0.7mM. Compared with ion concentrations C'_+ and C'_-, which is in the order of 100mM, the concentration of test solutes in Eq. B3 can be neglected. In addition, the concentration of charged macromolecules (albumin) is also negligible compared with the concentration of ions. So Eq. A3 reduces to the balance between monovalent cations ($Z^+ = 1$ for Na^+) and the summation of monovalent anions

($Z^- = -1$ for Cl^-) and negative charges of the SGL,

$$C'_{+,f} = C'_{-,f} + C_{mf} \tag{B4}$$

At the interface between the SGL and the lumen ($x = -L_f - L_b - L$), the Donnan equilibrium is satisfied. This gives

$$\psi_f - \psi'_f = \ln\left[\frac{C'_{+,f}}{C_+}\right] = \ln\left[\frac{C_-}{C'_{-,f}}\right] \tag{B5}$$

Here C_+ and C_- are the concentration of cation and anion in the vessel lumen which equals to a constant of 140 mM under physiological conditions.

Combining Eqs. B4 and B5 gives,

$$C'_{+,f} = \frac{C_{mf} + \sqrt{C_{mf}^2 + 4C_+C_-}}{2} \quad x = -L_f - L_b - L \tag{B6}$$

The condition for no electrical current flows across the SGL is

$$\sum_i Z^i J_{i,f} = 0\,, \quad i = +, -, TS \tag{B7}$$

Neglecting the current due to charged test solutes(Fu *et al.*, 2003; Chen and Fu, 2004), Eq. B7 reduces to

$$J_{+,f} = J_{-,f} \tag{B8}$$

The solute fluxes of monovalent ions are as following according to Eq. A2,

$$J_{+,f} = -D_{+,f}\left(\frac{dC'_{+,f}}{dx} + C'_{+,f}\frac{d\psi'_f}{dx}\right) \tag{B9}$$

$$J_{-,f} = -D_{-,f}\left(\frac{dC'_{-,f}}{dx} - C'_{-,f}\frac{d\psi'_f}{dx}\right) \tag{B10}$$

The condition of electroneutrality (Eq. B4) and zero current flow (Eq. B8) can be used to eliminate $C'_{-,f}$ and $J_{-,f}$ from Eqs. B9 and B10, so that

$$\frac{dC'_{+,f}}{dx} = \frac{-J_{+,f}\left[C'_{+,f}D_{+,f} + \left(C'_{+,f} - C_{mf}\right)D_{-,f}\right] + D_{+,f}D_{-,f}C'_{+,f}\frac{dC_{mf}}{dx}}{D_{+,f}D_{-,f}(2C'_{+,f} - C_{mf})} \tag{B11}$$

$$\frac{d\psi_f'}{dx} = \frac{J_{+,f}(D_{+,f}-D_{-,f})-D_{+,f}D_{-,f}\frac{dC_{mf}}{dx}}{D_{+,f}D_{-,f}(2C_{+,f}'-C_{mf})} \tag{B12}$$

In our model, charge density C_{mf} in the SGL is considered to be constant (see Model Description in main text) so $\frac{dC_{mf}}{dx} = 0$ and the above equations can be simplified as

$$\frac{dC_{+,f}'}{dx} = \frac{-J_{+,f}\left[C_{+,f}'D_{+,f}+\left(C_{+,f}'-C_{mf}\right)D_{-,f}\right]}{D_{+,f}D_{-,f}(2C_{+,f}'-C_{mf})} \tag{B13}$$

$$\frac{d\psi_f'}{dx} = \frac{J_{+,f}(D_{+,f}-D_{-,f})}{D_{+,f}D_{-,f}(2C_{+,f}'-C_{mf})} \tag{B14}$$

Eqs. B13 and B14 were integrated with initial values of $C_{+,f}^{'}$ and $\psi_{+,f}^{'}$ at $x = -L_f - L_b - L$ calculated from Eqs. B5 and B6,

$$C_{mf}(D_{-,f}-D_{+,f})\ln[\frac{(D_{-,f}+D_{+,f})C_{+,f}^{'}(x)-C_{mf}D_{-,f}}{(D_{-,f}+D_{+,f})C_{+,f}^{'}(-L_f-L_b-L)-C_{mf}D_{-,f}}] =$$

$$-2(D_{-,f}+D_{+,f})\,[C_{+,f}^{'}(x)-C_{+,f}^{'}(-L_f-L_b-L)]-\frac{J_{+,f}}{D_{+,f}D_{-,f}}(D_{-,f}+D_{+,f})^2(x+L_f+L_b+L) \tag{B15}$$

Test solute transport. Under steady state, the conservation of mass relation for test solutes (FITC-ribonuclease or FITC-α-lactalbumin) gives

$$\nabla\cdot[J_{i,f}] = 0 \qquad\qquad i = TS \tag{B16}$$

In the SGL, a 1-D transport is assumed(Fu *et al.*, 2003; Chen and Fu, 2004; Li *et al.*, 2010), Eq. B16 becomes,

$$\frac{d}{dx}\left[-D_{i,f}\left(\frac{dC_{i,f}^{'}}{dx}+Z^iC_{i,f}^{'}\frac{d\psi_f^{'}}{dx}\right)\right] = 0 \quad i = \text{TS} \tag{B17}$$

$$or \qquad \frac{dC_{i,f}^{'}}{dx}+C_{i,f}^{'}\left(Z^i\frac{d\psi_f^{'}}{dx}\right) = A \qquad i = \text{TS} \tag{B18}$$

Here A is a constant. We define

$$Pe_{charge} = L_f Z^i \frac{d\psi'_f}{dx} \tag{B19}$$

as a measure of the relative importance of ion migration and diffusion to transport of a charged solute. As a result, Eq. A18 can be expressed as:

$$\frac{dC'_{i,f}}{dx} + Pe_{charge} \frac{C'_{i,f}}{L_f} = A \qquad i = TS \tag{B20}$$

At the interface of the SGL and the inter-endothelial cleft, continuous solute flux is satisfied,

$$D_{i,f}\left[\frac{dC'_{i,f}}{dx} + Pe_{charge} \frac{C'_{i,f}}{L_f}\right] = D_{i,c} \frac{\partial C_i^{(1)}}{\partial x} \quad i = TS \qquad \text{at} \quad x = -L - L_b \tag{B21}$$

In Eq. B21, $C_i^{(1)}$ is the solute concentration in *region 1* of the inter-endothelial cleft ($-L-L_b < x < -L-L_b+L_1$).

As in previous models, there is a Donnan equilibrium relationship between the solute concentration $C'_{i,f}$ in the SGL and that at the lumen or the inter-endothelial cleft side $C_i(x,z)$

$$C'_{i,f} = C_{i,f} e^{[Z^i(\psi_f - \psi'_f)]} \qquad at\ x = -L - L_b - L_f \tag{B22}$$

$$C'_{i,f} = C_{i,f} e^{[Z^i(\psi^{(1)} - \psi'_f)]} \qquad at\ x = -L - L_b \tag{B23}$$

where ψ'_f and ψ_f are the dimensionless electrical potential inside and outside the SGL. At the microvessel lumen, $\psi_f(-L - L_b - L_f) = 0$, which is the reference potential. Here $\psi^{(1)}(x)$ is the dimensionless electric potential in the first region of the inter-endothelial cleft (see **Fig. 3.2**)

The solution of Eq. B20 which satisfies corresponding boundary conditions was obtained as,

$$C'_{i,f} = e^{-Z^i \psi'_f(x)}(C_{iL} + A\int_{-L-L_b-L_f}^{x} e^{Z^i \psi'_f(x)} dx) \quad i = TS \quad -L - L_b - L_f < x < -L - L_b \tag{B24}$$

$$A = \frac{C_i^{(1)}(-L-L_b, z)e^{Z^i\psi_f(-L-L_b)} - C_{iL}}{\int_{-L-L_b-L_f}^{-L-L_b} e^{Z^i\psi_f'(x)}dx}$$

Here C_{iL} is the solute concentration in the lumen, which is a constant value. $C_i^{(1)}(-L-L_b, z)$ is the solute concentration at the inter-endothelial cleft entrance $x = -L-L_b$, which can be obtained by jointly solving the governing equations in the BBB.

At the interface of the SGL and the inter-endothelial cleft entrance, the boundary condition described by Eq. B21 can be converted to the following form

$$\frac{D_{i,c}}{D_{i,f}}\frac{\partial C_i^{(1)}}{\partial x} = A = \frac{C_i{}^{(1)}(-L-L_b,z)e^{Z^i\psi_f(-L-L_b)} - C_{iL}}{\int_{-L-L_b-L_f}^{-L-L_b} e^{Z^i\psi_f'(x)}dx} \qquad \text{at } x = -L-L_b \quad \text{(B25)}$$

where $D_{i,c}$ is the effective diffusion coefficient of solute *i* in the inter-endothelial cleft.

Inter-endothelial cleft region

Ion transport. It was assumed that the overall electro-neutrality is satisfied in the inter-endothelial cleft

$$\sum_i Z^i C_i^{(n)} = 0 \qquad i = +, -, TS;\ n = 1,2,3 \quad \text{(B26)}$$

Here, $C_i^{(n)}$is the concentration of positive (i=+) and negative (i=-) monovalent ions and charged test solutes (i=TS) in different regions of the inter-endothelial cleft (n=1,2,3) (see **Fig. 3.2**). As in the SGL, the concentration of test solutes in Eq. B26 can be neglected compared with the concentration of ions, Eq. B26 becomes,

$$C_+^{(n)} = C_-^{(n)} \qquad n=1,2,3 \quad \text{(B27)}$$

At the interface between SGL and inter-endothelial cleft ($x = -L-L_b$), the Donnan equilibrium is satisfied. This gives,

$$\psi^{(1)} - \psi'_f = \ln\left[\frac{C'_{+,f}}{C_+^{(1)}}\right] = \ln\left[\frac{C_-^{(1)}}{C'_{-,f}}\right] \quad \text{at } x = -L - L_b \tag{B28}$$

Combining Eqs. B27 and B28 gives

$$C_+^{(1)} = \sqrt{C'_{+,f} C'_{-,f}} \qquad \text{at } x = -L - L_b \tag{B29}$$

The condition for no electrical current flows across the inter-endothelial cleft is

$$\sum_i Z^i J_i^{(n)} = 0 \qquad i = +, -, TS\,; n = 1,2,3 \tag{B30}$$

Neglecting the current due to the test solutes, Eq. B30 reduces to

$$J_+^{(n)} = J_-^{(n)} \qquad n = 1,2,3 \tag{B31}$$

As in the SGL, the flux of ions and test solutes in the inter-endothelial cleft is expressed as following based on modified Nernst-Plank equation,

$$J_i^{(n)} = -D_i^{(n)}\left(\nabla C_i^{(n)} + Z^i C_i^{(n)} \nabla\psi^{(n)}\right) + K_i^{(n)} J_v C_i^{(n)} \qquad i = +, -, TS; n = 1,2,3 \tag{B32}$$

Where $C_i^{(n)}$, $D_i^{(n)}$, and $K_i^{(n)}$ are concentration, diffusion coefficient and hindrance factor of positive ($i = +$) and negative ions ($i = -$) for different region of inter-endothelial cleft (i=1, 2, 3), respectively. $\psi^{(n)}$ is the dimensionless electrical potential in different regions of the inter-endothelial cleft. Through the same analysis as in the SGL, the Peclet number for the test solutes in the cleft region is in the order of 10^{-3}, and that for the ions, $O(10^{-4})$. The contribution to ion and test solute transport from the filtration can be neglected. In addition, the depth of the cleft L is much bigger than the cleft width 2B, the transport in the cleft can be approximated as 1-D(Li *et al.*, 2010). Therefore, for the ion transport, Eq. B32 can be simplified as

$$J_+^{(n)} = -D_+^{(n)}\left(\frac{dC_+^{(n)}}{dx} + C_+^{(n)}\frac{d\psi^{(n)}}{dx}\right) \tag{B33}$$

$$J_-^{(n)} = -D_-^{(n)}\left(\frac{dC_-^{(n)}}{dx} - C_-^{(n)}\frac{d\psi^{(n)}}{dx}\right) \tag{B34}$$

The conditions of electro-neutrality (Eq. B26) and zero current flow (Eq. B31) can be used to eliminate $C_-^{(n)}$ and $J_-^{(n)}$ from Eqs. B33 and B34, so that

$$\frac{dC_+^{(n)}}{dx} = -\frac{J_+^{(n)}(D_-^{(n)}+D_+^{(n)})}{2D_-^{(n)}D_+^{(n)}} \tag{B35}$$

$$\frac{d\psi^{(n)}}{dx} = \frac{J_+^{(n)}(D_+^{(n)}-D_-^{(n)})}{2D_-^{(n)}D_+^{(n)}C_+^{(n)}} \tag{B36}$$

Integrate Eq. B35 across the inter-endothelial cleft, we can get

$$C_+^{(3)}(x) - C_+^{(1)}(-L-L_b) = -\frac{J_+^{(n)}\left(D_-^{(n)}+D_+^{(n)}\right)}{2D_-^{(n)}D_+^{(n)}}(x+L+L_b) \tag{B37}$$

Test solute transport. Under steady state, when neglecting the convective contribution as analyzed earlier, the conservation of mass relation for the test solutes in the inter-endothelial cleft gives

$$\nabla \cdot \left[J_i^{(n)}\right] = 0 \qquad i = \text{TS; n=1,2,3} \tag{B38}$$

Where $J_i^{(n)} = -D_i^{(n)}\left(\nabla C_i^{(n)} + Z^i C_i^{(n)} \nabla \psi^{(n)}\right)$

Regions n = 1,2,3 are the cleft regions before the tight junction, within the tight junction, and after the tight junction of the inter-endothelial cleft (**Fig. 3.2**). Here $C_i^{(n)}$, $D_i^{(n)}$, $\psi^{(n)}$ are the concentration, effective diffusion coefficient, and dimensionless electric potential of test solutes in each region of the inter-endothelial cleft, respectively.

At the interfaces between different regions of the interendothelial cleft, continuity in concentration and solute flow gives

$$C_i^{(1)} = C_i^{(2)} \qquad D_i^{(1)}\left(\frac{\partial C_i^{(1)}}{\partial x} + Z^i \frac{\partial \psi^{(1)}}{\partial x} C_i^{(1)}\right)B = D_i^{(2)}\left(\frac{\partial C_i^{(2)}}{\partial x} + Z^i \frac{\partial \psi^{(2)}}{\partial x} C_i^{(2)}\right)B_s$$

$$\text{at} \quad x = -L - L_b + L_1 \tag{B39}$$

$$C_i^{(2)} = C_i^{(3)} \qquad D_i^{(2)}\left(\frac{\partial C_i^{(2)}}{\partial x} + Z^i \frac{\partial \psi^{(2)}}{\partial x} C_i^{(2)}\right)B_s = D_i^{(3)}\left(\frac{\partial C_i^{(3)}}{\partial x} + Z^i \frac{\partial \psi^{(3)}}{\partial x} C_i^{(3)}\right)B$$

at $x = -L - L_b + L_1 + L_{jun}$ (B40)

Basement Membrane

Ion Transport. The overall electro-neutrality is satisfied in the BM,

$$\sum_i Z^i C'_{i,b} - C_{mb} = 0 \qquad i = +, -, TS \tag{B41}$$

Here, $C'_{i,b}$ is concentration of positive (i=+) and negative (i=-) monovalent ions and charged test solutes (i= TS) in the BM. Similar to the SGL, the concentration of test solutes in Eq. B41 can be neglected compared with the concentration of ions, Eq. B41 becomes,

$$C'_{+,b} = C'_{-,b} + C_{mb} \tag{B42}$$

At the interface between the BM and the inter-endothelial cleft, the Donnan equilibrium is satisfied,

$$\psi^{(3)} - \psi'_b = \ln\left[\frac{C'_{+,b}}{C_+^{(3)}}\right] = \ln\left[\frac{C_-^{(3)}}{C'_{-,b}}\right] \tag{B43}$$

Combining Eqs. A42 and A43 gives

$$C'_{+,b} = \frac{C_{mb} + \sqrt{C_{mb}^2 + 4C_+^{(3)}C_-^{(3)}}}{2} \quad at \;\; x = -L_b \tag{B44}$$

The condition for no electrical current flows across the BM is

$$\sum_i Z^i J_{i,b} = 0\,, \qquad i = +, -, TS \tag{B45}$$

Neglecting the current due to the test solutes, Eq. B45 reduces to

$$J_{+,b} = J_{-,b} \tag{B46}$$

Similar to the SGL, the contribution to the ion transport from the convection can be neglected. Since the width of the basement membrane $2L_b$ is much smaller than its length $2W_a$, the ion transport in the BM can be approximated as 1-D,

$$J_{+,b} = -D_{+,b}\left(\frac{dC'_{+,b}}{dz} + C'_{+,b}\frac{d\psi'_b}{dz}\right) \tag{B47}$$

$$J_{-,b} = -D_{-,b}\left(\frac{dC'_{-,b}}{dz} - C'_{-,b}\frac{d\psi'_b}{dz}\right) \tag{B48}$$

The conditions of electroneutrality (Eq. B42) and zero current flow (Eq. B46) in the BM can be used to eliminate $C'_{-,b}$ and $J_{-,b}$ from Eqs. A47 and A48, so that

$$\frac{dC'_{+,b}}{dz} = \frac{-J_{+,b}[C'_{+,b}D_{+,b}+(C'_{+,b}-C_{mb})D_{-,b}]+D_{+,b}D_{-,b}C'_{+,b}\frac{dC_{mb}}{dz}}{D_{+,b}D_{-,b}(2C'_{+,b}-C_{mb})} \tag{B49}$$

$$\frac{d\psi'_b}{dz} = \frac{J_{+,b}(D_{+,b}-D_{-,b})-D_{+,b}D_{-,b}\frac{dC_{mb}}{dz}}{D_{+,b}D_{-,b}(2C'_{+,b}-C_{mb})} \tag{B50}$$

In our model, charge density C_{mb} in the BM is considered to be a constant (see Model Description in the main text) so $\frac{dC_{mb}}{dz} = 0$ and the above equation can be simplified as

$$\frac{dC'_{+,b}}{dz} = \frac{-J_{+,b}[C'_{+,b}D_{+,b}+(C'_{+,b}-C_{mb})D_{-,b}]}{D_{+,b}D_{-,b}(2C'_{+,b}-C_{mb})} \tag{B51}$$

$$\frac{d\psi'_b}{dz} = \frac{J_{+,b}(D_{+,b}-D_{-,b})}{D_{+,b}D_{-,b}(2C'_{+,b}-C_{mb})} \tag{B52}$$

Eq. B51 was integrated across the BM to get

$$C_{mb}(D_{-,b}-D_{+,b})\ln\frac{(D_{-,b}+D_{+,b})C'_{+,b}(z)-C_{mb}D_{-,b}}{(D_{-,b}+D_{+,b})C'_{+,b}(0)-C_{mb}D_{-,b}} = -2(D_{-,b}+D_{+,b})\left[C'_{+,b}(z)-C'_{+,b}(0)\right] - \frac{J_{+,b}}{D_{+,b}D_{-,b}}(D_{-,b}+$$

$$D_{+,b}2z \tag{B53}$$

Test solute transport. Under steady state, when neglecting the convective contribution similar to that in the SGL, the conservation of mass relation for the test solutes in the BM(Li *et al.*, 2010) gives

$$\nabla\cdot\left[J_{i,b}\right] = 0 \qquad\qquad i = TS \tag{B54}$$

Where $J_{i,b} = -D_{i,b}\left(\nabla C'_{i,b} + Z^i C'_{i,b}\nabla\psi'_b\right)$

Since the width of the basement membrane $2L_b$ is much smaller than its length $2W_a$, the solute transport in the BM can be approximated as 1-D. Integrating Eq. B54 gives,

$$\frac{dC'_{i,b}}{dz} + Z^i \frac{d\psi'_b}{dz} C'_{i,b} = A_b \qquad i = \text{TS} \tag{B55}$$

Here A_b is a constant. The Donnan equilibrium relationship at the two interfaces of the BM as shown by the following equation

$$C'_{i,b}(z) = C_{i,b}(z) e^{[Z^i(\psi_b(z) - \psi'_b)]} \qquad z = 0 \; and \; z = W_a + B_a \tag{B56}$$

where ψ'_b and ψ_b are the dimensionless electrical potentials inside and outside the BM. At interface of the BM and the inter-endothelial cleft, $\psi_b(0) = \psi^{(3)}(-L_b)$. At interface of the BM and the cleft between astrocyte foot processes, $\psi_b(W_a + B_a) = \psi^{(4)}(L_b)$. Here $\psi^{(4)}(x)$ is the dimensionless electric potential in the cleft between astrocyte foot processes.

The boundary conditions at the two interfaces of the BM are,

$$C_i^{(3)}(-L_b) = C_{i,b}(0),\ \frac{D_{i,c}}{D_{i,b}} \frac{1}{2L_b} \int_0^B \frac{\partial C_i^{(3)}}{\partial x} dz = \frac{C_{i,b}(W_a+B_a) e^{Z^i \psi_b(W_a+B_a)} - C_i^{(3)}(-L_b,0)}{\int_0^{W_a+B_a} e^{Z^i \psi'_b(z)} dz}$$

at z =0, $x = -L_b$ (B57)

$$C_i^{(4)}(L_b) = C_{i,b}(W_a + B_a)\ \frac{D_i^{(4)}}{D_{i,b}} \frac{1}{2L_b} \int_0^{B_a} \frac{\partial C_i^{(4)}}{\partial x} dz = \frac{C_{i,b}(W_a+B_a) e^{Z^i \psi_b(W_a+B_a)} - C_i^{(3)}(-L_b,0)}{\int_0^{W_a+B_a} e^{Z^i \psi'_b(z)} dz}$$

at z = $W_a + B_a, x = L_b$ (B58)

where $D_{i,b}$ and $D_i^{(4)}$ are the effective diffusion coefficients of test solute *i* in the BM and in the cleft between astrocyte foot processes.

Cleft between astrocyte foot processes

Ion transport. The same as in other regions, the overall electro-neutrality is satisfied in the cleft between astrocyte foot processes

$$\sum_i Z^i C_i^{(4)} = 0 \qquad i = +, -, TS \tag{B59}$$

Here, $C_i^{(4)}$ is concentration of positive (i=+) and negative (i=-) monovalent ions and charged test solutes (i = TS) in the cleft between astrocyte foot processes. As in the previous regions, neglecting the concentration of test solutes, Eq. B59 becomes,

$$C_+^{(4)} = C_-^{(4)} \tag{B60}$$

At the interface between the BM and cleft between astrocyte clefts ($x = L_b$), the Donnan equilibrium is also satisfied. This gives

$$\psi^{(4)} - \psi_b' = \ln\left[\frac{C_{+,b}'}{C_+^{(4)}}\right] = \ln\left[\frac{C_-^{(4)}}{C_{-,b}'}\right] \qquad \text{at } x = L_b \tag{B61}$$

Here $\psi^{(4)}$, $C_+^{(4)}$, and $C_-^{(4)}$ are the dimensionless electrical potential, concentration of positive and negative monovalent ions in the cleft between astrocyte clefts respectively. Combining Eqs. B60 and B61 gives,

$$C_+^{(4)} = \sqrt{C_{+,b}' C_{-,b}'} \qquad \text{at } x = L_b \tag{B62}$$

The condition for no electrical current flows across the cleft between astrocyte foot processes is

$$\sum_i Z^i J_i^{(4)} = 0 \qquad i = +, -, TS \tag{B63}$$

Neglecting the current due to the test solutes, Eq. B63 reduces to

$$J_+^{(4)} = J_-^{(4)} \tag{B64}$$

Similar to the previous regions, the contribution from the convection can be

neglected while 1-D approximation is applied to the cleft between astrocyte processes since the cleft depth L_a is much larger than its width $2B_a$, as the ion flux can be expressed as,

$$J_+^{(4)} = -D_+^{(4)}\left(\frac{dC_+^{(4)}}{dx} + C_+^{(4)}\frac{d\psi^{(4)}}{dx}\right) \tag{B65}$$

$$J_-^{(4)} = -D_-^{(4)}\left(\frac{dC_-^{(4)}}{dx} - C_-^{(4)}\frac{d\psi^{(4)}}{dx}\right) \tag{B66}$$

The conditions of electroneutrality (Eq. B60) and zero current flow (Eq. B64) can be used to eliminate $C_-^{(4)}$ and $J_-^{(4)}$ from Eqs. B65 and B66,

$$\frac{dC_+^{(4)}}{dx} = -\frac{J_+^{(4)}(D_-^{(4)}+D_+^{(4)})}{2D_-^{(4)}D_+^{(4)}} \tag{B67}$$

$$\frac{d\psi_+^{(4)}}{dx} = \frac{J_+^{(4)}(D_+^{(4)}-D_-^{(4)})}{2D_-^{(4)}D_+^{(4)}C_+^{(4)}} \tag{B68}$$

Integrate Eq. B67 across the cleft between astrocyte foot processes, we can get

$$C_+^{(4)}(L_a+L_b) - C_+^{(4)}(L_b) = -\frac{J_+^{(4)}\left(D_-^{(4)}+D_+^{(4)}\right)}{2D_-^{(4)}D_+^{(4)}}(x-L_b) \tag{B69}$$

Test solute transport. Under steady state, when neglecting the convective contribution as analyzed in the inter-endothelial cleft, the conservation of mass relation for the test solutes in the cleft between astrocyte foot processes gives

$$\nabla\cdot\left[J_i^{(4)}\right] = 0 \qquad i = \text{TS} \tag{B70}$$

Where $J_i^{(4)} = -D_i^{(4)}\left(\nabla C_i^{(4)} + Z^i C_i^{(4)}\nabla\psi^{(4)}\right)$

Since the width of cleft between astrocyte foot processes $2B_a$ is small compared to its length L_a, the test solute transport in the cleft between astrocyte foot processes can be treated as unidirectional, Eq. B70 is simplified to

$$\frac{d}{dx}\left[-D_i^{(4)}\left(\frac{\partial C_i^{(4)}}{\partial x} + Z^i C_i^{(4)}\frac{\partial\psi^{(4)}}{\partial x}\right)\right] = 0 \qquad i = \text{TS} \tag{B71}$$

$$or \qquad \frac{\partial C_i^{(4)}}{\partial x} + Z^i \frac{\partial \psi^{(4)}}{\partial x} C_i^{(4)} = A_4 \tag{B72}$$

Here A_4 is a constant, $C_i^{(4)}$, $D_i^{(4)}$, $\psi^{(4)}$ are the concentration of test solute, effective diffusion coefficient of test solute, and dimensionless electric potential in the cleft between astrocyte foot processes.

At the interface of this cleft region and the brain tissue space, the boundary condition is,

$$C_i^{(4)} = C_{i,A} \qquad \text{at} \quad x = L_b + L_a \tag{B73}$$

Here $C_{i,A}$ is concentration of test solute i in the tissue space, which is a constant.

B.2 Effective Diffusion Coefficients in Different Regions of the BBB

In the SGL, the effective diffusion coefficient of species i is calculated using the following equations (Ogston *et al.*, 1973; Michel and Curry, 1999; Sugihara-Seki and Fu, 2005)

$$D_{i,f} = D_i^{free}[1 - V_f{}^{0.5}\left(1 + \frac{2r_s}{\pi^{0.5} r_f}\right)]\phi \tag{B74}$$

$$\phi = 1 - V_f\left(1 + \frac{r_s}{r_f}\right)^2 \tag{B75}$$

Here D_i^{free} is the solute diffusion coefficient in a free aqueous solution, r_s is the radius of the solute, r_f is the radius of the fiber and V_f the fiber volume fraction. ϕ is the solute partition coefficient, which describes the steric exclusion of the fiber to the solute. The other term in Eq. B74 describes the diffusion resistance of the fiber to the solute.

In the BM, the effective solute diffusion coefficient includes both the effect from the fiber matrix and the cleft. Compared to the SGL, there is an additional drag on the molecule moving within the cleft relative to movement in free solution, and the steric

exclusion at the cleft entrance ϕ_b (Ogston *et al.*, 1973; Weinbaum *et al.*, 1992; Michel and Curry, 1999; Sugihara-Seki and Fu, 2005).

$$D_{i,b} = D_i^{free}\left[1 - V_f{}^{0.5}\left(1 + \frac{2r_s}{\pi^{0.5} r_f}\right)\right]\phi(1 - 1.004\beta_b + 0.418\beta_b^3 + 0.210\beta_b^4 - 0.169\beta_b^5)\phi_b \quad \text{(B76)}$$

$$\beta_b = \frac{r_s}{L_b}, \quad \phi_b = 1 - \beta_b \quad \text{(B77)}$$

Here L_b is the half width of the BM.

The electrical interaction can be estimated by a Debye length, over which significant charge exclusion or attraction occurs. For our range of charge density in the SGL and in the BM, its Debye length was estimated as ~1 nm(Chen and Fu, 2009). This indicates that the electrical interaction between the charged SGL and BM and the charged solute can be neglected if the distance between them is over 1 nm. Squire et al. (Squire *et al.*, 2001) found that the distance between the matrix fibers in the SGL is ~8 nm. Therefore, the electrical interaction between the charged SGL and BM and our test solutes (~4 nm diameter) and ions (less than 0.5 nm diameter) is negligible.

In the cleft regions 1,2,3,4, the effective diffusion coefficients of species i in region *n* is calculated using the following equation(Ogston *et al.*, 1973; Weinbaum *et al.*, 1992; Michel and Curry, 1999; Sugihara-Seki and Fu, 2005),

$$D_i^{(n)} = D_i^{free}\left(1 - 1.004\beta_n + 0.418\beta_n^3 + 0.210\beta_n^4 - 0.169\beta_n^5\right)\phi_n \qquad n = 1,2,3,4 \quad \text{(B78)}$$

$$\beta_n = \frac{r_s}{W_n}, \quad \phi_n = 1 - \beta_n \quad \text{(B79)}$$

Here W_n is the half width of cleft which equals to B, B_s and B_a for $n = 1,3;2;4$ respectively. ϕ_n is the solute partition coefficient at the cleft entrance, which describes the steric exclusion of the cleft to the solute. The other term in Eq. B78 describes the additional drag on the solute moving within the cleft relative to the movement in a free solution.

Using Eqs. B74-79, we calculated the effective diffusion coefficients of the test solutes (ribonuclease and α-lactalbumin) and the ions (cation Na^+ and anion Cl^-) in different regions of the BBB. Their values are listed in **Table 3.2** and **Table B1**.

Table B1 Transport parameters for ions

Diffusion coefficients	Cation (cm^2/s) (r_s=0.097nm) (Hurlbut, 1998)	Anions (cm^2/s) (r_s=0.18nm) (Hurlbut, 1998)
Free diffusion coefficient in aqueous solution at 37°C(Fu *et al.*, 2003)	1.59×10^{-5}	2.12×10^{-5}
Effective diffusion coefficient in the SGL (Michel and Curry, 1999; Fu *et al.*, 2003; Sugihara-Seki and Fu, 2005)	4.39×10^{-6}	5.67×10^{-6}
Effective diffusion coefficient in the inter-endothelial cleft(Michel and Curry, 1999; Fu *et al.*, 2003; Sugihara-Seki and Fu, 2005)	1.55×10^{-5}	2.04×10^{-5}
Effective diffusion coefficient in the small slit of the junction strand(Michel and Curry, 1999; Fu *et al.*, 2003; Sugihara-Seki and Fu, 2005)	1.44×10^{-5}	1.79×10^{-5}
Effective diffusion coefficient in the basement membrane(Michel and Curry, 1999; Fu *et al.*, 2003; Sugihara-Seki and Fu, 2005)	4.32×10^{-6}	5.50×10^{-6}
Effective diffusion coefficient in the cleft between astrocyte feet(Michel and Curry, 1999; Fu *et al.*, 2003; Sugihara-Seki and Fu, 2005)	1.57×10^{-5}	2.07×10^{-5}

B.3 Solution Procedure

Using similar methods as described in (Deen *et al.*, 1980; Chen and Fu, 2004; Chen and Fu, 2009), the Eqs. B13, B14, B35, B36, B51, B52, B67, B68 were solved simultaneously by numerical integration with initial values of $C'_{+,f}$ and ψ'_f at $x = -L_f - L - L_b$ obtained from Eq. B5 and Eq. B6. An iterative procedure similar to the previous literature (Fu *et al.*, 2003; Chen and Fu, 2004; Chen and Fu, 2009) was used, with values

of electric current adjusted until the following relation was satisfied

$$\left|\frac{J_{+,f}\left(-L_f-L-L_b\right)-J_+^{(4)}}{J_{+,f}\left(-L_f-L-L_b\right)}\right| \leq 10^{-5} \tag{B80}$$

Once dimensionless electrical potential distributions were calculated, they were substituted into the governing equations for test solute transport (Eqs. B20, B38, B55, and B71) and the concentration profiles of test solutes in all regions of the BBB can be found with coupled boundary conditions. The permeability of test solutes can then be calculated using Eq. B1 in main text.

Due to the unique geometry of the BBB, in the inter-endothelial cleft, L >> 2B, in the cleft between astrocyte foot processes, L_a >> $2B_a$, and in the BM, $2W_a$ >> $2L_b$ (see **Fig. 3.2**), the above governing equations can be simplified as 1-D. In addition, the contribution to the charged solute transport from the electrical potential (including diffusion potential) and electro-osmosis is much smaller than the diffusion (see **Table B2**) and the electrical partition at interfaces. An analytical solution for each region can be obtained for the concentration distribution of the charged test solute. The solute permeability is thus calculated by Eq. 3.2 in the main text. However, the 2-D effect at the entrance/exit of the inter-endothelial cleft and at that of the BM might contribute to the permeability. In our recent publication(Li *et al.*, 2010), we calculated this 2-D effect on the concentration distribution of a neutral solute with the same size of ribonuclease and α-lactalbumin. The concentration distributions at these entrance/exit regions are shown in **Figs. B1(a,b,c)**. We can see that the 2-D effect is only restricted to less than 1% of the BBB region. If we use 1-D approximation, the underestimation for P is less than 2% (Li *et al.*, 2010).

(a)

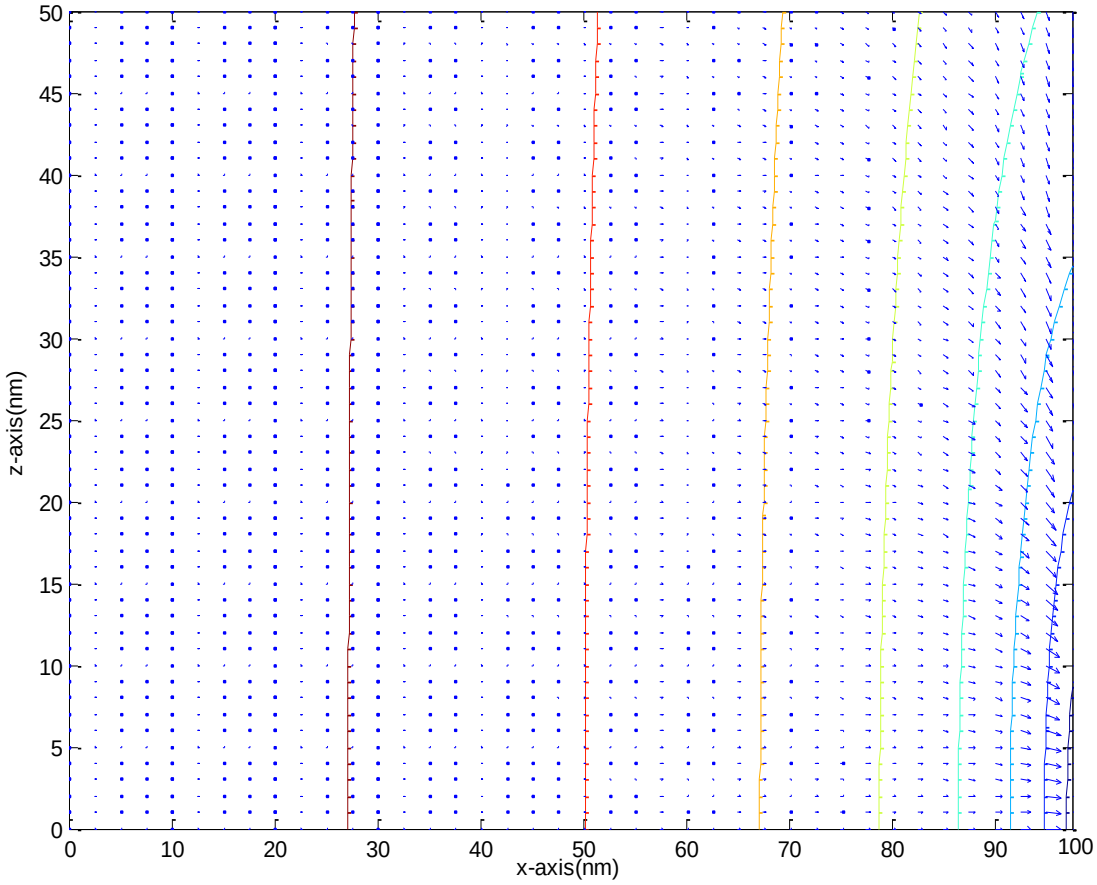
z-axis(nm)
x-axis(nm)
0
5
10
15
20
25
30
35
40
45
50
0
10
20
30
40
50
60
70
80
90
100

(b)

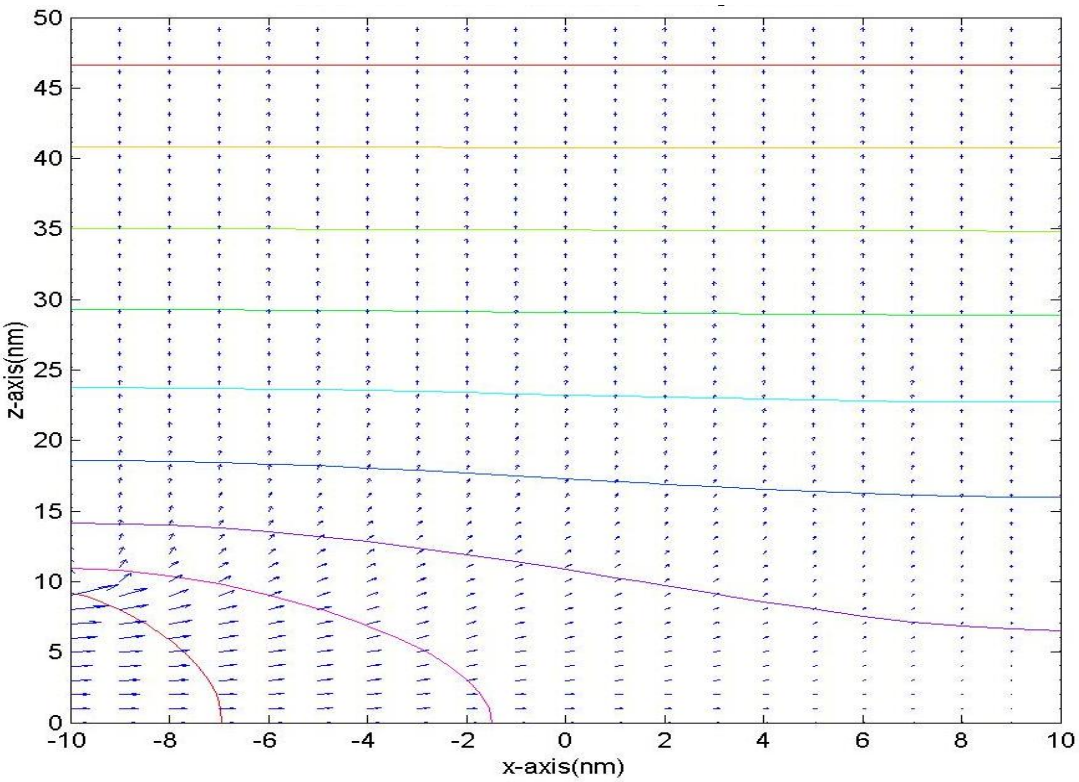
z-axis(nm)
x-axis(nm)
0
5
10
15
20
25
30
35
40
45
50
-10
-8
-6
-4
-2
0
2
4
6
8
10

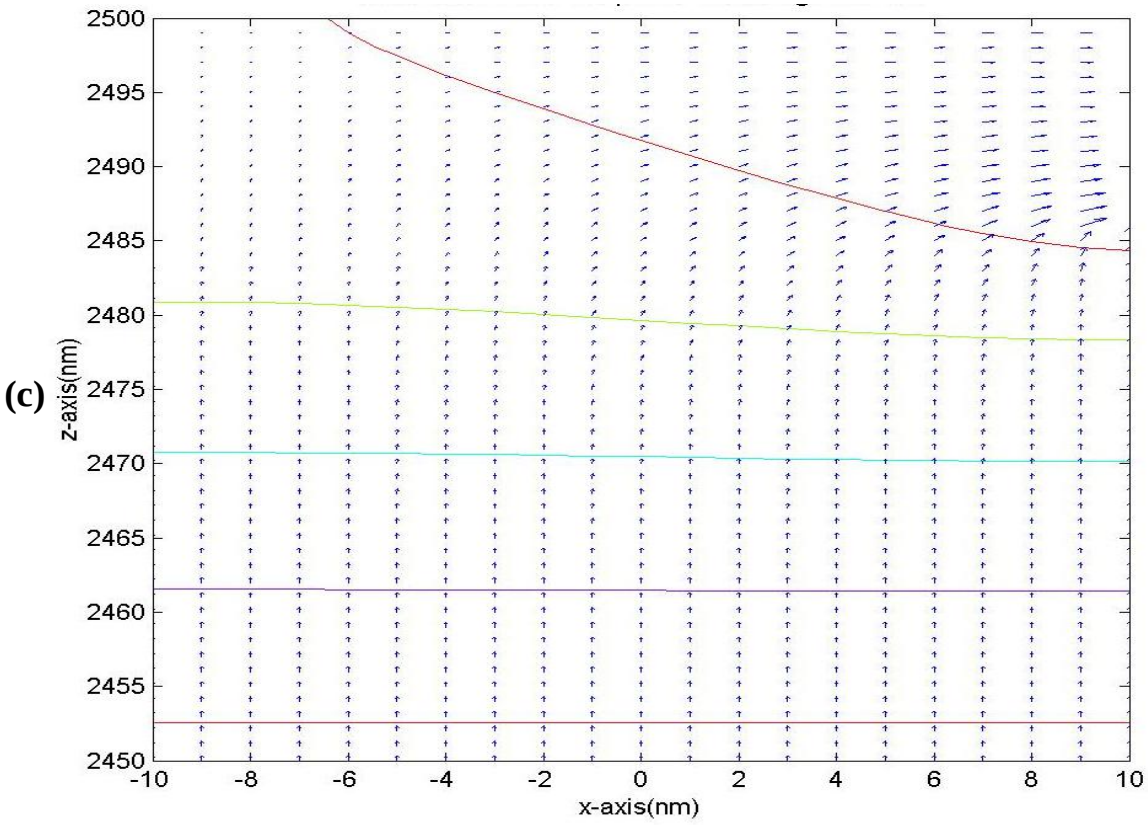

Figure B1. The solute flux (arrows) and concentration (contour lines) profiles **(a)** near the entrance region to the interendothelial cleft from the SGL, **(b)** the entrance region to the BM from the interendothelial cleft, and **(c)** the exit region of the BM to the cleft between astrocyte processes.

Table B2 Comparison of the contribution to charged solute transport from the electrical potential and electro-osmosis and that from diffusion in different regions of the BBB

BBB regions	$C_{mf}=C_{mb}=100$mEq/L				
	ΔC_+ (mM)	$\Delta\psi$	Pe_{charge}		Pe_{em}
			ribonuclease	α-lactalbumin	
The SGL	-5.73×10^{-6}	-4.98×10^{-9}	1.99×10^{-8}	4.98×10^{-8}	1.32×10^{-5}
Inter-endothelial cleft (region 1)	-5.89×10^{-6}	-5.58×10^{-9}	2.23×10^{-8}	5.58×10^{-8}	1.71×10^{-5}
Tight Junction (region 2)	-2.04×10^{-7}	-1.52×10^{-10}	6.08×10^{-10}	1.52×10^{-9}	7.67×10^{-6}
Inter-endothelial cleft (region 3)	-5.70×10^{-6}	-5.40×10^{-9}	2.16×10^{-8}	5.40×10^{-8}	1.65×10^{-5}
The BM	-1.47×10^{-4}	-1.21×10^{-7}	4.84×10^{-7}	1.21×10^{-6}	4.10×10^{-5}
Cleft between astrocyte foot processes (region 4)	-1.66×10^{-5}	-1.58×10^{-8}	6.32×10^{-8}	1.58×10^{-7}	1.08×10^{-4}

Here $Pe_{charge} = Z^i\Delta\psi$ is the ratio of the contribution from electrical potential to that from diffusion. Z^i is the charge number of the test solute, and $\Delta\psi$ is the dimensionless electrical potential difference across each region specified in the first column. Pe_{em} is defined as the ratio of the contribution from electro-osmosis to that from diffusion. For the SGL, $Pe_{em} = 2RT\Delta C_{+,f}K_p/(\mu D_{i,f})$. For the BM, $Pe_{em} = 2RT\Delta C_{+,b}K_b(1-\sqrt{K_b}/L_b\tanh(L_b/\sqrt{K_b}))/(\mu D_{i,b})$. In the cleft regions, $Pe_{em} = 2RT\Delta C_+^{(n)}B_n^2/(3\mu D_i^{(n)})$, n=1, 2, 3, 4. B_n=B when n=1,3; $B_n=B_s$ when n=2; ; $B_n=B_a$ when n=4. Here $2RT\Delta C_+$ is the osmotic pressure difference across each region due to concentration difference of both cations and anions. K_p, K_b are the Darcy permeability in the fiber matrix of the SGL and the BM, respectively. The fluid flows are approximated as the Darcy flow in the SGL, the Brinkman flow in the BM and the Poiseuille flow in the clefts, respectively(Li *et al.*, 2010).

Bibliography

Abbott, N. J., 2002. Astrocyte-endothelial interactions and blood-brain barrier permeability. *Journal of Anatomy* **200**(6): 629-638.

Adamson, R. H., Clough, G., 1992. Plasma-Proteins Modify the Endothelial-Cell Glycocalyx of Frog Mesenteric Microvessels. *Journal of Physiology-London* **445**: 473-486.

Adamson, R. H., *et al.*, 1988. Single capillary permeability to proteins having similar size but different charge. *Am J Physiol* **254**(2 Pt 2): H304-312.

Adamson, R. H., *et al.*, 2004. Oncotic pressures opposing filtration across non-fenestrated rat microvessels. *Journal of Physiology-London* **557**(3): 889-907.

Adamson, R. H., *et al.*, 1993. Pathways through the Intercellular Clefts of Frog Mesenteric Capillaries. *Journal of Physiology-London* **466**: 303-327.

Allt, G., Lawrenson, J. G., 1997. Is the pial microvessel a good model for blood-brain barrier studies? *Brain Research Reviews* **24**(1): 67-76.

Baldwin, S. A., *et al.*, 1996. Blood-brain barrier breach following cortical contusion in the rat. *J Neurosurg* **85**(3): 476-481.

Barzo, P., *et al.*, 1996. Magnetic resonance imaging-monitored acute blood-brain barrier changes in experimental traumatic brain injury. *J Neurosurg* **85**(6): 1113-1121.

Baskaya, M. K., *et al.*, 1997. The biphasic opening of the blood-brain barrier in the cortex and hippocampus after traumatic brain injury in rats. *Neurosci Lett* **226**(1): 33-36.

Beaumont, A., *et al.*, 2000. The permissive nature of blood brain barrier (BBB) opening in edema formation following traumatic brain injury. *Acta Neurochir Suppl* **76**: 125-129.

Boveri, M., *et al.*, 2005. Induction of blood-brain barrier properties in cultured brain capillary endothelial cells: Comparison between primary glial cells and C6 cell line. *Glia* **51**(3): 187-198.

Bowman, P. D., *et al.*, 1983. Brain microvessel endothelial cells in tissue culture: a model for study of blood-brain barrier permeability. *Ann Neurol* **14**(4): 396-402.

Braeckmans, K., *et al.*, 2003. Three-dimensional fluorescence recovery after photobleaching with the confocal scanning laser microscope. *Biophys J* **85**(4): 2240-2252.

Braga, J., *et al.*, 2004. Intracellular macromolecular mobility measured by fluorescence recovery after photobleaching with confocal laser scanning microscopes. *Mol Biol Cell* **15**(10): 4749-4760.

Brown, R. C., *et al.*, 2007. Tight junction protein expression and barrier properties of immortalized mouse brain microvessel endothelial cells. *Brain Res* **1130**(1): 17-30.

Calabria, A. R., Shusta, E. V., 2006. Blood-brain barrier genomics and proteomics: elucidating phenotype, identifying disease targets and enabling brain drug delivery. *Drug Discov Today* **11**(17-18): 792-799.

Cancel, L. M., *et al.*, 2007. In vitro study of LDL transport under pressurized (convective) conditions. *Am J Physiol Heart Circ Physiol* **293**(1): H126-132.

Cancel, L. M., Tarbell, J. M., 2010. The role of apoptosis in LDL transport through cultured endothelial cell monolayers. *Atherosclerosis* **208**(2): 335-341.

Cassella , J. P., Lawrenson ,J. G. , Firth,J. A., 1997. Development of endothelial paracellular clefts and their tight junctions in the pial microvessels of the rat. *Journal of Neurocytology 2* **26**: 547-575.

Cernak, I., *et al.*, 2004. The pathobiology of moderate diffuse traumatic brain injury as identified using a new experimental model of injury in rats. *Neurobiol Dis* **17**(1): 29-43.

Cohen, Z., *et al.*, 1995. Ultrastructural Analysis of Tryptophan-Hydroxylase Immunoreactive Nerve-Terminals in the Rat Cerebral-Cortex and Hippocampus - Their Associations with Local Blood-Vessels. *Neuroscience* **66**(3): 555-569.

Crone, C., Olesen, S. P., 1982. Electrical resistance of brain microvascular endothelium. *Brain Res* **241**(1): 49-55.

Cucullo, L., *et al.*, 2002. A new dynamic in vitro model for the multidimensional study of astrocyte-endothelial cell interactions at the blood-brain barrier. *Brain Research* **951**(2): 243-254.

Curry, F. E.,1983. Mechanics and thermodynamics of transcapillary exchange. In handbook of Physiology. The cardiovascular system. Bethesda, American Physiology Society.

Curry, F. E., *et al.*, 1989. Modulation of Microvessel Wall Charge by Plasma Glycoprotein Orosomucoid. *American Journal of Physiology* **257**(5): H1354-H1359.

Dagan, Z., *et al.*, 1982. An infinite-series solution for the creeping motion through an orifice of finite length. *J. Fluid Mech.* **115**: 505-523.

Damiano, E. R., Stace, T. M., 2002. A mechano-electrochemical model of radial deformation of the capillary glycocalyx. *Biophysical Journal* **82**(3): 1153-1175.

Decuzzi, P., Ferrari, M., 2007. The role of specific and non-specific interactions in receptor-mediated endocytosis of nanoparticles. *Biomaterials* **28**(18): 2915-2922.

Deen, W. M., *et al.*, 1980. Theoretical-Model for Glomerular-Filtration of Charged Solutes. *American Journal of Physiology* **238**(2): F126-F139.

del Zoppo, G. J., Hallenbeck, J. M., 2000. Advances in the vascular pathophysiology of ischemic stroke. *Thrombosis Research* **98**(3): V73-V81.

Deli, M. A., *et al.*, 2005. Permeability studies on in vitro blood-brain barrier models: Physiology, pathology, and pharmacology. *Cellular and Molecular Neurobiology* **25**(1): 59-127.

Demeuse, P., *et al.*, 2002. Compartmentalized coculture of rat brain endothelial cells and astrocytes: a syngenic model to study the blood-brain barrier. *Journal of Neuroscience Methods* **121**(1): 21-31.

deVries, H. E., *et al.*, 1996. The influence of cytokines on the integrity of the blood-brain barrier in vitro. *Journal of Neuroimmunology* **64**(1): 37-43.

Dietrich, W. D., *et al.*, 1994. Early microvascular and neuronal consequences of traumatic brain injury: a light and electron microscopic study in rats. *J Neurotrauma* **11**(3): 289-301.

Ehrlich, P.,1885. Das sauerstufbudurfnis des organismus. Hirschwald, Berlin.

Engvall, E., 1995. Structure and function of basement membranes. *Int J Dev Biol* **39**(5): 781-787.

Farkas, E., Luiten, P. G. M., 2001. Cerebral microvascular pathology in aging and Alzheimer's disease. *Progress in Neurobiology* **64**(6): 575-611.

Fletcher, N. F., *et al.*, 2006. Growth and characterisation of a cell culture model of the feline blood-brain barrier. *Vet Immunol Immunopathol* **109**(3-4): 233-244.

Floris, S., *et al.*, 2004. Blood-brain barrier permeability and monocyte infiltration in experimental allergic encephalomyelitis: a quantitative MRI study. *Brain* **127**(Pt 3): 616-627.

Franke, H., *et al.*, 1999. An improved low-permeability in vitro-model of the blood-brain barrier: transport studies on retinoids, sucrose, haloperidol, caffeine and mannitol. *Brain Research* **818**(1): 65-71.

Fraser, P. A., *et al.*, 1990. Measurement of Filtration Coefficient in Single Cerebral Microvessels of the Frog. *Journal of Physiology-London* **423**: 343-361.

Fu, B., Chen, B., 2003. A model for the modulation of microvessel permeability by junction strands. *Journal of Biomechanical Engineering-Transactions of the Asme* **125**(5): 620-627.

Fu, B. M., *et al.*, 1995. A diffusion wake model for tracer ultrastructure-permeability studies in microvessels. *American Journal of Physiology-Heart and Circulatory Physiology* **38**(6): H2124-H2140.

Fu, B. M., *et al.*, 1994. A Junction-Orifice-Fiber Entrance Layer Model for Capillary-Permeability - Application to Frog Mesenteric Capillaries. *Journal of Biomechanical Engineering-Transactions of the Asme* **116**(4): 502-513.

Fu, B. M. M., *et al.*, 2003. An electrodiffusion model for effects of surface glycocalyx layer on microvessel permeability. *American Journal of Physiology-Heart and Circulatory Physiology* **284**(4): H1240-H1250.

Fukuda, K., *et al.*, 1995. The blood-brain barrier disruption to circulating proteins in the early period after fluid percussion brain injury in rats. *J Neurotrauma* **12**(3): 315-324.

Gaillard, P. J., de Boer, A. G., 2000. Relationship between permeability status of the blood-brain barrier and in vitro permeability coefficient of a drug. *European Journal of Pharmaceutical Sciences* **12**(2): 95-102.

Gao, H., *et al.*, 2005. Mechanics of receptor-mediated endocytosis. *Proc Natl Acad Sci U S A* **102**(27): 9469-9474.

Goldmann, E., 1913. Vitalfarbung am zentralnervensystem. Abhandl Konigl preuss. *Akad Wiss*(1): 1-60.

Gumbleton, M., Audus, K. L., 2001. Progress and limitations in the use of in vitro cell cultures to serve as a permeability screen for the blood-brain barrier. *J Pharm Sci* **90**(11): 1681-1698.

Guo, P., *et al.*, 2000. A hydrodynamic mechanosensory hypothesis for brush border microvilli. *American Journal of Physiology-Renal Physiology* **279**(4): F698-F712.

Hamann, G. F., *et al.*, 1995. Microvascular Basal Lamina Antigens Disappear during Cerebral-Ischemia and Reperfusion. *Stroke* **26**(11): 2120-2126.

Hamm, S., *et al.*, 2004. Astrocyte mediated modulation of blood-brain barrier permeability does not correlate with a loss of tight junction proteins from the cellular contacts. *Cell and Tissue Research* **315**(2): 157-166.

Haraldsson, B., Rippe, B., 1987. Orosomucoid as One of the Serum Components Contributing to Normal Capillary Permselectivity in Rat Skeletal-Muscle. *Acta Physiologica Scandinavica* **129**(1): 127-135.

Haraldsson, B. S., *et al.*, 1992. Glomerular Permselectivity Is Dependent on Adequate Serum Concentrations of Orosomucoid. *Kidney International* **41**(2): 310-316.

Haseloff, R. F., *et al.*, 2005. In search of the astrocytic factor(s) modulating blood-brain barrier functions in brain capillary endothelial cells in vitro. *Cellular and Molecular Neurobiology* **25**(1): 25-39.

Hawkins, B. T., Davis, T. P., 2005. The blood-brain barrier/neurovascular unit in health and disease. *Pharmacological Reviews* **57**(2): 173-185.

Hemmila, J. M., Drewes, L. R., 1993. Glucose transporter (GLUT1) expression by canine brain microvessel endothelial cells in culture: an immunocytochemical study. *Adv Exp Med Biol* **331**: 13-18.

Henry, C. B. S., Duling, B. R., 1999. Permeation of the luminal capillary glycocalyx is determined by hyaluronan. *American Journal of Physiology-Heart and Circulatory Physiology* **277**(2): H508-H514.

Hu, X., Weinbaum, S., 1999. A new view of Starling's hypothesis at the microstructural level. *Microvasc Res* **58**(3): 281-304.

Hurwitz, A. A., *et al.*, 1993. Human fetal astrocytes induce the expression of blood-brain barrier specific proteins by autologous endothelial cells. *Brain Res* **625**(2): 238-243.

Johnston, H., *et al.*, 2004. Regulation of Sertoli cell number and activity by follicle-stimulating hormone and androgen during postnatal development in the mouse. *Endocrinology* **145**(1): 318-329.

Karyekar, C. S., *et al.*, 2003. Zonula occludens toxin increases the permeability of molecular weight markers and chemotherapeutic agents across the bovine brain microvessel endothelial cells. *Journal of Pharmaceutical Sciences* **92**(2): 414-423.

Kemper, E. M., *et al.*, 2004. Modulation of the blood-brain barrier in oncology: therapeutic opportunities for the treatment of brain tumours? *Cancer Treatment Reviews* **30**(5): 415-423.

Kim, J. H., *et al.*, 2006. Blood-neural barrier: Intercellular communication at glio-vascular interface. *Journal of Biochemistry and Molecular Biology* **39**(4): 339-345.

Kleinman, H. K., Martin, G. R., 2005. Matrigel: basement membrane matrix with

biological activity. *Semin Cancer Biol* **15**(5): 378-386.

Koto, T., *et al.*, 2007. Hypoxia disrupts the barrier function of neural blood vessels through changes in the expression of claudin-5 in endothelial cells. *American Journal of Pathology* **170**(4): 1389-1397.

Kraus, J., *et al.*, 2008. Interferon-beta stabilizes barrier characteristics of the blood-brain barrier in four different species in vitro. *Multiple Sclerosis* **14**(6): 843-852.

Lawrence, J. R., *et al.*, 1994. Determination of Diffusion Coefficients in Biofilms by Confocal Laser Microscopy. *Appl Environ Microbiol* **60**(4): 1166-1173.

Lawrenson, J. G., Reid, A.R. , Allt , G., 1997. Molecular characteristics of pial microvessels of the rat optic nerve: Can pial microvessels be used as a model for the blood-brain barrier? *Cell and Tissue Research* **288**: 259-265.

LeBleu, V. S., *et al.*, 2007. Structure and function of basement membranes. *Exp Biol Med (Maywood)* **232**(9): 1121-1129.

Leblond, C. P., Inoue, S., 1989. Structure, composition, and assembly of basement membrane. *Am J Anat* **185**(4): 367-390.

Lewandowsky, M., 1900. Zur lehre von der cerebrospinalflussigkeit. *Z Klin Med* **40**: 480-494.

Mak, M., *et al.*, 1995. Distribution of drugs following controlled delivery to the brain interstitium. *J Neurooncol* **26**(2): 91-102.

Malina, K. C., *et al.*, 2009. Closing the gap between the in-vivo and in-vitro blood-brain barrier tightness. *Brain Res* **1284**: 12-21.

Meyer, J., *et al.*, 1990. Blood-brain barrier characteristic enzymatic properties in cultured brain capillary endothelial cells. *Brain Res* **514**(2): 305-309.

Michel, C. C., Curry, F. E., 1999. Microvascular permeability. *Physiological Reviews* **79**(3): 703-761.

Miosge, N., 2001. The ultrastructural composition of basement membranes in vivo. *Histol Histopathol* **16**(4): 1239-1248.

Moody, D. M., 2006. The blood-brain barrier and blood-cerebral spinal fluid barrier. *Semin Cardiothorac Vasc Anesth* **10**(2): 128-131.

Neuwelt, E. A., 2004a. Mechanisms of disease: The blood-brain barrier. *Neurosurgery* **54**(1): 131-140.

Neuwelt, E. A., 2004b. Mechanisms of disease: the blood-brain barrier. *Neurosurgery* **54**(1): 131-140; discussion 141-132.

Nicolazzo, J. A., *et al.*, 2006a. Methods to assess drug permeability across the blood-brain barrier. *Journal of Pharmacy and Pharmacology* **58**(3): 281-293.

Nicolazzo, J. A., *et al.*, 2006b. Methods to assess drug permeability across the blood-brain barrier. *J Pharm Pharmacol* **58**(3): 281-293.

Ogston, A. G., *et al.*, 1973. Transport of Compact Particles through Solutions of Chain-Polymers. *Proceedings of the Royal Society of London Series a-Mathematical Physical and Engineering Sciences* **333**(1594): 297-316.

Omidi, Y., *et al.*, 2003. Evaluation of the immortalised mouse brain capillary endothelial cell line, b.End3, as an in vitro blood-brain barrier model for drug uptake and transport studies. *Brain Res* **990**(1-2): 95-112.

Pardridge, W. M., 1999. Blood-brain barrier biology and methodology. *Journal of Neurovirology* **5**(6): 556-569.

Pardridge, W. M., 2005. Molecular biology of the blood-brain barrier. *Molecular Biotechnology* **30**(1): 57-69.

Pardridge, W. M., 2006. Molecular Trojan horses for blood-brain barrier drug delivery. *Current Opinion in Pharmacology* **6**(5): 494-500.

Paulson, O. B., Newman, E. A., 1987. Does the Release of Potassium from Astrocyte Endfeet Regulate Cerebral Blood-Flow. *Science* **237**(4817): 896-898.

Petty, M. A., Lo, E. H., 2002. Junctional complexes of the blood-brain barrier: permeability changes in neuroinflammation. *Prog Neurobiol* **68**(5): 311-323.

Poller, B., *et al.*, 2008. The human brain endothelial cell line hCMEC/D3 as a human blood-brain barrier model for drug transport studies. *Journal of Neurochemistry* **107**(5): 1358-1368.

Rascher, G., *et al.*, 2002. Extracellular matrix and the blood-brain barrier in glioblastoma multiforme: spatial segregation of tenascin and agrin. *Acta Neuropathol* **104**(1): 85-91.

Rolfe, D. F. S., Brown, G. C., 1997. Cellular energy utilization and molecular origin of standard metabolic rate in mammals. *Physiological Reviews* **77**(3): 731-758.

Romero, I. A., *et al.*, 2003. Changes in cytoskeletal and tight junctional proteins correlate with decreased permeability induced by dexamethasone in cultured rat brain endothelial cells. *Neuroscience Letters* **344**(2): 112-116.

Rosenberg, G. A., 1999. Ischemic brain edema. *Prog Cardiovasc Dis* **42**(3): 209-216.

Rosenberg, G. A., *et al.*, 1993. Bacterial collagenase disrupts extracellular matrix and opens blood-brain barrier in rat. *Neurosci Lett* **160**(1): 117-119.

Sahagun, G., *et al.*, 1990. Permeability of neutral vs. anionic dextrans in cultured brain microvascular endothelium. *Am J Physiol* **259**(1 Pt 2): H162-166.

Salvetti, F., *et al.*, 2002. Insulin permeability across an in vitro dynamic model of endothelium. *Pharmaceutical Research* **19**(4): 445-450.

Santaguida, S., *et al.*, 2006. Side by side comparison between dynamic versus static models of blood-brain barrier in vitro: A permeability study. *Brain Research* **1109**: 1-13.

Schulze, C., Firth, J. A., 1992. Interendothelial Junctions during Blood-Brain-Barrier Development in the Rat - Morphological-Changes at the Level of Individual Tight Junctional Contacts. *Developmental Brain Research* **69**(1): 85-95.

Shi, Z. D., *et al.*, Interstitial flow induces MMP-1 expression and vascular SMC migration in collagen I gels via an ERK1/2-dependent and c-Jun-mediated mechanism. *Am J Physiol Heart Circ Physiol* **298**(1): H127-135.

Simard, M., *et al.*, 2003. Signaling at the gliovascular interface. *Journal of Neuroscience* **23**(27): 9254-9262.

Soga, N., *et al.*, 2001. Rac regulates vascular endothelial growth factor stimulated motility. *Cell Commun Adhes* **8**(1): 1-13.

Squire, J. M., *et al.*, 2001. Quasi-periodic substructure in the microvessel endothelial glycocalyx: A possible explanation for molecular filtering? *Journal of Structural Biology* **136**(3): 239-255.

Stace, T. M., Damiano, E. R., 2001. An electrochemical model of the transport of charged molecules through the capillary glycocalyx. *Biophysical Journal* **80**(4): 1670-1690.

Sugaya, R., *et al.*, 2006. Thermal diffusion of dextran in aqueous solutions in the absence and the presence of urea. *Biomacromolecules* **7**(2): 435-440.

Sugihara-Seki, M., Fu, B. M. M., 2005. Blood flow and permeability in microvessels. *Fluid Dynamics Research* **37**(1-2): 82-132.

Tarbell, J. M., Pahakis, M. Y., 2006. Mechanotransduction and the glycocalyx. *Journal of Internal Medicine* **259**(4): 339-350.

Thompson, S. E., *et al.*, 1994. Leucine-Enkephalin Effects on Paracellular and Transcellular Permeation Pathways across Brain Microvessel Endothelial-Cell Monolayers. *Journal of Cardiovascular Pharmacology* **24**(5): 818-825.

Tyagi, N., *et al.*, 2009. H2S protects against methionine-induced oxidative stress in brain endothelial cells. *Antioxid Redox Signal* **11**(1): 25-33.

Ueno, M., *et al.*, 2004. Blood-brain barrier disruption in the hypothalamus of young adult spontaneously hypertensive rats. *Histochem Cell Biol* **122**(2): 131-137.

Vink, H., Duling, B. R., 1996. Identification of distinct luminal domains for macromolecules, erythrocytes, and leukocytes within mammalian capillaries. *Circulation Research* **79**(3): 581-589.

Wang, H., *et al.*, 2006a. Shear stress induces endothelial transdifferentiation from mouse smooth muscle cells. *Biochemical and Biophysical Research Communications* **346**(3): 860-865.

Wang, R. S., *et al.*, 2006b. Androgen receptor in sertoli cell is essential for germ cell nursery and junctional complex formation in mouse testes. *Endocrinology* **147**(12): 5624-5633.

Weinbaum, S., *et al.*, 1992. A three-dimensional junction-pore-matrix model for capillary permeability. *Microvasc Res* **44**(1): 85-111.

Weinbaum, S., *et al.*, 2003. Mechanotransduction and flow across the endothelial glycocalyx. *Proc Natl Acad Sci U S A* **100**(13): 7988-7995.

Yamamoto, K., *et al.*, 2005. Fluid shear stress induces differentiation of Flk-1-positive embryonic stem cells into vascular endothelial cells in vitro. *Am J Physiol Heart Circ Physiol* **288**(4): H1915-1924.

Yoder, E. J., 2002. Modifications in astrocyte morphology and calcium signaling induced by a brain capillary endothelial cell line. *Glia* **38**(2): 137-145.

Yuan, W., *et al.*, 2009a. Modulation of the blood-brain barrier permeability by plasma glycoprotein orosomucoid. *Submited to Microvascular Research*

Yuan, W., *et al.*, 2010a. Effect of Surface Charge of Immortalized Mouse Cerebral Endothelial Cell Monolayer on Transport of Charged Solutes. *Ann Biomed Eng* **Jan 20. Epub ahead of print.PMID: 20087768.**

Yuan, W., *et al.*, 2010b. Modulation of the blood-brain barrier permeability by plasma glycoprotein orosomucoid. *Microvascular Research* **80**(1): 148-157.

Yuan, W., *et al.*, 2009b. Non-invasive measurement of solute permeability in cerebral

microvessels of the rat. *Microvascular Research* **77**(2): 166-173.

Zhang, X. B., *et al.*, 2006a. A 1-D model to explore the effects of tissue loading and tissue concentration gradients in the revised Starling principle. *American Journal of Physiology-Heart and Circulatory Physiology* **291**(6): H2950-H2964.

Zhang, Y., *et al.*, 2006b. Porcine brain microvessel endothelial cells as an in vitro model to predict in vivo blood-brain barrier permeability. *Drug Metabolism and Disposition* **34**(11): 1935-1943.